



IROCKS: SPATIALLY RESOLVED KINEMATICS OF $z \sim 1$ STAR-FORMING GALAXIES

ETSUKO MIEDA^{1,2}, SHELLEY A. WRIGHT^{3,4}, JAMES E. LARKIN⁵, LEE ARMUS⁶, STÉPHANIE JUNEAU⁷, SAMIR SALIM⁸, AND
NORMAN MURRAY⁹

¹Dunlap Institute for Astronomy & Astrophysics, University of Toronto, 50 St. George street, Toronto, ON M5S 3H4, Canada; mieda@dunlap.utoronto.ca

²Department of Astronomy & Astrophysics, University of Toronto, 50 St. George street, Toronto, ON M5S 3H4, Canada

³Department of Physics, University of California, San Diego, 9500 Gilman Drive, La Jolla, CA 92093, USA

⁴Center for Astrophysics and Space Sciences, University of California, San Diego, 9500 Gilman Drive, La Jolla, CA 92093, USA

⁵Department of Physics and Astronomy, University of California, Los Angeles, CA 90095, USA

⁶Spitzer Science Center, California Institute of Technology, 1200 E. California Blvd., Pasadena, CA 91125, USA

⁷CEA-Saclay, DSM/IRFU/SAP, F-91191 Gif-sur-Yvette, France

⁸Department of Astronomy, Indiana University, Bloomington, IN 47404, USA

⁹Canadian Institute for Theoretical Astrophysics, University of Toronto, 60 St. George Street, Toronto, ON M5S 3H8, Canada

Received 2016 March 19; revised 2016 August 2; accepted 2016 August 18; published 2016 October 27

ABSTRACT

We present results from the Intermediate Redshift OSIRIS Chemo-Kinematic Survey (IROCKS) for sixteen $z \sim 1$ and one $z \sim 1.4$ star-forming galaxies. All galaxies were observed with OSIRIS with the laser guide star adaptive optics system at Keck Observatory. We use rest-frame nebular $H\alpha$ emission lines to trace morphologies and kinematics of ionized gas in star-forming galaxies on sub-kiloparsec physical scales. We observe elevated velocity dispersions ($\sigma \gtrsim 50 \text{ km s}^{-1}$) seen in $z > 1.5$ galaxies persist at $z \sim 1$ in the integrated galaxies. Using an inclined disk model and the ratio of v/σ , we find that 1/3 of the $z \sim 1$ sample are disk candidates while the other 2/3 of the sample are dominated by merger-like and irregular sources. We find that including extra attenuation toward H II regions derived from stellar population synthesis modeling brings star formation rates (SFRs) using $H\alpha$ and stellar population fit into a better agreement. We explore the properties of the compact $H\alpha$ sub-component, or “clump,” at $z \sim 1$ and find that they follow a similar size–luminosity relation as local H II regions but are scaled-up by an order of magnitude with higher luminosities and sizes. Comparing the $z \sim 1$ clumps to other high-redshift clump studies, we determine that the clump SFR surface density evolves as a function of redshift. This suggests clump formation is directly related to the gas fraction in these systems and may support disk fragmentation as their formation mechanism since gas fraction scales with redshift.

Key words: galaxies: evolution – galaxies: high-redshift – galaxies: kinematics and dynamics – infrared: galaxies

1. INTRODUCTION

Star formation plays a crucial, but poorly understood, role in regulating the growth and formation of distant galaxies over a wide range of mass scales (e.g., Governato et al. 2007; Hopkins et al. 2012; Agertz et al. 2013; Wurster & Thacker 2013; Muratov et al. 2015). Characterizing star formation at high redshift is challenging since both high signal-to-noise ratio (S/N) and high angular resolution observations are required to resolve the kinematics, chemical abundances, and outflow and/or shocks in individual star-forming regions. The latest observations of distant galaxies ($z \gtrsim 1$) have shown high-velocity dispersions in their star-forming regions, suggesting that there are strong energetics and large turbulences present, which may be driven by radiation pressure (e.g., Murray et al. 2010), cold flow (e.g., Genel et al. 2010), and/or supernovae (e.g., Joung & Mac Low 2006). While we are rapidly compiling values for the global parameters (e.g., luminosity, color, star formation rate (SFR), gas/dust content, and stellar mass) of high-redshift galaxies, there is still a gap in our knowledge of processes that regulate galaxy growth and evolution even at modest redshifts of $z \sim 1$ to 2.

Ground-breaking observations with integral field spectrographs (IFSs) coupled to adaptive optics (AO) (e.g., OSIRIS at Keck and SINFONI at the VLT) have probed the dynamical processes of individual high-redshift ($z > 1.5$) star-forming galaxies on kiloparsec scales (see the review by Glazebrook 2013). IFS data of high-redshift systems provide valuable insight into the assembly and star formation properties of early

systems. IFS studies at $z \sim 2$ have shown mounting evidence that a large fraction (between 1/3 and 1/2) of high- z star-forming galaxies ($>10 M_{\odot} \text{ yr}^{-1}$) are in rotating disk systems (Förster Schreiber et al. 2011a, 2011b), while the rest are irregular or interacting. In general, velocity dispersions seen in the gas of early disk candidates are much higher than expected and imply strong feedback in the form of energy being injected into the interstellar gas (e.g., Newman et al. 2014). However, IFS+AO observations of $z \sim 1.5$ galaxies have found systems with lower SFR which are consistent with rotationally stable disks with lower intrinsic velocity dispersions (e.g., Wright et al. 2009; Wisnioski et al. 2011), which may indicate an evolution in the settling of disks. Seeing-limited slit-based spectroscopic observations have also shown that most galaxies have large V/σ values at $z \sim 1$ while only a small fraction of galaxies have high V/σ values at $z \sim 2$, implying a rapid evolution of disks in this 5 Gyr period (Kassin et al. 2012).

IFS observations of $z \gtrsim 1.5$ galaxies have shown that the most luminous star-forming galaxies have turbulent velocity dispersions, and the sites of star formation occur in large ($\gtrsim 1 \text{ kpc}$) “clumps” or concentrated “complexes” of star formation. These star-forming “clumps” are embedded in the rotation curves of these turbulent disks at high redshift and share similar velocity dispersions, and the observations suggest that clumps form at sites of disk instability (Genzel et al. 2011; Newman et al. 2013). WFC3 slitless grism observations have measured the properties of $z \sim 1$ star-forming regions, which have large $H\alpha$ sizes and fluxes, indicating a large variation in

the $H\alpha$ sizes within the population (half-light radii of 1–15 kpc; Nelson et al. 2012, 2013; Wuyts et al. 2012; Lang et al. 2014). Scaling relations of high-redshift star-forming clumps relating $H\alpha$ size, velocity dispersion, luminosity, and mass have been explored (Genzel et al. 2011; Wisnioski et al. 2011, 2012; Livermore et al. 2012, 2015). Each of these studies is able to relate the size–luminosity and size–velocity dispersion in these systems, and some find that there are luminosity offsets of high-redshift clumps compared to local H II regions (Jones et al. 2010; Livermore et al. 2012). Other IFS studies find that high-redshift clumps follow a similar trend and power law to that of local H II regions (Wisnioski et al. 2012), and investigations of whether there is redshift evolution between these samples have been explored and have contrary implications (Livermore et al. 2015). There are various observational selection differences between all IFS samples, from lensed systems to non-lensed to varying redshift and mass bins, but the number of high-redshift IFS observations is limited.

Thus far, IFS+AO observations of high-redshift galaxies have been limited to $z \sim 1.5$ and $z \sim 2$ where the prominent $H\alpha$ emission line is redshifted into the H and K bands where AO performance is better and instruments are more sensitive. In 2010, a new, powerful, center-launching laser guide star (LGS) AO was installed on Keck I (Chin et al. 2010, 2012). In 2012, our team installed a new grating on OSIRIS and increased its sensitivity by a factor of 1.5 to 2 (Mieda et al. 2014). With these factors combined, we are now capable of observing large samples of “normal” $z \sim 1$ galaxies with an IFS+AO. Selection of targets is still limited by available tip-tilt (TT) stars, but this criterion does not bias our sample selection. In this paper, we present the first result of the Intermediate Redshift OSIRIS Chemo-Kinematic Survey (IROCKS), an AO enhanced IFS study of $z \sim 1$ star-forming galaxies using OSIRIS at the Keck I telescope. We focus on the kinematics and morphological properties of $z \sim 1$ galaxies traced by $H\alpha$ emission.

This paper is organized as follows. In Section 2, we detail our sample selection, OSIRIS observations, and data reduction. We present morphology, kinematics, and disk fitting results in Sections 3, 4.1, and 4.2, respectively. Gas and dynamical mass estimates are described in Section 5. In Section 6, we introduce our definition of clumps and describe their properties. Finally, we summarize our survey in Section 7. Throughout this paper, we adopt the concordance cosmology with $\Omega_m = 0.306$, $\Omega_\Lambda = 0.692$, and $H_0 = 67.8 \text{ km s}^{-1} \text{ Mpc}^{-1}$ (Planck Collaboration et al. 2014), where 1 arcsec is 8.2 kpc at $z = 1$. For comparisons with other cosmologies used in other IFS high-redshift galaxy studies, comoving distances are different from the Planck cosmology by $<3\%$.

2. OBSERVATION AND DATA REDUCTION

2.1. Sample Selection

We select $z \sim 1$ galaxies in several well-studied fields using four surveys: the Team Keck Treasury Redshift Survey (TKRS; Wirth et al. 2004) in the Great Observatories Origins Deep Survey (GOODS)-North; the European Southern Observatory–GOODS (ESO–GOODS; Vanzella et al. 2008) spectroscopic program in GOODS-South; DEEP2 (Newman et al. 2013a and references therein) (R.A. = 02h, 14h, and 23h); and the Cosmic Assembly Near-infrared Deep Extragalactic Legacy Survey (CANDELS)–Ultra Deep Survey (UDS; Galametz et al.

2013). We target rest-frame $H\alpha$ and [N II] emission lines in the J-band, which corresponds to a redshift range of 0.8–1.1. We also target a few $z \sim 1.5$ galaxies, whose $H\alpha$ lines fall in the H-band ($1.2 < z < 1.8$). Objects are ranked in observational priority based on the following criteria: (1) the galaxy must have an accurate spectroscopic redshift; (2) the target’s shifted $H\alpha$ line must be located in regions of the J/H-band free from strong OH sky emission lines; (3) filter and atmosphere transmissions need to be high ($\gtrsim 0.7$); (4) there must be a nearby TT star with an R-band magnitude below 17 mag within $50''$ from the galaxy; and (5) a higher inferred $H\alpha$ flux, and hence SFR, is preferred. To estimate the SFR, we infer $H\alpha$ spectroscopic flux from previous $H\beta$ or [O II] detections when available. Assuming Case-B recombination, intrinsic flux ratios are estimated as $H\alpha/H\beta = 2.8$, and $H\alpha/[O II] = 1.77$ (Osterbrock 1989; Mouhcine et al. 2005), not including extinction. Using these relations, we infer the $H\alpha$ fluxes for objects in the TKRS ($H\beta$ for $z \sim 1$ and [O II] for $z \sim 1.5$ sources). For ESO–GOODS and DEEP2 targets, information on line fluxes are not available, and we estimate [O II] line fluxes using their rest-frame B-band magnitude (Mostek et al. 2012) and then convert to SFR. Objects in the UDS field also do not have line flux information available, and we use their K-band magnitudes, which have been shown to correlate with SFR (Reddy et al. 2005; Erb et al. 2006a), to rank those objects. Lastly, we prioritized sources that have complementary *Hubble Space Telescope* (HST) imaging. This provides accurate offsets between the galaxies and their TT stars, can aid in morphological comparisons between UV and optical line emissions, and helps choose galaxies that are neither too diffuse nor unresolved, to increase expected signal detection. Two fields, DEEP2 2d and 23d, are still targeted even though they do not have HST imaging available because they contain key spectroscopic information along with seeing-limited imaging from the Canada–France–Hawaii Telescope and Sloan Digital Sky Survey.

In total, we observed twenty-five $z \sim 1$ and two $z \sim 1.5$ systems and successfully detected sixteen $z \sim 1$ and one $z \sim 1.4$ systems. Table 1 summarizes the IROCKS observations.

2.1.1. TKRS Sample

TKRS (Wirth et al. 2004) is a deep spectroscopic survey in GOODS-North undertaken with a visible, multi-slit spectrograph, the DEEP Imaging Multi-Object Spectrograph (DEIMOS; Faber et al. 2003), on the Keck II telescope. It provides accurate redshift measurements of more than 1500 magnitude-limited objects to $R_{AB} = 24.4$ mag. To estimate $H\alpha$ fluxes, we use $H\beta$ and [O II] emission line fluxes for $z \sim 1$ and $z \sim 1.5$ galaxies, respectively. These $H\beta$ and [O II] emission lines were measured from flux-calibrated spectra as described by Juneau et al. (2011), but were not corrected for underlying Balmer absorption. The GOODS-North field has a wealth of optical HST imaging data available. We observed nine $z \sim 1$ and two $z \sim 1.5$ sources from TKRS and successfully detected three $z \sim 1$ (7187, 9727, and 7615) and one $z \sim 1.4$ (11169) sources. 11169 is the only source observed in the H-band in our sample.

2.1.2. ESO–GOODS Sample

We select our GOODS-South targets from the spectroscopic campaign of Vanzella et al. (2008). The data were taken by the UV FOCal Reducer and low-dispersion Spectrograph (FOR2;

Table 1
IROCKS Observation Summary

Survey	ID	z_0^a	R.A. J2000.0	Decl. J2000.0	Date yy/mm	t_{exp}^b	Filter	θ_{TT}^c ($''$)	R_{TT}^d	θ_{sm}^e (pixel)	θ_{PSF}^f ($''$)
Detected											
UDS	11655	0.8960	02 16 58.0	−05 12 42.6	13/08	9	Jn2	18.0	16.0	2.0	0.24/0.49
UDS	10633	1.0300	02 17 15.6	−05 13 07.6	13/08	4	Jn3	21.4	16.5	2.0	0.23/0.48
DEEP2	42042481	0.7934	02 31 16.4	+00 43 50.6	14/11	10	Jn1	23.2	15.4	2.0	0.26/0.52
ESO-G	J033249.73	0.9810	03 32 49.7	−27 55 17.4	14/09	5	Jn3	23.6	15.5	3.0	0.24/0.52
TKRS	11169	1.43249	12 36 45.8	+62 07 54.3	13/01	6	Hn2	33.7	16.4	2.0	0.37/0.55
TKRS	7187	0.84022	12 37 20.6	+62 16 29.7	13/05	8	Jn1	48.3	14.4	2.5	0.23/0.48
TKRS	9727	0.90316	12 37 05.9	+62 11 53.6	13/05	6	Jn2	46.9	14.0	2.5	0.53/0.68
TKRS	7615	1.01268	12 37 31.1	+62 17 14.7	13/01	6	Jn3	34.3	15.4	2.5	0.48/0.68
DEEP2	11026194	0.9198	14 15 43.0	+52 09 07.6	14/06	7	Jn2	15.1	13.5	2.5	0.33/0.57
DEEP2	12008898	0.9359	14 16 55.5	+52 27 51.3	13/05	10	Jn2	20.6	16.0	1.5	0.28/0.39
DEEP2	12019627	0.9040	14 18 49.8	+52 38 08.3	13/05	9	Jn2	49.7	16.4	2.0	0.23/0.37
DEEP2	13017973	1.0303	14 20 13.1	+52 56 13.7	12/06 ^g	9	Jn3	28.8	15.3	2.5	0.39/0.71
DEEP2	13043023	0.9715	14 20 15.8	+53 06 43.2	14/06	6	Jn3	35.6	13.7	2.5	0.42/0.59
DEEP2	32040603	1.0327	23 28 28.3	+00 21 55.9	14/11	5	Jn3	37.9	14.7	2.5	0.23/0.54
DEEP2	32016379	0.8335	23 29 36.6	+00 06 12.8	13/08	9	Jn1	18.8	16.8	2.0	0.27/0.42
DEEP2	32036760	0.8534	23 30 32.8	+00 20 06.9	13/08	7	Jn1	36.7	15.5	2.5	0.34/0.63
DEEP2	33009979	0.9797	23 31 56.3	−00 02 32.0	13/08	6	Jn3	41.1	13.0	2.0	0.20/0.42
Nondetection											
UDS	11557	0.9180	02 17 24.4	−05 12 52.2	14/11	4	Jn2	29.3	12.6	...	0.18
DEEP2	42042017	0.8070	02 28 38.0	+00 40 14.0	14/11	3	Jn1	33.1	14.2	...	0.14
TKRS	3447	0.83457	12 36 02.9	+62 12 01.4	12/06 ^g	5	Jn1	21.3	13.6	...	0.26
TKRS	4512	0.84047	12 36 08.6	+62 11 24.4	14/05	3	Jn1	37.0	13.6	...	0.24
TKRS	9867	0.85652	12 37 09.0	+62 12 02.0	14/06	2	Jn1	31.2	14.0	...	0.15
TKRS	9725	1.52079	12 37 18.6	+62 13 15.1	13/05	2	Hn3	33.2	15.8	...	0.31
TKRS	10137	0.90890	12 37 19.6	+62 12 56.2	13/05	3	Jn2	14.5	15.8	...	0.31
TKRS	3811	0.87026	12 37 22.6	+62 20 46.5	13/05	3	Jn1	17.9	13.2	...	0.22
TKRS	7078	0.95492	12 37 40.4	+62 18 53.4	14/06	3	Jn2	19.8	12.8	...	0.22
DEEP2	12027936	1.0385	14 19 26.5	+52 46 09.5	13/05	3	Jn4	42.3	16.7

Notes.

^a Spectroscopic redshift from the original selected survey.

^b Exposure time, multiple of 900 s.

^c Angular separation to the TT star.

^d R magnitude of the TT star.

^e FWHM of spatial smoothing Gaussian in pixel unit. 1 pixel = 0.1 arcsec.

^f FWHM of PSF during on-axis TT star observation before/after spatial smoothing in arcseconds.

^g Observation made before OSIRIS grating upgrade.

Appenzeller et al. 1998) on UT2 at the VLT. Their spectroscopic sample was selected by photometric colors and redshifts. The final ESO–GOODS catalog provides more than 850 redshift measurements. We use the relation between [O II] and the rest-frame B-band magnitude shown by Mostek et al. (2012) to estimate $H\alpha$ fluxes from the rest-frame B-band magnitude. In the GOODS–South field, *HST* optical observations are available, and we use them to eliminate diffuse sources. We observed and detected only one source, J033249.73, in ESO-G.

2.1.3. DEEP2 Sample

DEEP2 is a redshift survey to study the universe at $z \sim 1$ (Newman et al. 2013a, and references therein). The observations were made by the visible wavelength Low Resolution Imaging Spectrograph (Oke et al. 1995; Rockosi et al. 2010) at Keck I and DEIMOS at Keck II. It provides more than 38,000 reliable redshift measurements. We select sources in 02h (SDSS deep strip), 14h (EGS—Extended Groth Strip), and 23h

(SDSS deep strip). As GOODS–South sources, we use rest-frame B-band magnitudes to estimate $H\alpha$ fluxes. Multiple optical *HST* data are available for the EGS field, but not the 02h and 23h fields. We eliminate diffuse sources from EGS using *HST* images, but sources in the 02h and 23h fields are only selected from their expected $H\alpha$ flux. We observed six sources in EGS, four in 23h, and two in 02h field, and detected five (11026194, 12008898, 12019627, 13017973, 13043023) in EGS, all four (32040603, 32016379, 32036760, 22009979) in 23h, and one (42042481) in 02h.

2.1.4. UDS Sample

CANDELS at UDS provides the multi-wavelength (UV to mid-IR) catalog. Among about 36,000 F160W-selected sources, 210 sources have spectroscopic redshift measurements (Galametz et al. 2013). At the time of observation, SFR estimates were not available, and we used existing K-magnitude measurements to prioritize our samples (Erb et al. 2006a). The UDS field has both optical and near-IR *HST*

imaging data. We observed three sources in UDS, and detected two (11655 and 10633) sources.

2.2. OSIRIS Observations

IROCKS galaxies were observed with OSIRIS (Larkin et al. 2006) at the W. M. Keck Observatory at Mauna Kea in 2012 June, 2013 May/August, and 2014 May/June/September. OSIRIS is a diffraction-limited IFS with moderate spectral resolution ($R \sim 3800$). It uses a lenslet array as the sampling element on the sky to achieve low noncommon path error (<30 nm rms). In 2012 December, the OSIRIS grating was upgraded, and the final throughput was improved by a factor of 1.83 on average between the old grating at Keck II and the new grating at Keck I between 1 and $2.4 \mu\text{m}$ (Mieda et al. 2014). All IROCKS observations were made after OSIRIS was transferred to Keck I. Only one target, DEEP2-13017973, was observed with OSIRIS before the grating upgrade.

Our observations use OSIRIS LGS-AO in the coarsest plate scale, $0''.1$ per spaxel, corresponding to ~ 800 pc at $z \sim 1$, which gives the highest sensitivity to low surface brightness emission. All observations are made in one of the narrowband J and H filters (5% bandpasses) in order to observe both $H\alpha$ and [N II] simultaneously. This combination of plate scale and filter produces a field of view of roughly $4''.8 \times 6''.4$, which is sufficient to encompass the entire galaxy and support small $\sim 2''$ dithers between exposures on source. For each galaxy we also observe at least one pure sky pointing to ensure proper sky subtraction.

The standard observation procedure is as follows: we acquire a TT star at the optimal position angle (P.A.) and take a pair of 30 s integrations (center and $\sim 1''.5$ offset) to check the centering and measure the point-spread function (PSF). Once the telescope pointing matches with the sky, we apply a blind offset and move to the target galaxy. After the AO loop is closed, we take three 900 s exposures in up, down, and center positions. Typically, the up and down positions are separated by 2.2 arcsec. While taking the third frame, the second frame is subtracted from the first. When $H\alpha$ is detected in the first frame, we stay on the target for 1.5h–2.5h to achieve a high S/N. A different dither offset is used in each exposure to avoid any bad pixel contamination. At the end of each night, we observe an Elias standard star with all filters used that night.

There are two potential problems relating to our target selection that may produce bias in our sample. First, for estimating $H\alpha$ line fluxes to rank our targets, we used B or K broadband magnitudes for all targets, except for TKRS targets, which have existing $H\beta$ line fluxes (Section 2.1). However, there are no existing empirical data to show a direct correlation between the galaxies' B or K broad band magnitudes and $H\alpha$ fluxes, and we only used it because of a lack of alternatives. A more thorough, but also more expensive, approach would be to perform a pre-survey using a near-IR multi-slit spectrograph, such as MOSFIRE (McLean et al. 2010, 2012), to measure the galaxies' global $H\alpha$ fluxes.

Second, during observation, we visually inspected the data after the first 900 s exposure to decide whether to continue with a longer exposure. Arguably, 900 s may not be sufficient to judge whether the target is a non-detection. Additionally, because our non-TKRS targets have poor $H\alpha$ flux estimates, we spent more time on them, thus potentially generating sample bias. While we do not consider these effects significant,

future observations will benefit from a more rigorous methodology.

2.3. OSIRIS Data Reduction

Data reduction is performed using the OSIRIS data reduction pipeline (DRP) version 3.2 and custom IDL routines. Before we run DRP, we use our own custom IDL code to correct the rectification matrices. The rectification matrices are maps of lenslet PSFs and are required to extract spectra by DRP. Since the upgrade of the OSIRIS grating and calibration unit, the newly taken matrices have created artificial bad pixels in the reduced cube as they iteratively extract spectra. To resolve this issue, we replace any matrix entry >0.8 with its neighbor mean. With the corrected rectification matrices, we first combine several dark frames of that night by DRP to make a master-dark. We then run DRP again to subtract the master-dark, adjust channel levels, remove crosstalk, detector glitches, and cosmic rays, extract spectra using the corrected rectification matrices, assemble data cube and, finally, correct for atmospheric dispersion. After this, we run our own cleaning code on the cube, which, for a given channel, iteratively replaces pixel values with the median of its neighboring pixels, if its original value is more than $15 \sigma_\lambda$ (standard deviation per channel) away from the spatial median.

After we obtain the cleaned, dark-subtracted cubes, we experiment with two sky-subtraction methods, *simple subtraction* and *scale subtraction*, using *pure sky* and *pair sky*. Pair sky is another science frame where the galaxy's location on the detector does not overlap with the current science frame. Simple subtraction, as its name implies, is a simple subtraction of a sky cube from a science cube. Scale sky subtraction, on the other hand, uses an algorithm from Davies (2007) that scales OH sky emission lines between adjacent frames to reduce sky-subtraction residuals. The final choice of sky and subtraction method is determined by examining the resultant standard deviation in spectral space; a lower standard deviation (i.e., less noisy) was deemed better.

The scale subtraction method reduces 76% of the frames, among which 58% are with pure sky. Pure sky frames are used more by the scale subtraction method than pair sky frames are. Furthermore, we additionally subtract a channel-dependent constant to the sky-subtracted cube that ensures the median value in the regions away from the source is zero. We then mosaic the reduced cubes using the DRP with the "meanclip" combine method with LGS offset.

The effect of sky subtraction can be seen clearly in Figure 1. We are able to largely remove contamination from sky emission lines and recover a well-defined $H\alpha$ emission line from the galaxy. In the end, an additional bad-pixel-removal algorithm is used to replace single, isolated, high-value (6σ or 7σ above the spatial median) pixels that are outside of the expected galaxy vicinity, with the spatial median of the given channel. To increase the S/N, the cleaned mosaic-ed cube is spatially smoothed by a Gaussian function of FWHM = 1.5 to 3.0 pixel ($0''.15$ to $0''.3$). The smoothing FWHM is chosen by our custom "adaptive smoothing" code. The details of this method are documented in Appendix A. Finally, flux calibration is done using the Elias telluric standard stars observed on each night.

The error, or uncertainty, in our data is defined by the spatial standard deviation within the region where all mosaic-ed frames are overlapped, for a given channel. Therefore our error

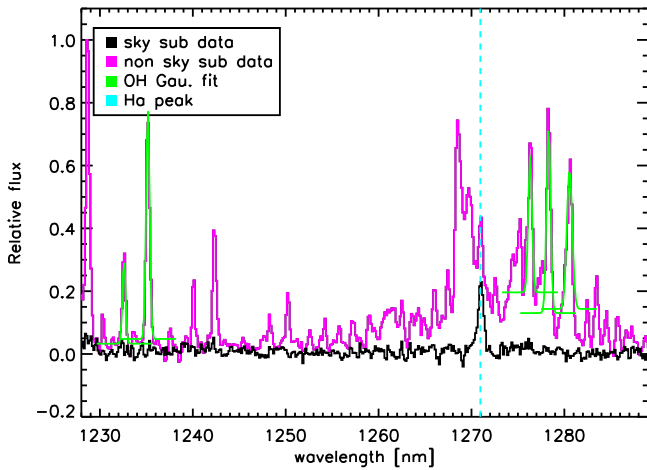


Figure 1. An example of unsmoothed non-sky-subtracted (magenta) and fully reduced (black) spectra at a single, bright spaxel of a DEEP2 galaxy, 12008898 ($z = 0.936$). The location of the $H\alpha$ emission line peak is shown by a cyan vertical line. Brighter OH lines that are well separated are fitted by a Gaussian profile (green) to obtain the instrumental width at that spaxel.

is wavelength-dependent, and spatially invariant. The only exception is where not all frames are overlapped. There we scale the error by $\sqrt{n_{\max}/n}$, where n is the number of frames used at that spaxel, and n_{\max} is the maximum number of frames used in the cube.

2.3.1. $H\alpha$ Maps

$H\alpha$ flux maps are created by cross-correlating a normalized Gaussian profile of a typical $H\alpha$ width ($\sigma = 1.5$ channel ~ 50 km s^{-1} at $z = 1$) with the spectrum at each spaxel to find a correlation peak. We then sum up five channels (~ 170 km s^{-1}) centered on this peak to represent $H\alpha$ flux. The noise map is made by adding the error in the same five channels in quadrature. When the correlation peak does not coincide with the peak of Gaussian fitting (see Section 4.1 for Gaussian profile fitting to $H\alpha$ lines), we instead use five channels around the redshift from the original surveys, z_0 (shown in Table 1). In this case, we consider it a non-detection, and the calculated flux reflects the background level. Two [N II] lines, [N II]6549 and [N II]6583, are simultaneously observed with the $H\alpha$ line. Both [N II] lines are well separated (~ 20 and ~ 28 channels, respectively, from $H\alpha$ line at $z = 1$), and $H\alpha$ maps are not contaminated by [N II] line fluxes. Since [N II] detection is significantly weaker than $H\alpha$, we do not cross-correlate our spectra to locate it. Rather, we infer its location from the detected $H\alpha$ line, and make its flux map and associated error map by summing up five channels centered on that inferred offset in the spectral dimension. *HST* images (when available) and the resultant $H\alpha$ flux maps are shown in Figure 13 below in the left and second left panels, respectively.

2.3.2. 1D Spectra

We define an $H\alpha$ segmentation map for each galaxy using the S/N. Spaxels whose $S/N_{H\alpha} < 3$ or Gaussian-fitted $S/N_{H\alpha}^G$ (integration of Gaussian parameters with propagated error, see Section 4.1 for Gaussian fitting) < 1.5 are masked out. We then apply final visual inspection to mask out bad spaxels. The integrated 1D spectra of the IROCKS samples (top panel of Figure 14) are created by summing up all spaxels in the $H\alpha$

segmentation map. A single Gaussian profile is fitted to the $H\alpha$ emission line in each 1D spectrum to obtain the peak wavelength and integrated width. From the peak wavelength, we measure a systemic redshift (z_{sys}), and from the width, corrected for the instrumental resolution, the global 1D velocity dispersion (σ_{1D}) is obtained. This 1D dispersion σ_{1D} (sometimes called σ_{net} or σ_{global} ; Law et al. 2009; Wright et al. 2009; Wisnioski et al. 2011) is not corrected for terms such as rotation and outflows. In Section 4.1, we discuss another velocity dispersion value, σ_{ave} , which more accurately measures the line-of-sight velocity dispersion.

We note that instrumental resolution varies across the field of view, and for σ_{1D} , we use a spatial average of instrumental width for correction. To calculate the spatially varying instrumental width, we measure the widths of OH lines in non-sky-subtracted data (see the example of OH lines in Figure 1). The procedure is as follows: we first smooth the non-sky-subtracted data with a Gaussian function of the same width as that used for the science data. Using a Gaussian fit, we then measure the widths of bright OH lines that are well separated (> 5 channels) from other OH lines. This results in a few width measurements per spaxial in an individual sky data cube. Since the final science frame is mosaic-ed together at different dither patterns, the instrumental width per spaxel is an average of all the frames combined. We do not see a width trend in wavelengths, and thus we only obtain spatially but not spectrally varying instrumental width. We find that the typical instrumental width corresponds to ~ 45 km s^{-1} , and spatial variation is about 10%.

2.3.3. Multiple Components in Each Galaxy

When there is only a single $H\alpha$ peak in the 1D spectrum, the object is classified as a “single” component source: 11655, 10633, 42042481, J033249.73, 9727, 7615, 11026194, 13017973, 13043023, 32040603, 32016379, and 32036760. When there is more than one peak, we spatially separate them and treat them as different components, and the galaxy is classified as a “multiple” $H\alpha$ source: 11169 (east and west), 7187 (east and west), 12019627 (north, south-east, and south-west), and 33009979 (north and south). There are two special cases: first, the spectrum of 12008898 only has one spectral peak in the 1D spectrum, but on both *HST* and $H\alpha$ maps, its north and south components are spatially separated by $\theta \sim 2''$ (~ 3 kpc), so we categorize it as multiple (north and south); and second, the west component of 7187 has more than one spectral peak in 1D spectrum even after it has been separated from the east component, but the peaks cannot be spatially separated, and hence we treat it as a single component. Due to multiple peaks, σ_{1D} and other parameters for the west component of 7187 are not well measured. In Appendix E, each component is separately shown in Figure 15.

2.3.4. Global Fluxes and SFRs

Like the top panels of Figure 14, the bottom panels are integrated spectra from the segmentation maps, but each $H\alpha$ line spectrum has been shifted to coincide to the same wavelength (i.e., matching each spaxel Gaussian fitting peak to the same systemic redshift, z_{sys}). This procedure removes all large-scale velocity trends, such as rotation, from the line width, and is useful for increasing the S/N of $H\alpha$ and boosting the detection of [N II]. We obtain the global $H\alpha$ and [N II]

Table 2
Emission Line Fluxes

ID	z_{sys}^a	$f_{\text{H}\alpha}^b$	$f_{[\text{N II}]}^c$	$\log\left(\frac{[\text{N II}]}{\text{H}\alpha}\right)$
11655	0.8962	20.1 ± 5.0	4.9 ± 4.4	-0.61 ± 0.40
10633	1.0318	4.1 ± 2.3
42042481	0.7940	43.0 ± 7.8	15.2 ± 6.8	-0.45 ± 0.21
J033249.73	0.9813	10.8 ± 4.3	3.8 ± 6.1	-0.45 ± 0.71
11169E	1.4344	14.8 ± 3.4	2.3 ± 4.2	-0.80 ± 0.79
11169W	1.4330	21.5 ± 3.6
7187E	0.8404	7.1 ± 2.9	2.3 ± 4.0	-0.49 ± 0.78
7187W	0.8409	6.0 ± 2.9	1.4 ± 5.2	-0.62 ± 1.59
9727	0.9038	28.2 ± 6.2	13.3 ± 6.0	-0.33 ± 0.22
7615	1.0130	15.4 ± 5.1	3.4 ± 3.6	-0.66 ± 0.48
11026194	0.9205	14.3 ± 4.0	2.6 ± 3.5	-0.74 ± 0.59
12008898N	0.9362	5.5 ± 4.3	0.6 ± 2.4	-0.94 ± 1.68
12008898S	0.9364	55.0 ± 9.4	22.2 ± 44.2	-0.39 ± 0.87
12019627N	0.9037	8.8 ± 3.5	1.8 ± 4.4	-0.69 ± 1.08
12019627SE	0.9045	15.3 ± 4.8
12019627SW	0.9059	9.7 ± 3.5	<0.2	<-1.70
13017973	1.0309	71.8 ± 19.6	9.9 ± 16.0	-0.86 ± 0.71
13043023	0.9716	27.1 ± 8.2	7.6 ± 8.0	-0.55 ± 0.47
32040603	1.0338	10.8 ± 3.4	<0.1	<-2.04
32016379	0.8339	20.0 ± 5.2	4.7 ± 4.0	-0.62 ± 0.38
32036760	0.8519	16.7 ± 3.7	5.0 ± 2.8	-0.52 ± 0.26
33009979N	0.9817	12.0 ± 4.2	3.5 ± 4.3	-0.53 ± 0.55
33009979S	0.9799	44.2 ± 9.5	8.3 ± 6.9	-0.73 ± 0.37

Notes.

^a Redshift measured from OSIRIS H α detected emission line.

^b Global H α emission line fluxes obtained by fitting Gaussian profiles to the shifted integrated 1D spectra, in units of 10^{-17} erg s $^{-1}$ cm $^{-2}$.

^c Global [N II] emission line fluxes obtained by fitting Gaussian profiles to the shifted integrated 1D spectra, in units of 10^{-17} erg s $^{-1}$ cm $^{-2}$.

fluxes by fitting Gaussian profiles to these shifted integrated 1D spectra, and computing the integral of the fitted Gaussian curves. We also obtain the flux uncertainties using the errors in the fitted parameters.

To convert H α fluxes into luminosities, we use a standard cosmological model (see Section 1), and correct for dust extinction, assuming a spatially constant optical depth derived from stellar population models (Section 2.4). These H α luminosities are then converted to SFR using the method of Kennicutt (1998) modified by the initial mass function of Chabrier (2003):

$$\text{SFR} [M_{\odot} \text{ yr}^{-1}] = \frac{L_{\text{H}\alpha}}{2.23 \times 10^{41} [\text{erg s}^{-1}]} \quad (1)$$

The systemic redshift, non-extinction-corrected integrated fluxes of H α and [N II], and [N II] to H α line ratio of each component are summarized in Table 2. In our $z \sim 1$ sample, H α flux spans between 4.1 to 71.8×10^{-17} erg s $^{-1}$ cm $^{-2}$, and the average is 21.2×10^{-17} erg s $^{-1}$ cm $^{-2}$. In this paper, we report the global [N II]/H α ratio, but not its spatial variation. We defer the analysis of spatially resolved [N II]/H α to future work. The extinction-corrected/non-corrected H α luminosity and SFR are reported in Table 3. The following section describes the extinction correction factor.

2.4. Stellar Population Modeling

We make use of publicly available photometric catalogs for each source to construct a consistent spectral energy

distribution (SED) and stellar population fit to estimate stellar masses, optical depths, and SFRs. For the four TKRS galaxies in GOODS-North, we use the photometric catalog from version 4.1 3D-*HST* release (Skelton et al. 2014). This catalog contains 22 bands: seven *HST*, four *Spitzer*, and nine ground-based, ranging from 0.3 to 8.0 μm . For our single ESO-GOODS source, we use the GOODS/ISAAC final data release, version 2.0 (Retzlaff et al. 2010) for J, H, and K photometry, and GOODS/FORS2 final data release version 3.0 for $i - z$, $V - i$, and $B - V$ (Vanzella et al. 2008). For the ten DEEP2 sources in our sample, we use the extended photometry catalog of DEEP2 Galaxy Redshift Survey data release 4 (Matthews et al. 2013), containing *ugriz* photometry. For the two UDS sources, we use the CANDELS UDS Multiwavelength catalog (Galametz et al. 2013), which contains 19 bands: four *HST*, four *Spitzer*, and ten ground-based, ranging from 0.3 to 8.0 μm . For consistency, our SED fitting uses only ground-based photometry in the 0.3–2.3 μm range.

The SED fitting method used in this study is further described in Salim et al. (2007, 2009). In short, the method uses the stellar population synthesis models of Bruzual & Charlot (2003), with an exponentially declining continuous SFR with random stochastic bursts superimposed, a range of metallicity (0.1 to 2 Z_{\odot}), and a Chabrier IMF (Chabrier 2003). Each model is attenuated according to a two-component prescription of Charlot & Fall (2000), whose extinction curve is age-dependent and typically steeper than the Calzetti (2001) curve. The model assumes extra attenuation toward H II regions, where young stars are embedded within dense birth clouds as well as the interstellar medium (ISM) in the galaxy at $t < 10^7$ yr. At $t > 10^7$ yr, the birth cloud disappears and only ISM attenuation is considered. We define a total optical depth, τ_V , to indicate attenuation from both H II and ISM, and $\mu\tau_V$ for ISM only attenuation. The coefficient μ is determined from SED fitting, and in our sample, the average μ is 0.48.

Individual values for stellar mass (M_*), τ_V , μ , and SFR (SFR $_{\text{SED}}$) obtained by SED fitting are tabulated in Table 3. The table also contains uncorrected, ISM-only corrected, and H II +ISM-corrected H α luminosities ($L_{\text{H}\alpha}$, $L_{\text{H}\alpha}^0$, and $L_{\text{H}\alpha}^{00}$), and the SFRs estimated from these luminosities (SFR $_{\text{H}\alpha}$, SFR $_{\text{H}\alpha}^0$, and SFR $_{\text{H}\alpha}^{00}$). The comparison of these three versions of SFR $_{\text{H}\alpha}$ with respect to SFR $_{\text{SED}}$ is shown in Figure 2. H II+ISM corrected SFR $_{\text{H}\alpha}$ best agrees with SFR $_{\text{SED}}$, as shown by the black best-fit line in Figure 2, which has a power of 0.81, mean SFR $_{\text{H}\alpha}/\text{SFR}_{\text{SED}} = 0.86$, and $\chi^2 = 1.24$.

Most IFS studies of high-redshift galaxies assume $E(B - V)_{\text{stellar}} = E(B - V)_{\text{nebular}}$ (e.g., Law et al. 2009; Wright et al. 2009; Wisnioski et al. 2011; Queyrel et al. 2012). On the other hand, the SINS survey (Förster Schreiber et al. 2009) used a locally found relation, $E(B - V)_{\text{stellar}} = 0.44E(B - V)_{\text{nebular}}$ (Calzetti 2001), and found a better agreement between H α - and UV-continuum-estimated SFR of $z \sim 2$ galaxies. More recent studies (e.g., Kashino et al. 2013; Pannella et al. 2015) found $E(B - V)_{\text{stellar}} \sim 0.75E(B - V)_{\text{nebular}}$ over the redshift range $0.5 < z < 4$, with more massive galaxies being more dust attenuated. Even though the emission lines are not attenuated by the same amount as the stellar continuum, and extra attenuation toward H II region may be more appropriate, in this paper, we use ISM-only extinction corrected values, otherwise specified, to be consistent with other IFS studies. Figure 3 shows the instantaneous global SFR estimated from H α luminosity as a function of redshift. Major IFS high-redshift

Table 3
Stellar Population Parameters

ID	$\log(M_*[M_\odot])^a$	τ_V^b	μ^c	$L_{H\alpha}^d$ (10^{41} erg s $^{-1}$)	$L_{H\alpha}^0^e$ (10^{41} erg s $^{-1}$)	$L_{H\alpha}^{00f}$ (10^{41} erg s $^{-1}$)	$SFR_{H\alpha}^g$ (M_\odot yr $^{-1}$)	$SFR_{H\alpha}^0^h$ (M_\odot yr $^{-1}$)	$SFR_{H\alpha}^{00i}$ (M_\odot yr $^{-1}$)	SFR_{SED}^j (M_\odot yr $^{-1}$)
11655	10.2 ± 0.1	2.07 ± 0.21	0.72	8.5 ± 2.1	28.7 ± 7.9	46.0 ± 13.8	3.8	12.9	20.6	67.6
10633	11.2 ± 0.0	3.43 ± 0.40	0.62	2.4 ± 1.3	13.9 ± 8.2	40.3 ± 25.8	1.1	6.2	18.1	39.8
42042481	10.6 ± 0.2	0.75 ± 0.48	0.42	13.5 ± 2.5	17.4 ± 4.3	24.9 ± 10.8	6.0	7.8	11.1	16.6
J033249.73	10.5 ± 0.1	0.88 ± 0.37	0.60	5.7 ± 2.3	8.8 ± 3.8	11.7 ± 5.8	2.6	3.9	5.2	4.0
11169E	10.8 ± 0.1	1.02 ± 0.84	0.21	19.9 ± 4.6	23.7 ± 6.4	45.8 ± 33.1	8.9	10.6	20.5	6.2
11169W	10.1 ± 0.0	1.06 ± 0.41	0.32	28.8 ± 4.8	38.0 ± 7.5	68.5 ± 25.6	12.9	17.0	30.7	22.9
7187	10.3 ± 0.1	1.25 ± 0.78	0.33	4.7 ± 1.5	6.6 ± 2.5	13.1 ± 9.3	2.1	3.0	5.9	7.8
7187E	2.5 ± 1.1	3.6 ± 1.7	7.1 ± 5.4	1.1	1.6	3.2	...
7187W	2.2 ± 1.0	3.0 ± 1.6	6.0 ± 4.8	1.0	1.4	2.7	...
9727	11.0 ± 0.0	3.66 ± 0.41	0.47	12.1 ± 2.7	49.5 ± 13.4	241.7 ± 96.9	5.4	22.2	108.4	158.5
7615	10.7 ± 0.1	1.29 ± 0.62	0.35	8.8 ± 2.9	12.7 ± 4.8	25.2 ± 15.3	3.9	5.7	11.3	3.8
11026194	10.2 ± 0.2	1.86 ± 0.89	0.60	6.5 ± 1.8	16.1 ± 8.3	29.5 ± 23.0	2.9	7.2	13.2	70.8
12008898N	2.6 ± 2.0	4.7 ± 3.9	7.0 ± 6.1	1.2	2.1	3.1	...
12008898S	9.9 ± 0.1	1.21 ± 0.49	0.60	25.8 ± 4.4	46.7 ± 13.8	69.4 ± 30.2	11.6	21.0	31.1	53.7
12019627N	3.8 ± 1.5	5.9 ± 2.8	9.1 ± 5.8	1.7	2.7	4.1	...
12019627S	10.0 ± 0.1	1.08 ± 0.60	0.51	10.7 ± 2.6	16.8 ± 5.8	25.9 ± 14.2	4.8	7.5	11.6	32.4
12019627SE	6.6 ± 2.1	10.4 ± 4.2	16.0 ± 9.3	3.0	4.7	7.2	...
12019627SW	4.2 ± 1.5	6.6 ± 2.9	10.1 ± 6.2	1.9	2.9	4.5	...
13017973	10.6 ± 0.2	1.51 ± 0.64	0.65	42.7 ± 11.7	95.3 ± 41.5	146.8 ± 86.6	19.2	42.7	65.8	72.4
13043023	10.4 ± 0.1	1.96 ± 0.53	0.57	13.9 ± 4.2	34.8 ± 13.6	69.2 ± 36.6	6.3	15.6	31.0	85.1
32040603	9.6 ± 0.3	0.34 ± 0.37	0.37	6.5 ± 2.0	7.2 ± 2.4	8.5 ± 3.7	2.9	3.2	3.8	11.5
32016379	10.4 ± 0.2	0.71 ± 0.74	0.43	7.1 ± 1.8	9.1 ± 3.3	12.6 ± 8.3	3.2	4.1	5.7	17.0
32036760	10.7 ± 0.2	1.29 ± 0.73	0.52	6.2 ± 1.4	10.7 ± 4.1	17.8 ± 11.3	2.8	4.8	8.0	43.7
33009979N	6.3 ± 2.2	9.0 ± 4.1	15.0 ± 11.8	2.8	4.0	6.7	...
33009979S	10.3 ± 0.2	1.06 ± 0.86	0.41	23.2 ± 5.0	33.1 ± 11.9	55.1 ± 40.5	10.4	14.8	24.7	33.9

Notes.

^a Stellar mass derived from the SED fits.

^b Total optical depth for H II+ISM extinction.

^c Correction to the optical depth for ISM-only extinction.

^d H α luminosity not corrected for extinction.

^e H α luminosity corrected for ISM-only extinction ($\mu\tau_V$).

^f H α luminosity corrected for H II+ISM extinction (τ_V).

^g SFR estimated from uncorrected H α luminosity.

^h SFR estimated from ISM-only ($\mu\tau_V$) extinction corrected H α .

ⁱ SFR estimated from H II+ISM (τ_V) extinction corrected H α .

^j SFR estimated from SED fitting.

galaxy observations (Law et al. 2009; Wright et al. 2009; Förster Schreiber et al. 2009; Wisnioski et al. 2011; Queyrel et al. 2012) are overplotted. On this figure, whether AO is used or not is irrelevant to the global SFR estimate, but we distinguish the two cases to show which survey focuses on what redshift range with what type of observation mode.

3. MORPHOLOGIES

We quantify morphologies of star-forming regions by examining H α maps with the same segmentation criteria in Section 2.2 applied. H α flux distribution and its segmentation map are best described by Figure 13 and Figure 7. We measure a size scale and three morphological parameters for each galaxy. We define a radius of gyration, r_g as a size scale. This yields a typical distance from a given origin using the second moment of flux:

$$r_g = \sqrt{\frac{\sum_i d_i^2 f_i}{\sum_i f_i}}, \quad (2)$$

where d_i is the distance between the given origin to the i th pixel whose flux value is f_i . Our choice of origin is the flux-weighted

centroid. This is a mathematically robust way to define a galaxy size, especially for systems with asymmetric and clumpy flux distributions since it does not assume a specific galaxy model (e.g., Sérsic index). Many of our H α maps exhibit clumpy morphologies, and r_g has the additional advantage of being largely insensitive to PSF and spatial smoothing because it gives the typical distance between each clump center (a galaxy with a single concentrated nucleus has a small r_g while a galaxy with multiple nuclei has a r_g that is roughly the distance between nuclei). Compared to typical size measurements, such as a half-light radius, r_g is always smaller and more sensitive to the distribution of the light. The values of r_g are reported in Table 4. In our sample, r_g ranges from 1.0 to 7.6 kpc, and the average is 3.5 kpc. When the source has more than one distinct component (TKRS11169, DEEP2-12008898, DEEP2-12019627, and DEEP2-33009979), we also report their separation in Table 4. In our sample, the smallest source, UDS 10633, is smaller than the smoothing width and hence not resolved. However, its spectrum has a good signal at the expected redshift, so we consider this source as a real detection (not a noise spike) and retain it in our analysis. The largest

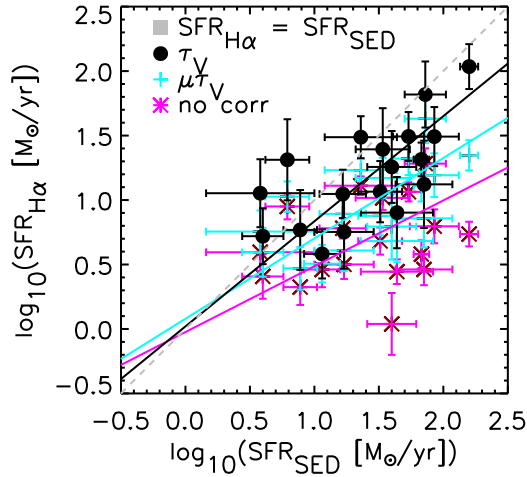


Figure 2. Comparison of SFRs with different extinction corrections derived from the SED fits. H II+ISM dust-corrected ($\text{SFR}_{\text{H}\alpha}^0$, black circle), ISM dust-only-corrected ($\text{SFR}_{\text{H}\alpha}^0$, cyan plus), and uncorrected ($\text{SFR}_{\text{H}\alpha}$, magenta asterisk) SFR estimated from H α luminosity using Kennicutt (1998) and Chabrier (2003) vs. SFR estimated from SED fitting. The one-on-one relation ($\text{SFR}_{\text{H}\alpha} = \text{SFR}_{\text{SED}}$ is shown as a gray dotted line. The average H II+ISM attenuation is $\langle\tau_V\rangle = 1.2$, and the average ISM-only attenuation is $\langle\mu\tau_V\rangle = 0.6$ ($\text{SFR}_{\text{H}\alpha}^0 = \text{SFR}_{\text{H}\alpha}e^{\tau_V}$ and $\text{SFR}_{\text{H}\alpha}^0 = \text{SFR}_{\text{H}\alpha}e^{\mu\tau_V}$). Correcting for the dust attenuation in H II region and ISM yields the best match between the derived $\text{SFR}_{\text{H}\alpha}$ and SFR_{SED} , with a best-fit line of $\log\text{SFR}_{\text{SED}} = 0.02 + 0.82 \log\text{SFR}_{\text{H}\alpha}^0$ and has mean $\text{SFR}_{\text{H}\alpha}^0/\text{SFR}_{\text{SED}} = 0.88$.

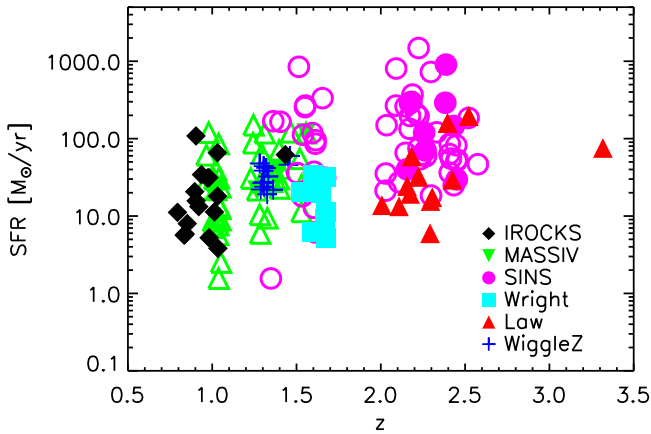


Figure 3. Global SFR of individual galaxies in the IROCKS sample compared to other high-redshift IFS samples, Wright et al. (2009), Law et al. (2009), SINS (Förster Schreiber et al. 2009), WiggleZ (Wisnioski et al. 2011), and MASSIV (Queyrel et al. 2012), as a function of redshift. The SFRs shown here are estimated from H α or [O III] fluxes using Planck cosmology (see Section 1) and are corrected for ISM-only extinction. Same symbols and colors but filled/open are AO/non-AO observations. Because this figure shows global SFR, AO/non-AO is almost irrelevant, but two cases are shown separately to highlight the differences between different surveys.

galaxy, DEEP2 13017973, has $r_g = 7.6$ kpc, but the most extended one is DEEP2 12019627, whose separation between the different components spans 24 kpc.

In Section 6, we measure the individual sizes (half-light radii) of clumps in galaxies. While the radius of gyration and the component separation distance describe the whole extent of the galaxy, the clump size describes the scale of local star-forming regions.

We also calculate three morphological parameters for our H α maps: the Gini coefficient (G ; Abraham et al. 2003), M_{20} (Lotz et al. 2004), and multiplicity (Ψ ; Law et al. 2007b). The

Table 4
H α Morphology Parameters

ID	r_g^a (kpc)	d^b (kpc)	G^c	M_{20}^d	Ψ^e
11655	2.79	...	0.22	-1.29	2.25
10633	<0.88	...	0.14	-0.88	0.32
42042481	5.88	...	0.19	-1.18	5.16
J033249.73	4.68	...	0.11	-0.74	13.78
11169	...	8.97	0.18	-0.86	10.11
11169E	2.60	...	0.11	-0.86	3.34
11169W	2.55	...	0.21	-1.30	2.30
7187	...	9.19	0.14	-0.90	12.98
7187E	2.33	...	0.16	-1.42	3.71
7187W	3.55	...	0.10	-0.61	13.34
9727	4.82	...	0.12	-0.96	6.10
7615	5.00	...	0.11	-0.69	13.11
11026194	3.07	...	0.14	-0.85	4.95
12008898	...	17.35	0.29	-1.47	7.50
12008898N	1.04	...	0.22	-1.07	1.05
12008898S	2.88	...	0.29	-1.23	3.61
12019627	...	24.20	0.18	-1.08	17.42
12019627N	4.41	...	0.17	-1.15	14.61
12019627SE	2.66	...	0.18	-1.29	4.56
12019627SW	1.87	...	0.15	-0.94	1.72
13017973	7.59	...	0.09	-0.67	16.31
13043023	4.72	...	0.11	-0.87	9.80
32040603	1.96	...	0.21	-1.33	0.53
32016379	4.32	...	0.17	-0.76	8.62
32036760	3.09	...	0.16	-1.21	0.79
33009979	...	16.37	0.31	-1.37	7.66
33009979N	2.04	...	0.16	-1.06	2.80
33009979S	2.83	...	0.31	-1.58	1.58

Notes.

- ^a Radius of gyration by H α flux with respect to the flux-weighted centroid.
- ^b Distance between two components. When there are more than two components, it is the distance between the two farthest components.
- ^c Gini parameter on a segmentation map.
- ^d Second-order moment on a segmentation map.
- ^e Multiplicity parameter on a segmentation map.

Gini coefficient is commonly used in econometrics, and when applied to galaxy morphologies it quantifies the relative distribution of galaxy flux among its constituent pixels. G is one when all light is concentrated in one pixel while it is zero when every pixel has the same value. M_{20} is the normalized second-order moment of the brightest 20% of the galaxy's flux and has low negative value when galaxies are extended with multiple nuclei and high negative value when galaxies are smooth with a bright nucleus. Ψ is designed to measure how multiple the source appears by measuring the projected potential energy of the light distribution, normalized by the most compact arrangement of the flux pixels. Low Ψ means compact single-nucleus galaxies, while high Ψ means clumpy multiple-nuclei galaxies. For example, see Figure 3 of Lotz et al. (2004) and Figure 10 of Law et al. (2007b) for how G , M_{20} , and Ψ change with different *HST* morphologies. G , M_{20} , and Ψ are listed in Table 4.

As discussed by Law et al. (2009), OSIRIS H α morphologies are difficult to compare to high-resolution rest-UV *HST* morphologies. IFS data typically have high background levels, and the special background reduction techniques employed by the OSIRIS pipeline results in highly customized segmentation maps (see Section 2.3). These segmentation maps are different

from those commonly used for imaging data, such as a quasi-Petrosian isophotal cut (Abraham et al. 2007). Even with all these techniques, we still are unable to achieve the same level of low-brightness sensitivity as narrowband data and, as a result, our G values are systematically lower than the rest-frame UV imaging data (e.g., Lotz et al. 2004; Law et al. 2007a, 2009).

Because of the extremely narrow field of view of OSIRIS, there are no reference stars that can be used for astrometric calibration between *HST* and OSIRIS data. This is another uncertainty for morphological comparisons, but we included *HST* images in Figure 13 when available, and we align the images by visual inspection. Exactly how *HST*- $H\alpha$ alignments are done changes from source to source, and the alignment details can be found in Appendix E.

4. KINEMATICS

4.1. Kinematic Maps

We create kinematic velocity maps of star-forming regions by fitting a Gaussian profile to the $H\alpha$ emission line in each spaxel. Intensity, width, center position, and constant offset are fitted, and these parameters are then converted to physical quantities of interest. The radial velocity map is obtained from the peak position with respect to $H\alpha$ at the systemic redshift (z_{sys} in Table 2). The velocity dispersion map is calculated from the width of the Gaussian function, corrected for the spatially varying instrumental resolution (see Section 2.3 for instrumental width). The third and last panels of Figure 13 in Appendix C show our radial velocity and velocity dispersion maps. For these kinematic maps, we apply the same segmentation criteria as those specified in Section 2.2.

We measure the S/N-weighted averages of velocity dispersion, σ_{ave} (sometimes referred to as σ_{mean} ; Law et al. 2009; Wisnioski et al. 2011), in our segmented kinematic maps. Since it excludes the global velocity gradient, it represents a more accurate measurement of the line-of-sight velocity dispersion compared to σ_{1D} . However, the gradient within a pixel, $0''1$ per spaxel, beam smearing, and weighting method can still potentially bias the value.

In addition to velocity dispersion, we also measure the velocity shear, v_{shear} , which is defined as a half of the maximum difference in rotational velocity, $0.5(v_{\text{max}} - v_{\text{min}})$, in a galaxy. Because the axis of rotation is not well defined in most of our galaxies, instead of v_{max} and v_{min} being maximum and minimum velocities along the kinematic major axis (e.g., Förster Schreiber et al. 2006; Law et al. 2009), we use velocities in the main bodies of the galaxies. In order to avoid possible outliers and artifacts, we use a modified version of the method by Gonçalves et al. (2010). We calculate v_{max} and v_{min} as the mean of the highest and lowest three values. Given that the inclinations of the galaxies are not well constrained, and that the depth of observation is not sufficient to detect the full spatial extent, some galaxies do not show obvious disk-like velocity gradients. For these galaxies, v_{shear} represents the best possible unbiased rotation measurement. We discuss the effect of smoothing on the kinematics in Appendix B. v_{shear} , σ_{ave} , the ratio $v_{\text{shear}}/\sigma_{\text{ave}}$, and σ_{1D} are listed in Table 5.

In Table 5, we also report a combined velocity scale, S_K . This is a velocity indicator for tracing galaxy potential well depths proposed by Weiner et al. (2006a), and is defined as $S_K \equiv \sqrt{Kv^2 + \sigma^2}$. We adopted $K = 0.5$ for a flat rotation curve

whose density profile is $\propto r^{-2}$. We use the notation of $S'_{0.5} = \sqrt{v_{\text{shear}}^2 + \sigma_{\text{ave}}^2}$ to emphasize the difference between inclination-uncorrected v_{shear} and inclination-corrected V_{rot} for $S_{0.5}$ (Kassin et al. 2012). Both $S'_{0.5}$ and σ_{1D} describe the total kinematic/potential energy of the galaxy and should have similar values, and they can serve as a consistency check. Most sources have similar values between $S'_{0.5}$ and σ_{1D} . For a few cases when they are significantly different, those sources with high v_{shear} are likely interacting or dominated by low-S/N regions in the data.

Figure 4 shows how σ_{1D} and σ_{ave} change in redshift, stellar mass, SFR, and normalized specific star formation rate (sSFR) (see Equation (9); Whitaker et al. 2012; Genzel et al. 2015). Measurements of Wright et al. (2009), Law et al. (2009), Förster Schreiber et al. (2009), Wisnioski et al. (2011), and Epinat et al. (2012) are also shown. While our σ_{1D} spans a similar, wide range of $49 < \sigma_{1D} < 150 \text{ km s}^{-1}$, as other surveys, our σ_{ave} spans very narrow range at lower values than other surveys. The narrow range may be due to the observational limitation. A value of 50 km s^{-1} corresponds to the $\sigma = 1.5$ channel. In the low-S/N regime we work in, a line narrower than this width is difficult to distinguish from noise spikes, and what we see in the IROCKS sample at $z \sim 1$ might be an upper limit. Interestingly, our only $z \sim 1.4$ source (TKRS11169) shows a higher dispersion, $\sigma_{\text{ave}} \sim 90 \text{ km s}^{-1}$, on both east and west components. A previous X-ray observation (Alexander et al. 2003) identified this source as an active galactic nucleus (AGN), and high dispersion is consistent with AGN narrow line region kinematics. However, it is unlikely that both components each host an AGN. Thus, the high dispersion we observed is most likely the kinematic evolution (higher dispersion at higher redshift) seen in the other surveys.

Weiner et al. (2006a, 2006b) show that σ_{1D} is relatively robust against observational effects to measure internal kinematics of galaxies, and can be used to study the Tully–Fisher (TF) relation with a large scatter. The second and third panels of Figure 4 on the top row are representative of the TF relation. Our sample shows an increasing σ_{1D} with both an increasing stellar mass and SFR. However, to properly conduct an investigation of the TF relation, we need to greatly increase the number of disks in our sample (of order hundreds to thousands) to overcome the intrinsic scatter.

The rightmost panels of Figure 4 show that most samples have a specific SFR below the main sequence. This is because we only apply ISM-only extinction to estimate SFR to be consistent with other surveys (see Section 2.4). By applying extra-attenuation, the SFR of IROCKS sources increase by, on average, a factor of 1.8. Assuming galaxies from other surveys also get a factor of ~ 2 increase in SFRs, the center of normalized sSFR is shifted to around 1. After the correction, IROCKS and other high- z samples are near the main sequence within an order of magnitude. Samples in KMOS^{3D} (Wisnioski et al. 2015) and KROSS (Stott et al. 2016) surveys also span a similar range. We discuss the comparison between the IROCKS, KMOS^{3D}, and KROSS kinematics in Section 4.3.

The $z \sim 1$ sample spans line-of-sight velocity dispersions of $48 \lesssim \sigma_{\text{ave}} \lesssim 80 \text{ km s}^{-1}$, velocity shears of $40 \lesssim v_{\text{shear}} \lesssim 192 \text{ km s}^{-1}$, and combined velocity scales of $58 \lesssim S'_{0.5} \lesssim 147 \text{ km s}^{-1}$ (excluding 10633 and 7187W, see Sections 2.3 and 3). We will further discuss kinematic properties, in particular disk settling, using the $v_{\text{shear}}/\sigma_{\text{ave}}$ values in Section 4.3.

Table 5
Kinematics Parameters

ID	σ_{1D}^a (km s ⁻¹)	σ_{ave}^b (km s ⁻¹)	v_{shear}^c (km s ⁻¹)	v_{shear}/σ_{ave}	$S'_{0.5}^d$
11655	100.8 ± 25.5	54.7 ± 3.0 (14.2)	125.9 ± 8.6 (19.6)	2.30 ± 0.20	104.5 ± 5.4
10633	58.4 ± 36.5	54.5 ± 4.0 (11.2)	7.8 ± 5.7 (14.3)	0.14 ± 0.11	54.8 ± 4.0
42042481	86.9 ± 15.6	66.6 ± 1.4 (14.8)	179.4 ± 15.7 (25.7)	2.70 ± 0.24	143.2 ± 9.9
J033249.73	88.0 ± 33.2	71.0 ± 2.9 (15.1)	97.0 ± 14.1 (26.6)	1.37 ± 0.21	98.7 ± 7.2
11169E	140.5 ± 23.0	96.5 ± 3.4 (13.6)	125.5 ± 14.0 (25.9)	1.30 ± 0.15	131.1 ± 7.1
11169W	110.4 ± 13.7	88.0 ± 2.1 (10.1)	57.4 ± 9.8 (20.8)	0.65 ± 0.11	96.9 ± 3.5
7187E	85.9 ± 35.2	80.5 ± 2.5 (12.5)	130.3 ± 12.6 (25.5)	1.62 ± 0.16	122.3 ± 6.9
7187W	190.6 ^e ± 107.5	62.0 ± 3.5 (18.9)	239.8 ± 13.4 (29.9)	3.87 ± 0.31	180.5 ± 9.0
9727	65.6 ± 17.4	64.8 ± 2.5 (14.7)	89.1 ± 11.3 (22.6)	1.37 ± 0.18	90.4 ± 5.9
7615	75.1 ± 24.6	66.1 ± 2.3 (16.6)	89.0 ± 12.7 (25.0)	1.35 ± 0.20	91.3 ± 6.4
11026194	72.1 ± 21.7	64.0 ± 2.9 (15.4)	71.9 ± 9.7 (20.3)	1.12 ± 0.16	81.7 ± 4.8
12008898N	65.1 ± 52.0	61.5 ± 6.8 (14.4)	62.6 ± 12.6 (20.6)	1.02 ± 0.23	75.8 ± 7.5
12008898S	68.2 ± 11.4	61.6 ± 1.2 (8.6)	73.6 ± 7.6 (14.3)	1.19 ± 0.12	80.7 ± 3.6
12019627N	72.8 ± 44.2	55.8 ± 5.0 (12.0)	191.9 ± 14.3 (19.5)	3.44 ± 0.40	146.7 ± 9.6
12019627SE	65.4 ± 23.4	48.0 ± 2.9 (18.1)	71.2 ± 14.6 (23.7)	1.48 ± 0.32	69.5 ± 7.7
12019627SW	51.9 ± 27.3	59.5 ± 4.0 (15.3)	68.3 ± 11.9 (18.0)	1.15 ± 0.21	76.6 ± 6.1
13017973	62.6 ± 19.1	65.3 ± 1.9 (17.8)	117.7 ± 15.6 (27.0)	1.80 ± 0.25	105.8 ± 8.8
13043023	59.5 ± 20.4	63.9 ± 1.9 (15.8)	65.4 ± 9.2 (24.7)	1.02 ± 0.15	78.8 ± 4.1
32040603	49.7 ± 19.4	55.1 ± 1.9 (8.1)	40.5 ± 8.4 (15.7)	0.73 ± 0.15	62.1 ± 3.2
32016379	54.0 ± 18.3	63.3 ± 2.0 (16.8)	64.0 ± 12.7 (23.0)	1.01 ± 0.20	77.8 ± 5.5
32036760	53.1 ± 13.2	55.0 ± 1.9 (11.4)	60.3 ± 12.7 (16.8)	1.10 ± 0.23	69.6 ± 5.7
33009979N	49.7 ± 19.2	49.9 ± 2.3 (11.4)	43.0 ± 8.2 (16.1)	0.86 ± 0.17	58.4 ± 3.6
33009979S	79.8 ± 16.8	61.0 ± 2.1 (13.2)	128.9 ± 15.3 (22.6)	2.11 ± 0.26	109.7 ± 9.1

Notes.

^a Gaussian width of 1D spectrum.

^b S/N-weighted average of dispersion map. The errors in the weighted average are reported. We also report the median errors of the dispersion maps in parentheses. They represent typical error per spaxel.

^c $v_{shear} = 1/2(v_{max} - v_{min})$. The error is the error in v_{shear} . For reference, the median errors of the rotation maps are reported in parentheses to represent typical error per spaxel.

^d $S'_{0.5} = \sqrt{0.5v_{shear}^2 + \sigma_{ave}^2}$. Note that $S'_{0.5}$ is uncorrected for an inclination while $S_{0.5}$ is corrected for an inclination (Kassin et al. 2012).

^e This component has double peak that cannot be separated spatially. See Section 2.3 and the Appendix.

4.2. Disk Fits

Following a disk-fitting analysis by Wright et al. (2009), we fit an inclined disk model to each galaxy's radial velocity map to determine if it is consistent with a disk galaxy. The disk model we use is a tilted ring algorithm for a symmetrically rotating disk (Begeman 1987), which contains seven parameters: the center of rotation in the sky coordinates (x_0 , y_0), P.A. of the major axis (ϕ), inclination angle (i), velocity slope (m_v), radius at which the plateau velocity is achieved in the plane of the disk (R_p), and systemic velocity offset (v_0). The observed radial velocity in the sky coordinates is described by:

$$v(x, y) = v_0 + V_c(R) \sin(i) \cos(\Theta), \quad (3)$$

where R and Θ are the polar coordinates in the plane of the galaxy, and V_c is the azimuthally symmetric circular velocity. Θ is related to the other parameters as follows:

$$\cos(\Theta) = \frac{-(x - x_0) \sin(\phi) + (y - y_0) \cos(\phi)}{R} \quad (4)$$

$$\sin(\Theta) = \frac{-(x - x_0) \cos(\phi) - (y - y_0) \sin(\phi)}{R \cos(i)}. \quad (5)$$

This model defines for a given radius, R , from the center in the plane, the velocity profile is increasing linearly, until it reaches

the plateau velocity, V_p , at a plateau radius, R_p :

$$V_c = \begin{cases} m_v R & \text{if } R < R_p, \\ V_p = m_v R_p & \text{if } R \geq R_p. \end{cases} \quad (6)$$

Since the observed velocity map is a velocity field convolved with a PSF, we also convolve our model with a Gaussian profile whose FWHM is the summation in quadrature of the unsmoothed TT star FWHM and smoothing FWHM used in the science data (Table 1).

Since H α detections only represent the regions of ongoing star formation, which is not necessarily distributed uniformly in the disk, we cannot satisfactorily set a constraint on the inclination angle from the H α morphology alone. The use of deep *HST* images to determine the inclination angle may be more robust, but we do not have *HST* images for all of our sample, and instead we fix the inclination angle to be an expectation value, $\langle i \rangle$, of 57°:3 (e.g., Law et al. 2009) to be consistent throughout our sample. This reduces the number of final fitted parameters to be six. The best-fit model is determined by the least-squares method, weighted by error. Among the 23 components in our 17 IROCKS sources, four (11655, 42042481, 9727, and 33009979S) are well fitted by a disk model. We note that one of the four, 33009979S, has a velocity field that behaves differently near the center of the system compared to the rest of the main body. Our simple model does not fully capture its complex velocity pattern, and

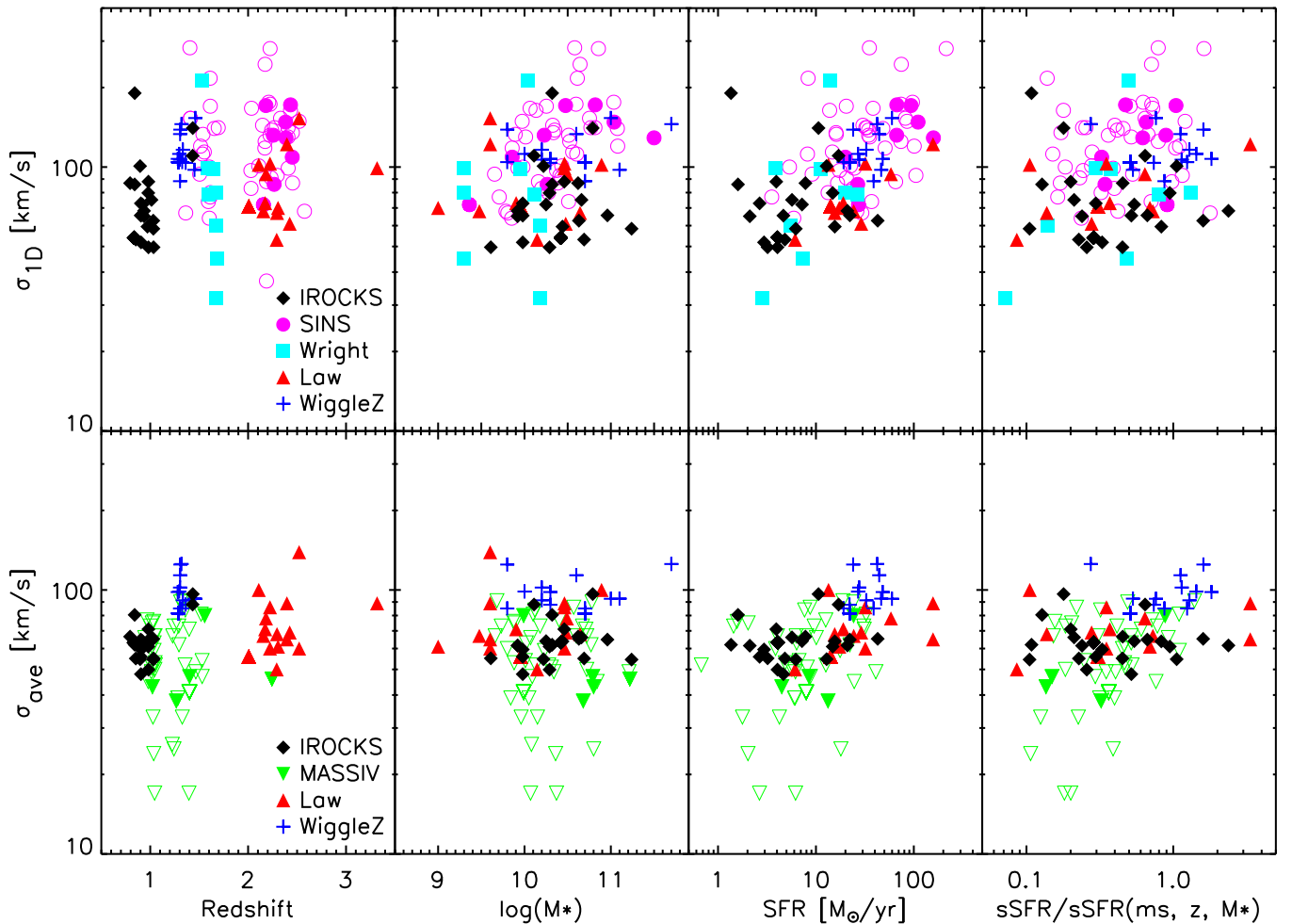


Figure 4. Dispersions σ_{1D} (top) and σ_{ave} (bottom) measured by IROCKS and other IFS studies, SINS (Förster Schreiber et al. 2009), Wright et al. (2009), Law et al. (2009), WiggleZ (Wisnioski et al. 2011) and MASSIV (Epinat et al. 2012; Queyrel et al. 2012) as a function of redshift, stellar mass, SFR, and specific SFR normalized to the Genzel et al. (2015) version of the star formation main sequence of Whitaker et al. (2012) (see Equation (9)). The symbols whose colors and shapes are the same but are open/filled are the difference between non-AO/AO within the same survey. The average error of IROCKS σ_{1D} is 28.2 km s^{-1} , and σ_{ave} is 2.5 km s^{-1} .

our fitting algorithm does not easily converge. To aid with numerical convergence, we enforce the dynamical center to be at the $H\alpha$ flux peak. Additionally, we enforce the plateau radius to be within the detected area for our later analysis in Section 5.3. Given the priors on these values, these constraints yield the lowest converged χ^2 parameter space with the most realistic values for this source. The resultant disk parameters, average residuals, and reduced χ^2 values are listed in Table 6.

In Figure 5, the observed velocity maps, best-fit models, and residuals are shown on the left with the projected major-axis rotation curves on the right. On the rotation curve, the line-of-sight dispersion, σ_{ave} , and σ_{1D} are overplotted. The line-of-sight dispersion of UDS 11655 peaks at the center and flattens at the large radius. This dispersion profile is similarly seen in the majority of the KMOS^{3D}. One possible reason for this dispersion profile is beam smearing (Newman et al. 2013), but our other three disk candidates show essentially flat dispersion profiles. In fact, regardless of their kinematic classification, the majority of our sample show a flat dispersion across the spatial extent of the galaxies (see the rightmost panels in Figure 13). This most likely indicates that our kinematics are not too affected by beam smearing, which may confuse the kinematic classification.

Table 6
Kinematic Model Parameters

ID	P.A. ^a (deg)	R_{peak}^b (kpc)	V_p^c (km s^{-1})	$\langle \Delta \rangle^d$ (km s^{-1})	$\tilde{\chi}^2^e$
11655	125.1	1.2	140.7	13.4	0.1
42042481	152.6	3.2	151.7	23.6	0.4
9727	223.8	0.5	109.9	13.2	0.1
33009979S ^f	249.9	0.5	81.7	30.8	0.7

Notes.

- ^a Position angle.
- ^b Radius where the rotational velocity reaches its peak.
- ^c Plateau velocity, $V_p = m_v R_p$.
- ^d Average residual of |observed – model| kinematics.
- ^e Reduced χ^2 between observed and model velocity field.
- ^f Dynamical center is forced to be the $H\alpha$ peak.

4.3. Disk Settling

Resolved measurements of kinematics allow one to probe the process of disk settling that leads to present-day spiral galaxies. In Figure 6, we compare the IROCKS sample’s σ_{ave} , v_{shear} , and $S'_{0.5}$ values as a function of redshift with those reported by other high- z surveys (Epinat et al. 2009, 2012; Wisnioski et al. 2011).

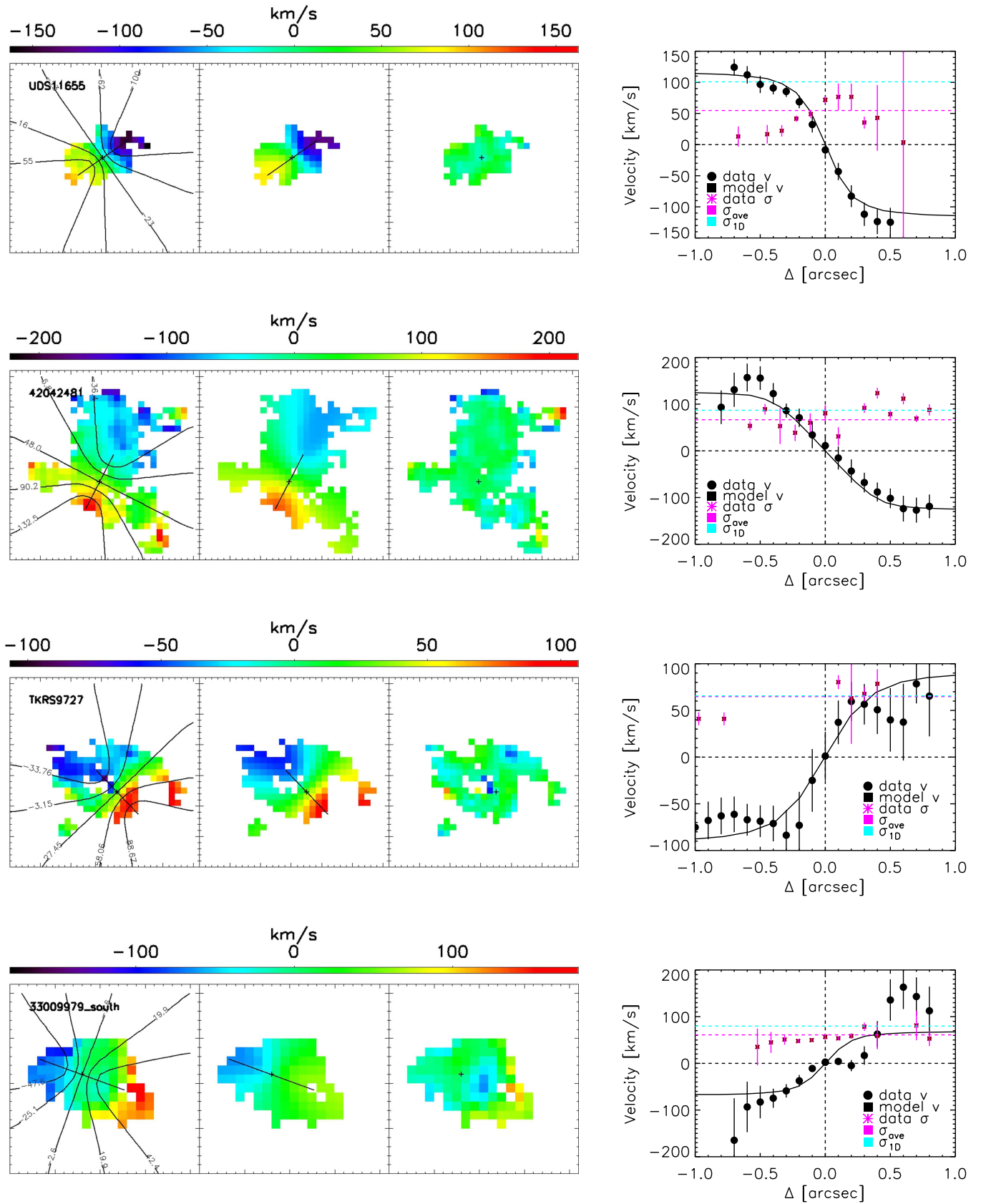


Figure 5. Kinematic inclined-disk best fit to four $z \sim 1$ galaxies in our sample (UDS11655, DEEP2-42042481, TKRS9727, and DEEP2-33009979S). Shown in the left panels are the observed radial velocity (left), fitted inclined disk model (middle), and the residual between observed and model radial velocities (right). The plus sign (+) shows the dynamical center, and the black straight line shows the direction of velocity gradient. The figure on the right shows the observed (black filled circle) and fitted model (black line) rotation curve. The line-of-sight dispersion (magenta asterisks), σ_{ave} (magenta dashed line), and σ_{1D} (cyan dashed line) are overplotted. The velocity field of DEEP2-33009979S near the center behaves differently compared to the rest of the main body. Because our fitting algorithm cannot capture such complicated structure, we enforce the dynamical center to be at the $H\alpha$ flux peak and the plateau radius to be within the detected area.

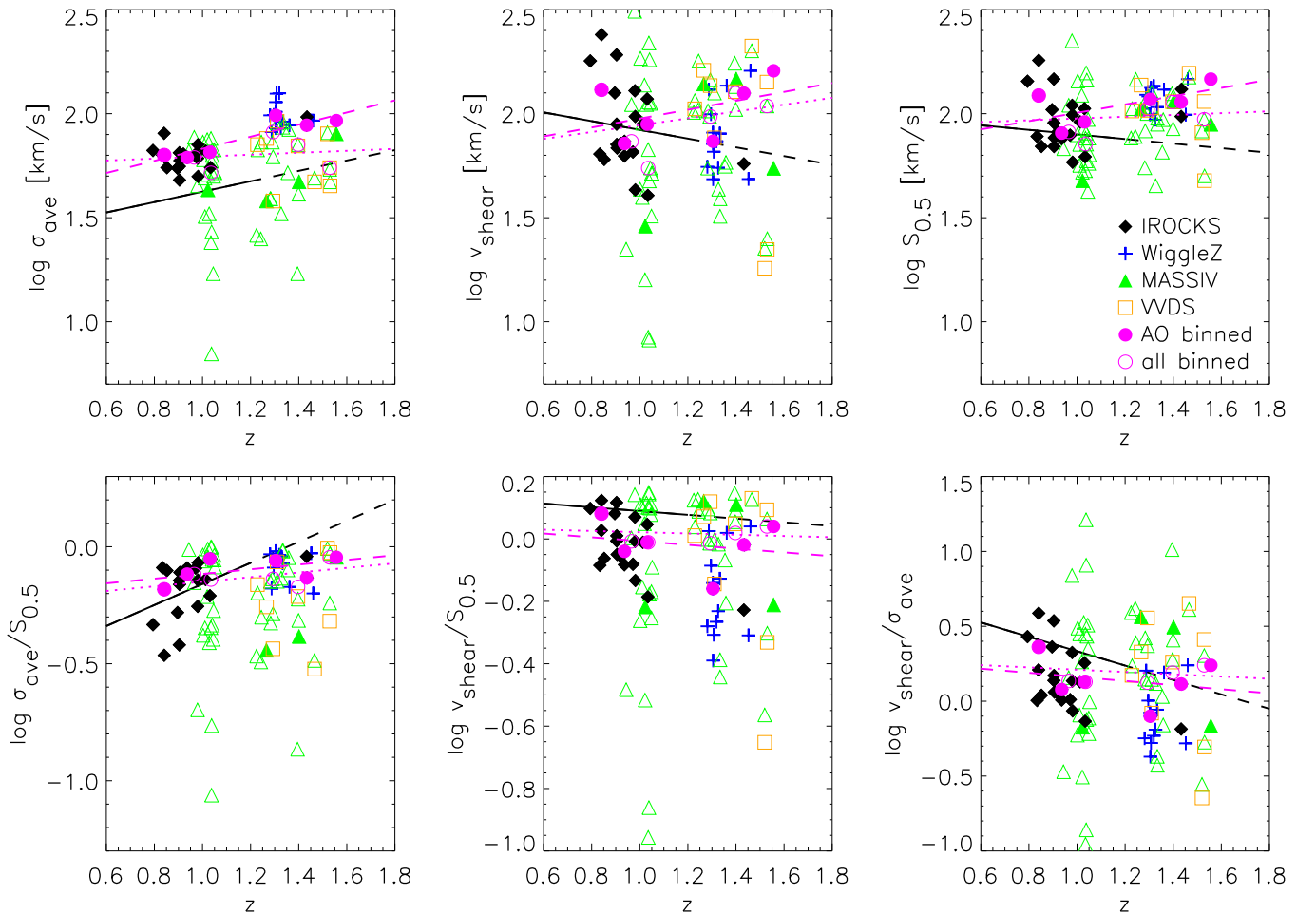


Figure 6. Evolution of σ_{ave} , v_{shear} , $S'_{0.5}$, and their ratios measured by IROCKS and other IFS high-redshift galaxy studies, VVDS (Epinat et al. 2009), WiggleZ (Wisnioski et al. 2011), and MASSIV (Epinat et al. 2012). The symbols whose colors and shapes are the same but are open/filled denote non-AO/AO observations within the same survey. Relationships found by the 1D spectrum study of Kassin et al. (2012) at $0.2 < z < 1.2$ are overplotted as a black line. Black dashed lines are extrapolations of Kassin et al. (2012) beyond $z > 1.2$. Binned medians of all AO data combined are shown as magenta filled circles. Linear fits to the binned AO medians are shown as magenta dashed lines. Binned medians of all data, both AO and non-AO, are shown as magenta open circles, and linear fits are shown as magenta dotted lines.

Note that the v_{shear} values plotted here for Epinat et al. (2009, 2012) are the plateau velocities obtained from their kinematic fitting. For comparison, we removed the inclination correction in their calculated values to be consistent with both our sample and Wisnioski et al. (2011) data points. We also plot the relationship found by the 1D long-slit study of Kassin et al. (2012) at $0.2 < z < 1.2$, for the mass-limited sample ($9.8 < \log M(M_{\odot}) < 10.7$), as black lines for comparison. For a galactic disk to be considered settled, one expects its organized motion in rotation to dominate over random motion, hence $v_{\text{shear}}/\sigma_{\text{ave}} \gg 1$. This quantity as a function of redshift is shown in the lower right panel of Figure 6.

Our measurements deviate from the kinematic relationships found by Kassin et al. (2012): we generally find a higher velocity dispersion, and lower $v_{\text{shear}}/\sigma_{\text{ave}}$ ratio. Most components in the IROCKS sample have $v_{\text{shear}}/\sigma_{\text{ave}} \sim 1$, and only five have $v_{\text{shear}}/\sigma_{\text{ave}} > 2$. If we apply the definition of settled fraction proposed by Kassin et al. (2012) ($v_{\text{shear}}/\sigma_{\text{ave}} > 3$), this fraction in our sample would be 2/21, or $\sim 10\%$, which is lower than the disk fraction expected. Some of this discrepancy may be reconciled by a difference in the v_{shear} definition: Kassin et al. (2012) correct their v_{shear} values for inclinations between $30^{\circ} < i < 70^{\circ}$, using axis ratios of $V + I$ band *HST* images,

while we do not include any inclination dependence in ours. This difference accounts for at most a factor of two increase in v_{shear} values, which may be one of the reasons why our settled fraction appears to be low. Besides inclination effects, our v_{shear} measurements are similar to those of Kassin et al. (2012), implying that the velocities in our sample, both in rotation and dispersion, are higher than their sample.

While v_{shear} measurements may be ambiguous due to the lack of inclination information, the elevated dispersion we measure is robust and consistent with previous IFS+AO studies that observed elevated dispersions compared to local ($z=0$) galaxies. In fact, looking at IFS binned medians for AO-only data (magenta filled circles with linear fit by dashed lines, see upper-left panel in Figure 6) and for all combined data (magenta open circles with linear fit by dotted lines), our combined results show a steady decrease of σ_{ave} with decreasing redshift and increase of $v_{\text{shear}}/\sigma_{\text{ave}}$, consistent with the picture of disk settling, except for the MASSIV survey non-AO data. The median linear fit used on IFS binned data shows a shallower slope, but in general the trend matches that of Kassin et al. (2012), except for v_{shear} and $S'_{0.5}$.

Possible sources of discrepancies in kinematic parameters and their trends between Kassin et al. (2012) and IFS surveys

may due to differing sample selections and definitions of derived values. While Kassin et al. (2012) uses a mass-limited sample ($9.8 < \log M(M_\odot) < 10.7$), we use all available IFS data points in which roughly 20% are outside of this mass range (see the second panels of Figure 4 for a rough estimate). As shown in Kassin et al. (2012), more massive galaxies tend to settle earlier than less massive ones, and mixing different populations in IFS studies may lead to redshift trends being washed out. Furthermore, different definitions of kinematic parameters in IFS surveys may introduce varying systematics. Commonly among IFS studies, σ_{ave} is an average of the velocity dispersion map that is derived from an emission line-width corrected for the instrumental dispersion; however, the definition of v differs among IFS surveys. For instance, v_{shear} in our sample and that of Wisnioski et al. (2011) are derived from the difference between the maximum and minimum in the velocity map, but Epinat et al. (2009, 2012) use plateau velocities obtained from the kinematic model fitting. Also, usually IFS observations are less sensitive to galaxies at large radii than traditional seeing-limited spectrographs, and IFS v_{shear} values may be lower regardless of the calculating methods due to sensitivity differences.

A second method of determining a disk fraction is through disk fitting. Re-enforcing our conclusions from Section 4.2, we found four components well-fitted by an inclined disk model. Indeed, three of these disk candidates have some of the highest $v_{\text{shear}}/\sigma_{\text{ave}}$ (>2) in our sample, while the last one is a nearly face-on disk. Additionally, there are some components, such as DEEP12008898N and 33009979N, that show velocity gradients consistent with rotation by visual inspection, but their small sizes prevent reliable fitting. Overall, it is likely that the common notion that about one-third of the galaxies in high redshift samples are disk-like also applies in our $z \sim 1$ sample, but we need finer sampling and deeper observations to confirm this.

The recent large seeing-limited IFS kinematic surveys KMOS^{3D} (Wisnioski et al. 2015) and KROSS (Stott et al. 2016) have observed 90 and 584 $z \sim 1$ galaxies, respectively. In the KMOS^{3D} survey, the σ_{ave} equivalent dispersion is measured from the outer region of galaxies to avoid rotation and beam smearing effects, and their average dispersion at $z \sim 1$ is found to be 25 km s^{-1} . Their global rotation is corrected for the inclination and is defined as half of the difference between maximum and minimum, which is similar to our v_{shear} . Under these definitions, they find 70% to 93% of galaxies are rotation dominated. In the KROSS survey, the definition of dispersion is similar to our σ^{corr} discussed in Appendix B, where the local velocity gradient is removed from the dispersion, and their sample average is 60 km s^{-1} . The global rotation is the average of velocities in the model velocity map at a radius 2.2 times the effective radius along the semimajor axis that is corrected for inclination. They find 83% of their sample as rotation dominated.

While our definition and sample average of dispersion is consistent with KROSS, the KMOS^{3D} average dispersion definition is different from ours, and their final average value is a factor of two lower. Even if we apply the same method as KMOS^{3D}, the majority of the IROCKS sample has a flat dispersion and the average value would not be as low as their measured value. Also, in both studies, they find significantly higher disk fractions than IROCKS. In general, seeing-limited IFS observations are more sensitive to low surface brightness

regions, and deeper observations by IFS+AO is warranted to fully compare the measurements in the outer regions of galaxies.

5. DERIVED MASSES

In this section, we estimate the gas masses of our galaxies using the measured $\text{H}\alpha$ fluxes. We then derive their virial masses using their kinematics. Finally, for the four galaxies well fitted by disk models, we calculate their dark matter halo and enclosed masses using their fitted disk parameters.

5.1. Gas Mass

The gas mass (M_{gas}) of a galaxy can be expressed with respect to its gas depletion timescale (t_{dep}) as:

$$M_{\text{gas}} = t_{\text{dep}}/\text{SFR}. \quad (7)$$

We can obtain estimates for the gas masses of our galaxies by inferring their t_{dep} from an empirical relationship between t_{dep} and sSFR normalized to the star-formation main sequence (SFMS; Genzel et al. 2015):

$$\begin{aligned} \log(t_{\text{dep}}(z, \text{sSFR}, M_*)|_{\alpha=\alpha_{\text{MW}}}) \\ = \alpha_f + \xi_f \log(1+z) + \xi_g \log(\text{sSFR}/\text{sSFR}(\text{ms}, z, M_*)) \\ + \xi_h (\log(M_*) - 10.5), \end{aligned} \quad (8)$$

where t_{dep} is in the units of $[\text{Gyr}^{-1}]$, M_* is the stellar mass in $[M_\odot]$, and $\{\alpha_f, \xi_f, \xi_g, \xi_h\} = \{+0.1, -0.34, -0.49, +0.01\}$ are fit parameters. $\text{sSFR}(\text{ms}, z, M_*)$ is the sSFR in the SFMS, which follows a fitted function (Whitaker et al. 2012):¹⁰

$$\begin{aligned} \log(\text{sSFR}(\text{ms}, z, M_*)) \\ = -1.12 + 1.14z - 0.19z^2 \\ - (0.3 + 0.13z)(\log M_* - 10.5), \end{aligned} \quad (9)$$

where sSFR is in the units of $[\text{Gyr}^{-1}]$. Combining Equations (7) to (9), we obtain our first gas mass estimates, which we denote $M_{\text{gas},1}$, and they are listed in Table 7.

For comparison, we use an independent method to calculate a second gas mass estimate, which we denote $M_{\text{gas},2}$. The gas surface density (Σ_{gas}) is related to the SFR per area (Σ_{SFR}) by an empirical relation (Kennicutt et al. 2007). Modified for a Chabrier IMF, it is

$$\log\left(\frac{\Sigma_{\text{gas}}}{M_\odot \text{pc}^{-2}}\right) = 0.73 \log\left(\frac{\Sigma_{\text{SFR}}}{M_\odot \text{yr}^{-1} \text{kpc}^{-2}}\right) + 2.91. \quad (10)$$

Replacing SFR by the observed $\text{H}\alpha$ luminosity using Equation (1), the gas mass is:

$$M_{\text{gas},2} = 1.27 \times 10^{-23} L_{\text{H}\alpha}^{0.73} A_{\text{pc}}^{0.27}, \quad (11)$$

where A_{pc} is the area of a pixel in parsec². The values of $M_{\text{gas},2}$ are listed in Table 7. This second method has the additional advantage of allowing us to convert a spatial SFR distribution to a gas distribution using Equation (10). This enables us to investigate local properties of the galaxies, such as their

¹⁰ The coefficients in this equation are different from those in the original equation in Whitaker et al. (2012): $\log(\text{sSFR}(\text{ms}, z, M_*)) = 0.38 + 1.14z - 0.19z^2 - (-0.7 + 0.13z)(\log M_* - 10.5)$. We use Genzel et al.'s (2015) version to follow their method to estimate gas mass.

Table 7
Masses

ID	$\log M_*$ ^a	$\log M_{\text{gas},1}$ ^b	$f_{\text{mol gas}}$ ^c	$\log M_{\text{gas},2}$ ^d	$\log M_{\text{vir}}$ ^e	$\log M_{\text{halo}}$ ^f	$\log M_{\text{enc}}$ ^g
11655	10.22	10.32	0.56	9.82	10.35	11.80	10.49
10633	11.24	10.26	0.09	9.78	9.54
42042481	10.62	10.06	0.22	9.61	10.55	11.95	10.79
J033249.73	10.46	9.72	0.15	9.39	10.62
11169E	10.79	10.28	0.24	9.83	10.78
11169W	10.11	10.45	0.69	9.96	10.56
7187	10.32	9.78	0.22	9.41
7187E	9.22	10.30
7187W	9.17	11.18
9727	10.96	11.04	0.55	10.34	10.22	11.50	10.28
7615	10.66	10.05	0.20	9.63	10.52
11026194	10.25	10.12	0.43	9.68	10.27
12008898N	9.22	9.71
12008898S	9.92	10.49	0.79	9.95	10.19
12019627	9.98	11.36	0.96	9.23
12019627N	9.31	10.43
12019627SE	9.23	10.12
12019627SW	9.34	9.77
13017973	10.63	10.82	0.60	10.19	10.54
13043023	10.44	10.49	0.53	9.95	10.29
32040603	9.61	9.10	0.24	9.40	9.75
32016379	10.42	9.76	0.18	9.51	10.17
32036760	10.69	9.91	0.14	8.93	10.01
33009979N	9.47	9.77
33009979S	10.29	10.39	0.56	9.88	10.15	11.08	10.40

Notes.^a Stellar mass from SED model.^b Total gas mass derived by the method of Genzel et al. (2015).^c Gas mass fraction by the method of Genzel et al. (2015).^d Total gas mass derived by the method of Kennicutt (1998).^e Virial mass estimate, $C = 3.4$ for disk candidates and $C = 5$ for non disks.^f Dark matter halo mass.^g Enclosed (dynamical) mass.

gravitational stability (Section 6.2). This is not possible with the first method, because we only have the global value for M_* .

We note that we have elected to carry out the Genzel et al. (2015) empirical estimate of gas mass for the $z \sim 1$ sample, since our group has verified that OSIRIS H α emission of $z \sim 1.5$ galaxies matches the estimated gas mass directly from Plateau de Bure Interferometer CO 3–2 observations. This gas mass estimate was in better agreement than the standard Kennicutt law used above. We thus show the gas fraction using the first method, $M_{\text{gas},1}/(M_* + M_{\text{gas},1})$, in Table 7.

5.2. Virial Mass

For a virialized system, the virial mass within a given radius, r_{vir} , can be estimated by assuming a symmetric gravitational potential. We use σ_{1D} to represent the kinetic energy of the system, which includes both global rotation and line-of-sight velocity dispersion. Then the virial mass can be written as:

$$M_{\text{vir}} = \frac{C\sigma_{\text{1D}}^2 r_{\text{vir}}}{G}, \quad (12)$$

where G is the gravitational constant, and C is a constant factor that represents the shape of the potential with respect to our viewing angle. For example, $C = 5$ if the mass is uniformly distributed in a sphere, and $C = 3.4$ if it is a uniform thin disk with an average inclination (e.g., Erb et al. 2006b). We use

$C = 3.4$ for our four disk candidate galaxies (UDS11655, 42042481, TKRS9727, and 33009979S), and $C = 5$ for the rest of the sample. Since our galaxies have no clear boundaries (see Section 3), we use the radius of gyration, r_g , as r_{vir} , although it is most likely an underestimate because r_g decreases for more centrally concentrated galaxies.

5.3. Masses for Disk Galaxies

5.3.1. Dark Matter Halo Mass

We assume that for spherical and virialized dark matter halos, the circular velocity is $V_c = [GM(r)/r]^{1/2}$, where $M(r)$ is the total mass enclosed within r . Following common practice, we consider a dark halo within a radius r_{200} , defined as where the mean enclosed density is 200 times the mean cosmic value $\bar{\rho}$:

$$r_{200} = \left[\frac{GM(r_{200})}{100\Omega_m(z)H^2(z)} \right]^{1/3}, \quad (13)$$

where the Hubble parameter H and matter density parameter Ω_m are related to their present values by $H(z) = H_0 E(z)$, $\Omega_m(z) = \Omega_{m,0}(1+z)^3/E^2(z)$, and $E(z) = [\Omega_{\Lambda,0} + (1 - \Omega_{\Lambda,0})(1+z)^2 + \Omega_{m,0}(1+z)^3]^{1/2}$. The halo mass is then written as:

$$M_{\text{halo}} = \frac{0.1V_c^3}{H_0 G \Omega_m^{0.5} (1+z)^{1.5}}. \quad (14)$$

We use the plateau velocity V_p found in Section 4.2 for V_c and report M_{halo} in Table 7.

5.3.2. Enclosed Mass

The enclosed mass, which is often called the dynamical mass, refers to the mass residing in the disk-like component of the galaxy. It is calculated by assuming circular motion in a highly flattened spheroid described by the following equation:

$$M_{\text{enclosed}} = \frac{2V_c^2 r}{\pi G}. \quad (15)$$

Again, we use the plateau velocity, V_p for V_c . For r , we use the farthest distance from the dynamical center to the edge of the galaxy, as seen in the segmentation maps. The resultant enclosed masses are listed in Table 7.

5.4. Mass Summary

In this section, we have estimated the gas masses by two independent methods (Kennicutt et al. 2007; Genzel et al. 2015), and virial masses for our sources. For our four disk candidates, we have also estimated their halo masses and enclosed (dynamical) masses. While the stellar masses in our sample range from $\log M_*/M_\odot = 9.61$ to $\log M_*/M_\odot = 11.24$, the gas masses estimated with the Genzel et al. (2015) method span $9.10 \lesssim \log M_{\text{gas},1}/M_\odot \lesssim 11.36$, and the gas fractions, $f_{\text{mol gas}} = M_{\text{gas}}/(M_{\text{gas}} + M_*)$, span $0.14 \lesssim f_{\text{mol gas}} \lesssim 0.80$.

The virial masses span $9.54 \lesssim \log M_{\text{vir}}/M_\odot \lesssim 10.62$ (excluding 7187W; see Section 2.3), and are overall in order-of-magnitude agreement with M_* and $M_{\text{gas},1}$. However, one particular case, the source 10633, shows notable disagreement in its mass estimates. Specifically, its virial mass, $\log M_{\text{vir}}/M_\odot = 9.54$, is nearly two orders of magnitude lower than the sum of its stellar ($\log M_*/M_\odot = 11.24$) and gas ($\log M_{\text{gas}}/M_\odot = 10.26$) masses. This discrepancy is most likely due to the result of incomplete detection: while the *HST* image shows three separate components, the $\text{H}\alpha$ map only has one component (see Appendix E for details).

For the four disk candidates, we additionally calculated enclosed masses, which are in good agreement with their virial and halo masses, which span $11.08 \lesssim \log M_{\text{halo}}/M_\odot \lesssim 11.95$. In order to obtain a rotation curve with a plateau velocity (V_p), we require the model to fit the plateau radius (R_p) within the detected area (see Section 4.2). The assumption of $V_p = V_c$ may be too simplified to model disks since even in well-ordered (high v/σ) local disks, V_{opt}/V_{200c} (optical-to-virial velocity ratio) is found to differ by 30% to 40% (e.g., Reyes et al. 2012). Taking into account these considerations, M_{enc} and M_{halo} are order-of-magnitude estimates.

Similarly, the assumption in the constant factor C in the virial mass calculation (Equation (12)) has a high uncertainty. We only assume two cases: $C = 3.4$ for the four disk candidates and $C = 5$ for the other galaxies. Between the two, there is a factor of 1.5 difference if we mis-classify galaxies. Moreover, these two cases are assuming uniform thin disks ($C = 3.4$) and uniform spheres ($C = 5$), which are simplifications in themselves. Additionally, as mentioned in Section 5.2, the use of r_g as r_{vir} also adds uncertainty in M_{vir} . Therefore combining these factors, we expect uncertainties of order unity in M_{vir} .

6. CLUMPS

Observations of star-forming galaxies at high redshift show irregular morphologies, dominated by kpc-scale star-forming clumps (e.g., Elmegreen et al. 2009; Förster Schreiber et al. 2009; Livermore et al. 2012). These clumps are likely a result of gravitational instability in the disk. They are speculated to migrate toward the galactic center through dynamical friction and form the galactic bulge (Bournaud 2016, and references therein), and/or be disrupted by stellar feedback and recycle their gas back to the ISM (Hopkins et al. 2012; Oklopčić et al. 2016). In this section, we explain how we define the observed $z \sim 1$ clumps and present their properties.

6.1. Clump Definition

There have been many definitions of “clumps” in the literature. For imaging studies, the definition ranges from visual inspection (e.g., Cowie et al. 1995; Elmegreen et al. 2007), which is difficult to reproduce, to automated definitions based on the intensity contrast between the peak and the local background in galaxy images (Guo et al. 2012; Wuyts et al. 2012). For example, Guo et al. (2015) suggested UV-bright clumps as discrete regions that individually contribute more than 8% of the rest frame UV light of their galaxies. In IFS studies, Genzel et al. (2011) required a clump to be a local maximum in at least two separate velocity channels, while Wisnioski et al. (2012) identified their clumps solely from local $\text{H}\alpha$ peaks in 2D $\text{H}\alpha$ maps.

We define a clump as a local $\text{H}\alpha$ flux peak that is separated by more than two pixels from other peaks in $\text{H}\alpha$ maps (second panel in Figure 13). We apply this definition to the smoothed $\text{H}\alpha$ maps. When this definition is applied to a compact, single-nucleus galaxy, the whole galaxy itself is classified as a “clump” (e.g., UDS 10633). It is technically *not* a clump, but we include these in our analysis for completeness. Under this definition, we identify 68 isolated $\text{H}\alpha$ peaks among 17 sources. We use the 68 isolated $\text{H}\alpha$ peaks to investigate their $\text{H}\alpha$ flux and velocity dispersion, and where we resolve the clumps we are able to measure their physical size.

We measure clump sizes through the following procedure: (1) we make an azimuthally averaged surface brightness profile centered at the peak, (2) compute the derivative of the surface brightness profile with respect to radius, (3) set the background to be the radius (r_{back}) at which the derivative crosses 0 or reaches less than a cut-off value (in our case $3^{-18} \text{ erg s}^{-1} \text{ cm}^{-2} \text{ arcsec}^{-1}$), (4) subtract the background from the $\text{H}\alpha$ map, and (5) calculate the radius at which half of the total flux within r_{back} is included. The size obtained by this method is denoted as r_{ap} . This method is robust when the surface brightness profile is steep. When the profile is shallow (i.e., size is large), the derivative slowly plateaus to 0, and our choice of the cut-off value is not necessarily the best; however, a shallow profile also means the background value is not sensitive to the choice of the background location, so we do not expect this uncertainty to have a significant effect on our measurements.

When the surface brightness profile is approximated by a Gaussian function, using its standard deviation (σ_G), the half-light radius ($r_{1/2}^G$) and FWHM can be written as $r_{1/2}^G = \sqrt{-2 \ln 0.5} \sigma_G$ and $\text{FWHM} = 2\sqrt{2 \ln 2} \sigma_G$, respectively. Using these relationships, the final clump sizes, denoted as $r_{1/2}$,

are expressed as follows:

$$r_{1/2} = \sqrt{r_{\text{ap}}^2 + \frac{2 \ln 0.5}{4 \times 2 \ln 2} \text{FWHM}^2}. \quad (16)$$

The final values of r_{ap} and $r_{1/2}$ are listed in Table 8. Some clumps are smaller than the beam sizes, and are considered unresolved. Among 68 isolated peaks, 58 are resolved clumps. The uncorrected sizes (r_{ap}) of identified clumps are shown in Figure 7 as the size of dashed circles centered at the peaks. Figures are ordered from the highest to the lowest stellar mass estimated by SED fitting (Section 2.4).

The total H α flux for each clump is measured by summing up the spectra inside the uncorrected aperture radius (r_{ap}), and fitting a Gaussian profile to the H α emission line in a total spectrum. To compare with other surveys, we assume a spatially uniform, ISM-only extinction to convert H α fluxes into SFRs (see Section 2.4 for H II and ISM extinction). We also obtain each clump's σ_{ID} , measured from the width of the Gaussian function, and corrected for an average instrumental width within the aperture radius. The values of SFR and σ_{ID} are listed in Table 8. When the clump is unresolved, its SFR and dispersion values are still valid within the aperture, and we include them in our analysis. The clumps are marked as A, B, and so forth in descending order of brightness in Figure 7.

We find that among the $z \sim 1$ sample, star-forming clumps have a half-light radius between 0.17 and 4.5 kpc, σ_{ID} between 13 and 160 km s $^{-1}$, and SFR between 0.1 and 27 M_{\odot} yr $^{-1}$.

6.2. Disk Stability

We investigate the dynamical stability of the candidate disks using H α flux maps and fitted disk models. The Toomre parameter, Q_{gas} , describes the gravitational stability of a gaseous disk by using the local velocity shear and random motion and is expressed as:

$$Q_{\text{gas}} = \frac{\sigma \kappa}{\pi G \Sigma_{\text{gas}}}, \quad (17)$$

where σ is the local velocity dispersion, G is the gravitational constant, Σ_{gas} is the gas surface density (evaluated from Equation (11)), and κ is the epicyclic frequency of the disk. κ can be replaced by the orbital frequency, Ω , if the system is Keplerian. $Q_{\text{gas}} \lesssim 1$ to 2 can cause instability-driven large scale turbulence. Following Thompson et al. (2005) and Genzel et al. (2011), if we assume the total mass $M_T \propto v^2 r / G$ and total gas mass M_g inside the radius r , then the Toomre parameter can be written as follows:

$$Q = a \frac{\sigma}{v} \left(\frac{M_T}{M_g} \right) = \frac{\sigma a}{v f_g}, \quad (18)$$

where f_g is the gas fraction within radius r , and the constant a represents different potentials. We apply $a = \sqrt{2}$ for a flat rotation curve for a disk. In our sample, four galaxies (11655, 42042481, 9727, and 33009979S) are well fit to a disk model, and Q_{gas} can be computed spatially using the locally measured gas surface density, velocity dispersion, and modeled rotation. The inclinations of these galaxies are not well constrained with H α detection, and hence we use the expectation value $\langle i \rangle = 57^\circ 3$ for all four disk fittings (Section 4.2), and

Table 8
Clump Parameters

ID	Clump	$r_{1/2}^a$ (kpc)	r_{ap}^b (kpc)	SFR ^c (M_{\odot} yr $^{-1}$)	σ_{ID}^d (km s $^{-1}$)	
11655	A	2.50	2.63	8.43	48.0	
	B	0.58	0.99	0.56	67.8	
10633	A	0.91	1.23	7.51	57.3	
42042481	A	3.04	3.13	2.40	61.0	
	B	0.79	1.10	0.21	43.6	
	C	0.85	1.15	0.19	51.2	
	D	0.63	1.00	0.16	50.1	
	E	0.61	0.98	0.12	32.6	
	F	...	0.66	0.10	131.8	
J033249.73	G	...	0.70	0.06	79.3	
	A	1.25	1.75	0.84	77.2	
	B	0.98	1.57	0.78	61.8	
	C	...	1.22	0.31	60.4	
11169	D	...	0.76	0.19	93.4	
	A	2.47	2.62	14.12	96.8	
	B	3.02	3.14	9.49	113.9	
	C	0.42	0.96	0.94	66.6	
	D	0.65	1.08	0.88	64.4	
7187	E	0.19	0.89	0.71	70.8	
	A	3.01	3.17	1.88	87.7	
	B	1.52	1.81	0.50	99.5	
	C	...	0.93	0.17	71.7	
	D	0.45	1.08	0.17	56.6	
9727	E	0.33	1.03	0.14	24.5	
	F	0.53	1.11	0.11	73.5	
	A	4.45	4.56	26.74	89.7	
	B	1.14	1.52	3.37	86.6	
	C	0.51	1.13	1.69	45.4	
	D	0.80	1.28	0.99	13.3	
	E	0.42	1.09	0.78	40.6	
	F	...	0.82	0.66	45.9	
	7615	A	2.22	2.45	1.77	79.4
		B	1.28	1.64	1.17	79.6
C		1.63	1.93	1.15	60.6	
D		1.89	2.16	0.94	64.3	
E		1.13	1.53	0.60	70.8	
11026194	F	0.69	1.24	0.44	59.8	
	A	2.63	2.82	4.56	65.0	
	B	1.20	1.56	2.25	76.4	
	12008898	A	2.84	2.91	13.87	61.4
		B	2.74	2.81	11.92	59.6
	12019627	C	1.35	1.48	2.07	54.0
A		1.82	1.99	1.93	45.6	
B		2.34	2.47	1.66	42.6	
C		1.10	1.36	0.92	58.5	
D		0.82	1.15	0.58	71.1	
E		0.46	0.92	0.39	54.4	
13017973	F	0.73	1.08	0.34	25.3	
	A	2.77	2.96	13.12	36.2	
	B	1.88	2.14	12.03	161.5	
	C	1.69	1.98	4.83	39.6	
	D	1.37	1.71	4.17	60.4	
	E	0.82	1.32	3.75	62.0	
	F	...	0.69	1.31	117.6	
	G	...	0.90	1.23	76.6	
13043023	H	...	1.03	0.99	46.6	
	A	1.08	1.49	2.31	104.5	
	B	0.52	1.15	1.39	69.3	
	C	0.51	1.14	0.96	61.1	
32040603	D	...	0.69	0.66	58.6	
	A	1.53	1.85	1.75	52.5	
	32016379	A	1.94	2.09	1.20	64.9
B		1.48	1.68	0.63	27.2	

Table 8
(Continued)

ID	Clump	$r_{1/2}^a$ (kpc)	r_{ap}^b (kpc)	SFR ^c ($M_{\odot} \text{ yr}^{-1}$)	σ_{1D}^d (km s^{-1})
	C	0.72	1.06	0.26	58.6
32036760	A	2.78	2.95	2.60	55.1
33009979	A	2.15	2.30	7.45	60.8
	B	1.92	2.09	2.43	42.8
	C	0.74	1.10	0.61	56.5

Notes.

^a Half-light radius of clump.

^b Aperture size (i.e., non corrected size).

^c ISM-corrected SFR inside the half-light radius.

^d Integrated velocity dispersion inside the half-light radius.

therefore this adds uncertainties into the derived Toomre values.

Our model assumes rotation-supported disks with $v = v_{\text{circ}}$. This may not be appropriate for disks that are partially supported by turbulence, and in those cases, their potential would likely be better traced by $S'_{0.5}$ (or $S_{0.5}$) instead of v_{circ} . Also, we use $a = \sqrt{2}$ for a flat rotation curve, while inner part of the disk's rotation may better resemble solid body rotation, which would give $a = 2$. Despite these shortcomings in our model, we retain these assumptions for a one-to-one comparison with other IFS studies.

Instead of showing absolute values, we show relative Toomre maps in Figure 8 (Wisnioski et al. 2012) for our four disk candidates (from the left, 11655, 42042481, 9727, and 33009979S). We overplot circles with centers located at the peaks and radii representing the aperture radius (r_{ap}) of the clumps. Most clumps reside where Q_{gas} is low (unstable), as seen in higher-redshift observations (Genzel et al. 2011; Wisnioski et al. 2012).

6.3. Clump Evolution

The empirical properties of star-forming clumps can provide clues to the physical mechanisms that drive their formation and evolution, and it is interesting to compare them to local H II regions. Wisnioski et al. (2012) compared their observations on $z \sim 1.3$ star-forming clumps with data on local H II regions and found tight scaling relations between the clump size, luminosity, and velocity dispersion regardless of clump redshifts. This led them to conclude that clumps at $z \sim 1.3$ are likely larger analogs of local H II regions, and turbulence sets the scaling relation. On the other hand, Livermore et al. (2015) using observations on gravitationally lensed galaxies, combined with previous lensed and non-lensed galaxies, found that the mean surface brightness and characteristic luminosity of clumps evolves with redshift, becoming brighter as redshift increases. They argued that this can be explained by an evolving gas mass fraction that increases with redshift, which translates to a higher SFR density if the clumps are results of disk fragmentation via gravitational instability. These two results imply two distinct mechanisms that set the characteristics of star-forming clumps. We will compare our IROCKS measurements with these results, and attempt to reconcile the differences.

Figure 9 shows the clump SFR surface density, Σ_{SFR} , as a function of redshift, of IROCKS and data points from other

surveys (Genzel et al. 2011; Wisnioski et al. 2012; Livermore et al. 2015). Also shown in the figure is Equation (5) of Livermore et al. (2015), the empirical relation they found. We find excellent agreement with their relation, which we consider to be part of the supporting evidence for the disk fragmentation scenario. Figure 10 shows the relations between our clump size, luminosity, velocity dispersion, and Σ_{SFR} , together with data points from the same surveys as Figure 9. Wisnioski et al. (2012) found that assuming equal weighting for all points, combining local H II regions and $z > 1$ clumps, luminosity scales with size by the relation, $L \propto r^{2.72 \pm 0.04}$. When only $z > 1$ clumps are considered (eight clumps), this relation becomes $L \propto r^{1.42 \pm 0.45}$. Using IROCKS-resolved clumps (58 clumps), we find $L \propto r_{1/2}^{1.47 \pm 0.15}$, and this is consistent with Wisnioski et al. (2012). In fact, like Wisnioski et al. (2012), we find our relation can be reasonably extended to H II regions at $z \sim 0$. However, as already shown by Figure 9, this does not imply a lack of time evolution in clump properties. Interestingly, we find that even though we have similar velocity dispersions as the other IFS studies, the SFR surface density is lower in our sample. Clumps with a given velocity dispersion are able to occupy a range of SFR surface density conditions. This probably indicates that clumps are not necessarily virialized, and gravitational instability contributes to the high dispersion observed (Livermore et al. 2015).

The $z \sim 1$ clumps agree well with the slightly higher redshift IFS samples from Wisnioski et al. (2012) on the σ - r , L - r , and L - σ relations, but have some deviation on the Σ - σ relation. On Σ - z relation, the $z \sim 1$ clumps agree well with the IFS lensed galaxy samples from Livermore et al. (2015). Our clump SFR surface density measurements support the hypothesis of clumps forming from disk fragmentation. We find similarities between local H II regions and high- z star-forming clumps. Yet a larger statistical sample is still needed to explore redshift, stellar mass, and gas fraction trends that could point to some environmental impact on clump properties. Also, a better understanding between observational and analysis differences between IFS lensed and un-lensed population is still warranted.

7. CONCLUSION

In this paper, we have presented the first results of the IROCKS survey, which is currently the largest sample of IFS +AO observations of star-forming galaxies at $z \sim 1$. The sample consists of sixteen $z \sim 1$ and one $z \sim 1.4$ star-forming galaxies, selected from the four well studied fields, GOODS-North, GOODS-South, DEEP2, and UDS. All of our targets but one were observed with the upgraded OSIRIS grating at the Keck I telescope, with the assistance of a newly upgraded AO system. We focused on the kinematics and morphological properties of star-forming galaxies at $z \sim 1$ by using H α emission line as a star formation tracer. The results of our survey are summarized as follows:

- (1) In our sample of sixteen star-forming galaxies with $0.794 \leq z \leq 1.03$ (median $z = 0.936$), twelve are classified as single and four as multiple systems, based on the number of spectrally and/or spatially separated components observed. Our seventeenth source 11169 has $z = 1.43$, and is classified as a multiple system.
- (2) We computed the SFR for each galaxy. Taking into account only extinction by the ISM ($\text{SFR}_{\text{H}\alpha}^0$) spans $0.2 \leq \text{SFR}_{\text{H}\alpha}^0 \leq 42.7 M_{\odot} \text{ yr}^{-1}$. Applying extra attenuation

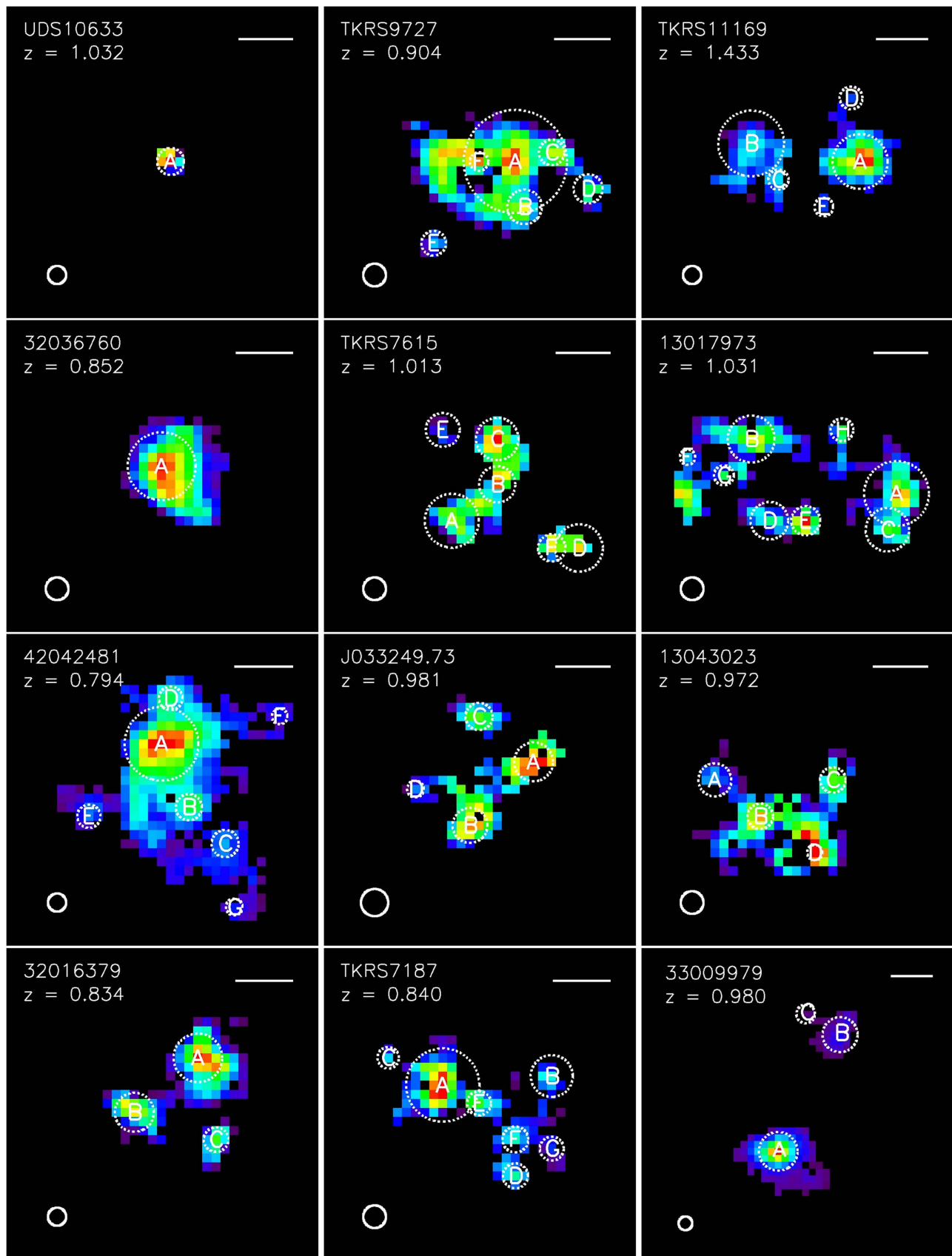


Figure 7. Identified clump locations and sizes. The radii of dashed circles are the size used to obtain the total clump $H\alpha$ flux (r_{ap}). In our definition, a clump is a local $H\alpha$ peak that is separated by more than two pixels from neighbor peaks in $H\alpha$ maps (second panels in Figure 13). The clumps are marked as A, B, and so forth in descending order of brightness. Panels are organized from the highest to lowest stellar mass estimated by SED fitting. The name and redshift of the galaxy are listed at the top left corner. The length of the top right line presents 5 kpc at that redshift. The solid circle at the bottom left presents the size of smoothing FWHM.

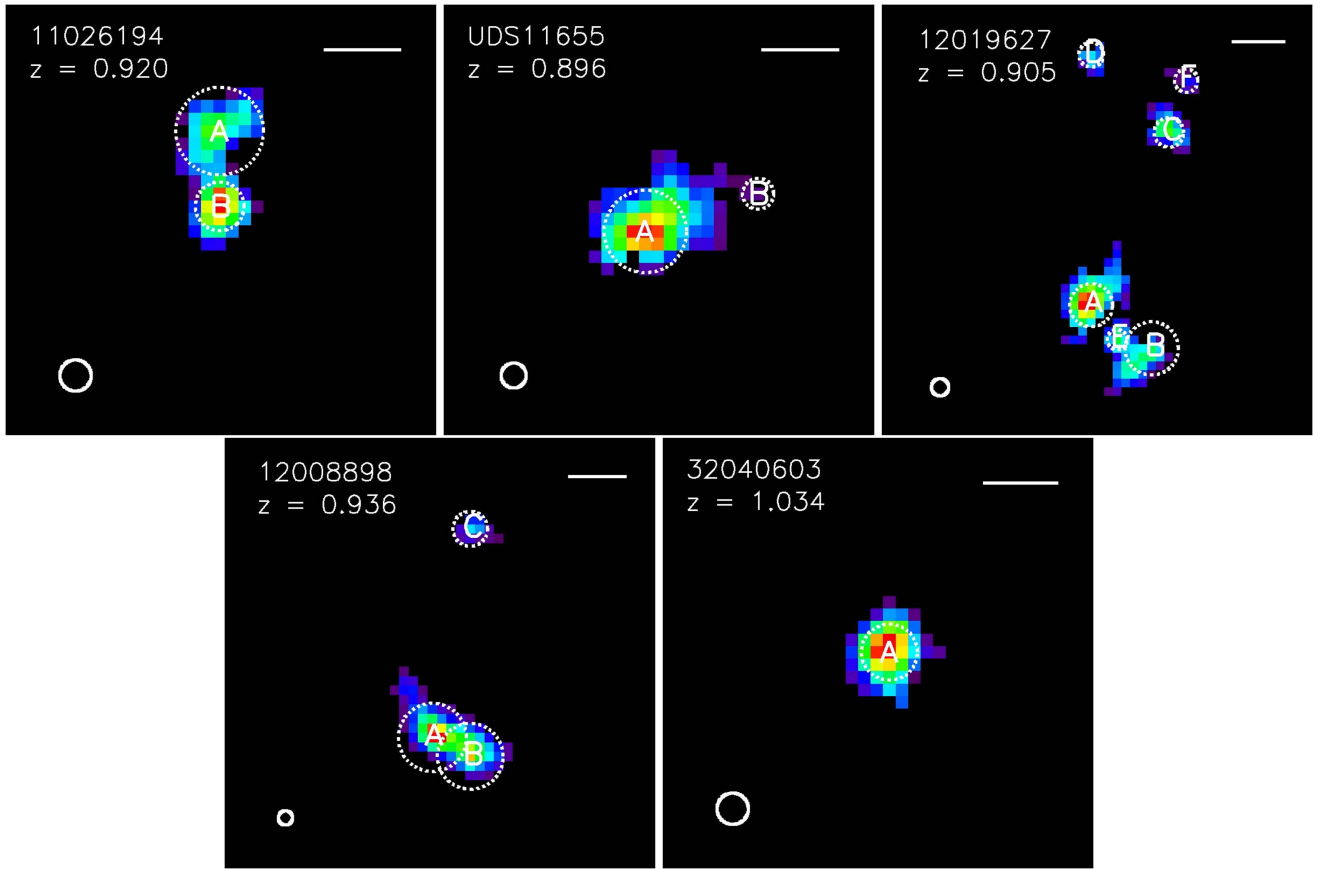


Figure 7. (Continued.)

from H II regions, it increases by a factor of ~ 2 to 5 and becomes $0.3 \leq \text{SFR}_{\text{H}\alpha}^{00} \leq 108.4 M_{\odot} \text{yr}^{-1}$. We find that applying both ISM and H II extinction provides better agreement with the SFR estimated from SED fitting.

- (3) Using line width measurements, we find all $z \sim 1$ components to have line-of-sight velocity dispersions of $\sigma_{\text{ave}} \gtrsim 48 \text{ km s}^{-1}$, with a median value of 61.6 km s^{-1} . In comparison, both components in 11169 ($z \sim 1.4$) have even higher dispersion, $\sigma_{\text{ave}} \sim 90 \text{ km s}^{-1}$. Considering disk fraction using both disk model fitting and $v_{\text{shear}}/\sigma_{\text{ave}}$ criteria, $z \sim 1$ galaxies resemble $z > 1$ galaxies in that about one-third are disk-like.
- (4) The stellar mass of each galaxy is estimated using SED fitting, and it ranges between $9.6 \leq \log M_{*}/M_{\odot} \leq 11.2$. Gas mass and virial mass are given through SFR and kinematics arguments, and they are between $9.10 \lesssim \log M_{\text{gas},1}/M_{\odot} \lesssim 11.04$ and $9.54 \lesssim \log M_{\text{vir}} \lesssim 10.62$, respectively. Using both stellar and gas mass, we find the gas fraction in these galaxies ranges between $0.14 < f_{\text{gas}} < 0.80$.
- (5) Clump properties in the $z \sim 1$ galaxies were explored for the first time by IFS, and we identified 68 star-forming clumps, among which 58 are resolved. The sizes of resolved clumps are $0.3 \lesssim r_{1/2} \lesssim 4.5 \text{ kpc}$, their SFRs are $0.1 \lesssim \text{SFR} \lesssim 26.7 M_{\odot} \text{yr}^{-1}$, and integrated dispersions are $13 \lesssim \sigma_{\text{ID}} \lesssim 132 \text{ km s}^{-1}$.
- (6) Compared to the other high- z clump sample, they support the disk fragmentation model as the clump formation mechanism while the $z \sim 1$ clumps follow a similar size–

luminosity clump relation as local H II regions even though they are orders of magnitude larger in SFR and size.

The high spatial resolution that IFS+AO provides comes with a sacrifice of S/N that impacts our measurements of galaxy rotation. Compared to observations without AO, ours are less sensitive to low surface brightness regions of the galaxies, which is where the plateau velocity should be measured. Consequently, our rotation measurements are biased toward the more dispersed, central portions of the galaxies, and should not be used as a direct comparison to 1D slit-based spectroscopy observations that probe the fainter outskirts of galaxies. Indeed, IFS+AO observations find more dispersion-dominated galaxies while non-AO find more rotationally-dominated systems because of this effect (Newman et al. 2012).

In order to boost S/N in the low surface brightness regions of the galaxies, where plateau velocities are reached, we apply a smoothing to each galaxy data cube. This smoothing does not have a significant impact on the global dispersions (Appendix B) and dispersion profiles (Section 4.2). However, it may soften the velocity gradient, resulting in a lower estimate underestimate of v_{shear} (Appendix B).

High-redshift kinematic studies systematically classify their kinematic types by using disk model fitting and the global v/σ parameter. However, interacting pairs and late-stage merger remnants have shown that they can sometimes produce similar kinematic fields to high-redshift disk systems. The use of both kinematic and morphological analysis is suggested to help distinguish between late-stage mergers and rotating disks

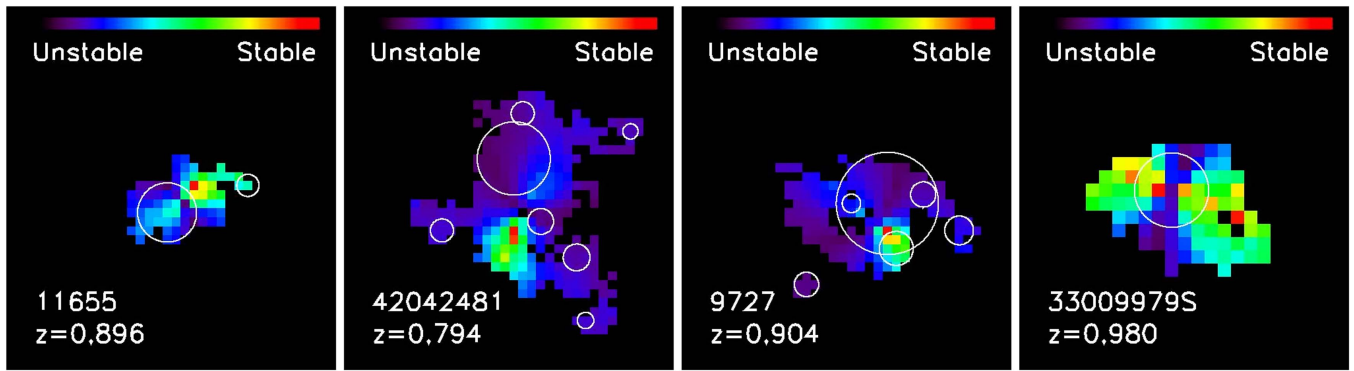


Figure 8. Relative Toomre parameter (Q , Equation (18)) maps of four disk candidates (UDS11655, DEEP2-42042481, TKRS9727, and DEEP2-33009979S) in IROCKS sample. Circles are centered at the peaks of the clumps, and their radii represent their sizes, r_{ap} . Most clumps are located where Q is low (unstable), which is seen by high- z observations (Genzel et al. 2011; Wisnioski et al. 2012).

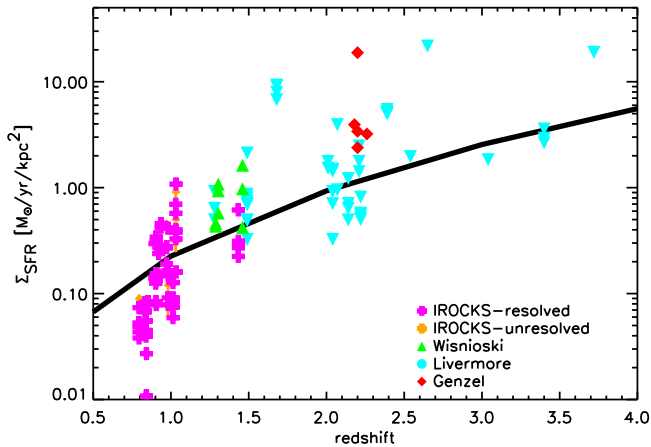


Figure 9. Star formation rate surface density of clumps as a function of redshift. IROCKS and previous survey (Genzel et al. 2011; Wisnioski et al. 2012; Livermore et al. 2015) measurements are plotted with an empirical fit by Livermore et al. (2015). IROCKS data points are separated between resolved (magenta) and unresolved (orange) (see Section 6).

(Hung et al. 2015). It is also important to note that when comparing kinematic properties (such as the disk or merger fraction), we need to use more uniform kinematic distinction criteria between different spectroscopy studies. This has been challenging since each group has been re-defining their kinematic distinction criteria, and their disk modeling procedures vary. The community should be careful when combining data sets, and we need to push more for unified data samples and analysis techniques, especially between differing instruments.

In the last few years, more physically realistic high-resolution simulations have become available, and galaxy formation and evolution are now studied at individual galaxy structure size scales (\sim kpc). Comparing our kinematic results against zoomed-in hydrodynamics simulation data points of Kassin et al. (2014), our results fall between the cold (without stellar feedback) and warm (with feedback) models, suggesting at least a moderate amount of feedback is needed to reproduce our results (see Figure 1 of Kassin et al. 2014). However, Kassin et al. (2014) have commented on their results’ possible dependences on poorly constrained quantities such as the average stellar mass of galaxies and the spatial variations of gas density and temperature. Simulations which probe parameters such as stellar mass, feedback mechanism, and metallicity

would certainly be helpful for pinpointing the physics that dictate “feedback” in galaxy evolution.

Our $z \sim 1$ clumps are consistent with the SFR surface density and redshift relation found by Livermore et al. (2015), who argued that their relation suggests gravitational instability as the clump formation mechanism. We can further test this theory by measuring the gas fractions of individual clumps using, for example, molecular line emissions from ALMA, and comparing them to their luminosities. The luminosity of a clump is related to its mass which, if formed from gravitational instability, is higher for larger gas fractions.

In this study, we extended the IFS study of high- z kinematics and morphologies to the $z \sim 1$ regime with sixteen additional sources. However the number of IFS high- z samples are still limited and currently only able to probe the most massive and luminous star-forming galaxies. Extremely large telescopes coming in a few years combined with IFS+AO will enable us to see high- z galaxies at the scale of a giant molecular cloud, and will provide us with key information to understand galaxy evolution.

This is the first paper from the IROCKS study, and a second paper on the nebular diagnostic of these galaxies is forthcoming, where we will focus on resolved metallicity gradients on ten galaxies and explore ionization and feedback mechanisms like shocks and AGNs.

The Dunlap Institute is funded through an endowment established by the David Dunlap family and the University of Toronto. This research was partly supported by the Natural Sciences and Engineering Research Council (NSERC) of Canada Discovery Grant. We extend our gratitude to Nick Mostek, Alison Coil, and Bahram Mobasher for generously sharing their SED parameters for these sources. We also thank Emily Wisnioski for providing local H II measurements used in our clump analysis. We are grateful to the Keck Observatory staff, Jim Lyke and Randy Campbell, for helping with many of the observations and the OSIRIS data reduction pipeline. We thank the referee for a thorough reading and valuable comments. The data presented herein were obtained at the WM Keck Observatory, which is operated as a scientific partnership among the California Institute of Technology, the University of California, and the National Aeronautics and Space Administration. The Observatory was made possible by the generous financial support of the WM Keck Foundation. The authors wish to recognize and acknowledge the very significant cultural role and reverence that the summit of

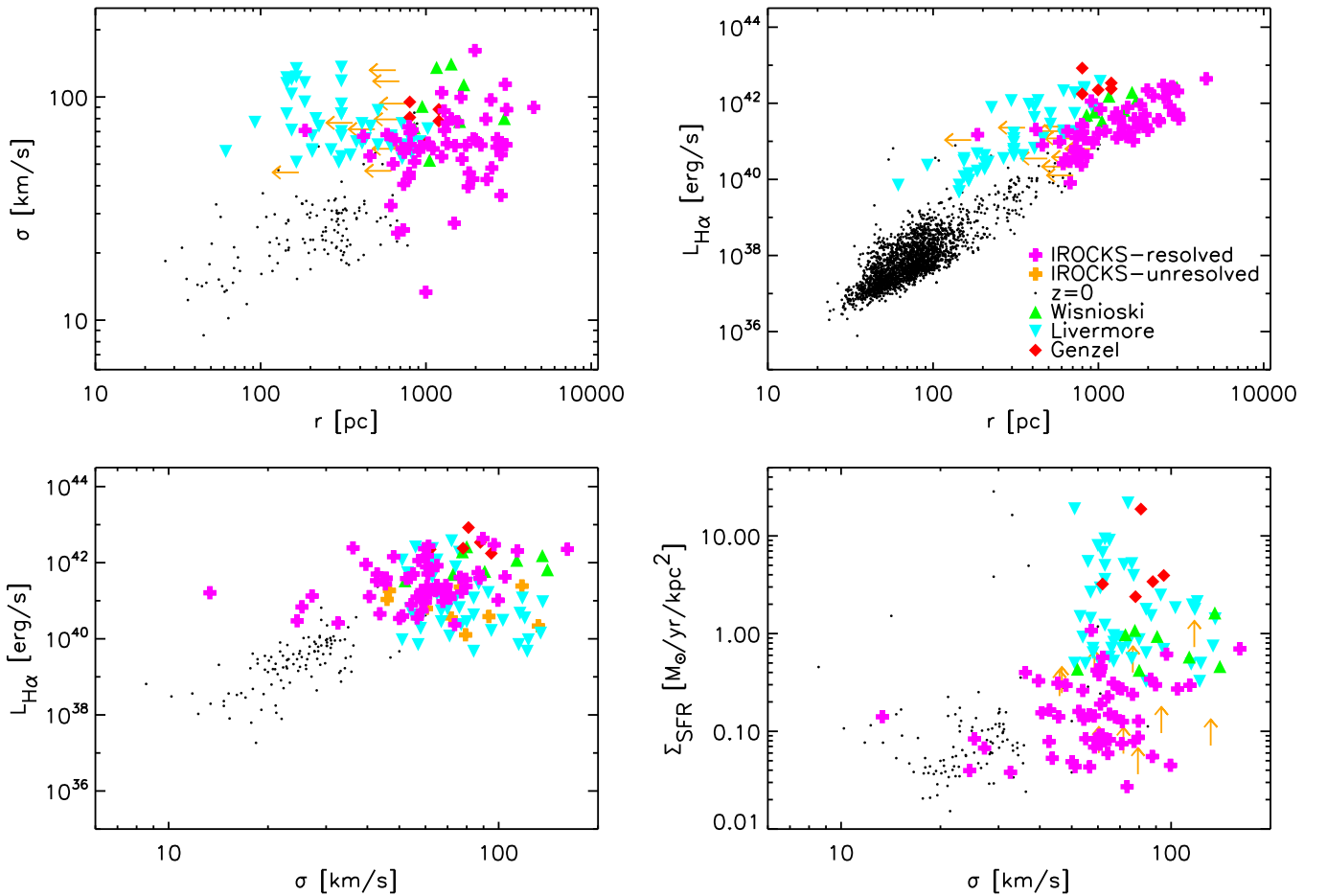


Figure 10. Clump size, velocity dispersion, luminosity, and SFR surface density relations. IROCKS and previous surveys (Genzel et al. 2011; Wisnioski et al. 2012; Livermore et al. 2015) are shown. $z = 0$ data points are described in Wisnioski et al. (2012). IROCKS data points are separated between resolved (magenta) and unresolved (orange) clumps or regions. For the two top panels, where the x -axis is in units of radii [pc], unresolved points are shown as left-pointing arrows to emphasize these size measurements are upper limits. On the bottom right panel, the SFR densities for unresolved clumps are shown as up-pointing arrows as they are the lower limits.

Mauna Kea has always had within the indigenous Hawaiian community. We are most fortunate to have the opportunity to conduct observations from this mountain.

APPENDIX A ADAPTIVE SMOOTHING

In IFS studies of high-redshift galaxies, very often data cubes are spatially smoothed by a Gaussian function of FWHM ~ 2 pixels to increase the S/N (e.g., Förster Schreiber et al. 2009; Law et al. 2009; Wright et al. 2009; Genzel et al. 2011; Wisnioski et al. 2011; Epinat et al. 2012). Some properties (e.g., σ_{ID} , σ_{ave} , and SFR) are not significantly affected by smoothing, but other parameters need careful treatment. For example, when we study the spatially resolved quantities, such as the metallicity gradient across the galaxy and resolved clumps, the smoothing process distributes the flux to neighbor pixels and as a result smears out the information. In particular, observations with AO, where diffraction-limited observation is potentially achievable, lowering the spatial resolution in the data reduction process is detrimental. In order to increase S/N while preserving as high spatial resolution as possible, the choice of optimum width is crucial. We develop an adaptive smoothing code to find the best choice of smoothing width.

In short, the code iteratively applies smoothing of increasing FWHM to a data cube until spaxels reach a desired or optimal S/N. In each iteration, the entire reduced, un-smoothed cube is smoothed by a single FWHM, and the S/N of each spaxel in an $H\alpha$ flux map is calculated using the method described in Section 2.3. For the next iteration, the same original, reduced, un-smoothed cube is then smoothed by a wider FWHM, usually increasing by 0.5 pixel for each iteration, and we repeat the process until the maximum FWHM is reached, or most spaxels achieve a high S/N. The smallest smoothing FWHM that allows the spaxel at $[i, j]$ to reach the desired S/N is then recorded as $\text{FWHM}_{i,j}$. The most optimized, final smoothing width for the particular data cube is the mean $\text{FWHM}_{i,j}$ within the region of interest. Figure 11 shows a $\text{FWHM}_{i,j}$ map of UDS11655 as an example. The color presents the value of FWHM, and is illustrative how adaptive smoothing can potentially be powerful at increasing the S/N of low surface brightness emission.

In the analysis, we use this code only to find the most optimized smoothing width. However, this code has the potential to produce an adaptively smoothed data cube, where spaxels of a higher signal would be smoothed by a narrower FWHM. Such a method is suitable for morphology related

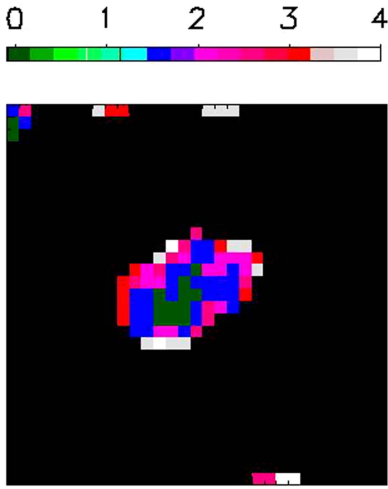


Figure 11. FWHM map of UDS11655. The color presents the smallest value of FWHM that makes the particular spaxel reach a desired S/N. The final single smoothing width for each data cube is the mean of FWHM map. For UDS11655, FWHM = 2.0 pixel is chosen as a final FWHM.

analysis (e.g., morphology parameter, size, peak location), and particularly beneficial when (1) the galaxy contains an AGN with a high single $[\text{N II}]/\text{H}\alpha$ peak, which would allow for a more accurate measurement of the location of the AGN; also, when (2) multiple star-forming clumps are located close to each other, which would prevent excess smoothing to smear the boundaries between them. On the other hand, a spatial varying smoothing length makes it difficult to model the beam size correctly. The potential of this method and its numerous merits will be explored in future studies.

APPENDIX B EFFECT OF SMOOTHING ON KINEMATICS

Side-by-side comparisons of the AO and AO+artificial smoothing resolution kinematic maps for an irregular galaxy (DEEP2-12008898S smoothed by FWHM = 1.5 pixel) and a disk candidate (UDS11655 smoothed by FWHM = 2.0 pixel) are shown in Figure 12.

We apply a local velocity gradient correction to the dispersion. Half of the biggest velocity difference between vertical or horizontal immediate neighbor pixels, $\Delta v = 0.5 \times \max(|v_{i+1,j} - v_{i-1,j}|, |v_{i,j+1} - v_{i,j-1}|)$, is subtracted from the local dispersion in quadrature, $\sigma^{\text{corr}} = \sqrt{\sigma^2 - \Delta v^2}$. The S/N weighted average of σ^{corr} in our sample is typically $\sim 60 \text{ km s}^{-1}$, compared to $\sim 64 \text{ km s}^{-1}$ for the non-corrected σ_{ave} , which indicates the local velocity gradient within a pixel is small compared to the line-of-sight dispersion.

We also investigate the effects of beam smearing on the observed velocities. Using one of the highest S/N sources in the sample, we find the un-smoothed data to have a dispersion lower by $\sim 4 \text{ km s}^{-1}$ compared to the smoothed data set. When the additional local gradient correction is applied to the un-smoothed data, the dispersion is lowered further by $\sim 5 \text{ km s}^{-1}$. This confirms our local velocity gradient correction analysis with the smoothed data sets.

Overall the line-of-sight velocity dispersion measurements are resolved (i.e., measured widths are not the widths of smoothing nor local rotation), and after the local gradient

corrections have been applied, they are found to be $\gtrsim 55 \text{ km s}^{-1}$ across our sample. As shown in previous studies, this is significantly higher than velocity dispersions found in local galaxies. We note that our method for removing the local velocity gradient is not rigorous: we have included it to provide a rough quantitative estimate of the contribution of our finite spatial resolution to the line of sight dispersion. For the rest of our analysis, we will not apply this correction, which as we have shown has a $\lesssim 10\%$ effect on our results.

For the two galaxies shown in Figure 12, v_{shear} is reduced by 16% (irregular) and by 22% (disk). This is consistent with the expectation that smoothing softens velocity gradients, and may result in an underestimate of v_{shear} in the disk candidates. Smoothing is nonetheless necessary since, as shown by Figure 12, the increased S/N of the observations allows more robust kinematics measurements on each of the sources.

APPENDIX C KINEMATIC MAPS

In this section, we show IROCKS $\text{H}\alpha$ flux, radial velocity, and velocity dispersion maps, extracted from the OSIRIS data cube in Figure 13. When available, *HST* images are also shown.

APPENDIX D 1D SPECTRUM

In this section, spatially integrated 1D spectra of IROCKS samples are shown in Figure 14. When the target is a multiple system, we spatially separate them and make an individual 1D spectrum.

APPENDIX E NOTES ON INDIVIDUAL GALAXIES

In this section we briefly describe the OSIRIS results of individual galaxies. For galaxies that are classified as “multiple” in Section 2.3.3, their individual $\text{H}\alpha$ flux, radial velocity, and velocity dispersion maps are shown in Figure 15.

E.1. UDS11655

This is one of four IROCKS disk candidates whose *HST* rest frame UV image shows disk-like morphology with a spiral arm pattern. The OSIRIS kinematic map is well fitted by a disk model (P.A. = 125° , $V_p = 140 \text{ km s}^{-1}$), with a small residual $\langle \Delta \rangle = 13.4 \text{ km s}^{-1}$. It has σ_{ave} of 55 km s^{-1} , with higher dispersion ($\sim 80 \text{ km s}^{-1}$) along the rotation axis and lower ($\sim 20 \text{ km s}^{-1}$) off axis. This is the typical velocity dispersion structure for a disk galaxy. The stellar mass is $\log M_*/M_\odot = 10.22$ with estimated gas fraction of $\sim 56\%$. The virial mass $\log M_{\text{vir}}/M_\odot = 10.35$, the enclosed mass $\log M_{\text{enc}}/M_\odot = 10.49$, and the halo mass $\log M_{\text{halo}}/M_\odot = 11.80$. The $\text{H}\alpha$ detected size is almost the same as the *HST* image, and we align the two by matching the overall structures.

E.2. UDS10633

This source has the largest stellar mass estimate ($\log M_*/M_\odot = 11.24$) among our sample. The rest frame UV image from the *HST* shows a compact source in the north, a bar-like structure in the south, and another compact source in the south-west. The $\text{H}\alpha$ does not show all of these

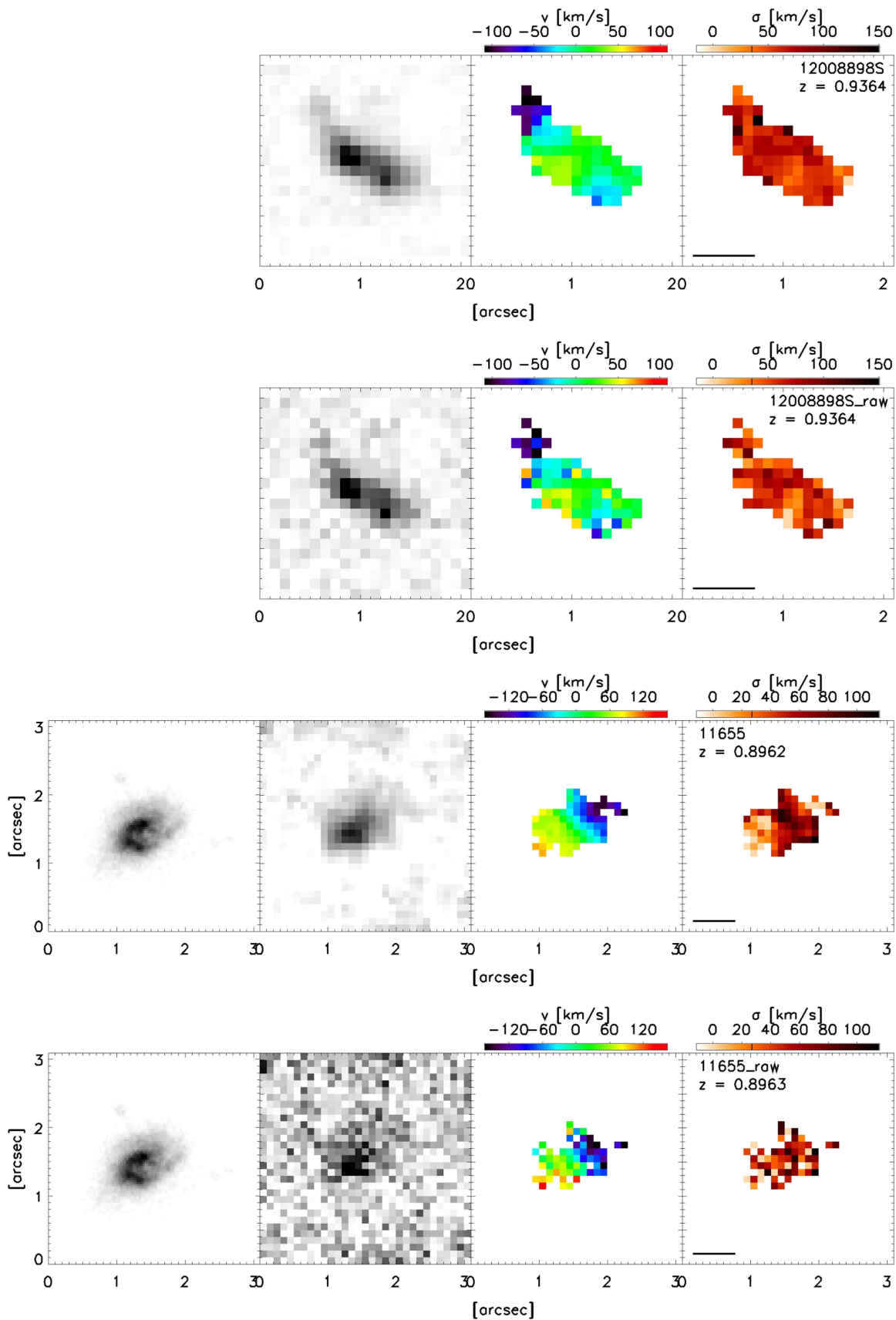


Figure 12. From the left, *HST* (when available), $H\alpha$, rotation velocity, and velocity dispersion maps of DEEP2-12008898S smoothed (first row) and unsmoothed (second row) as an example of irregular galaxy, and UDS-11655 smoothed (third row) and unsmoothed (bottom) as an example of disk galaxy. The smoothing FWHM of DEEP2-12008898S is 1.5 pixel, and that of UDS-11655 is 2.0 pixel.

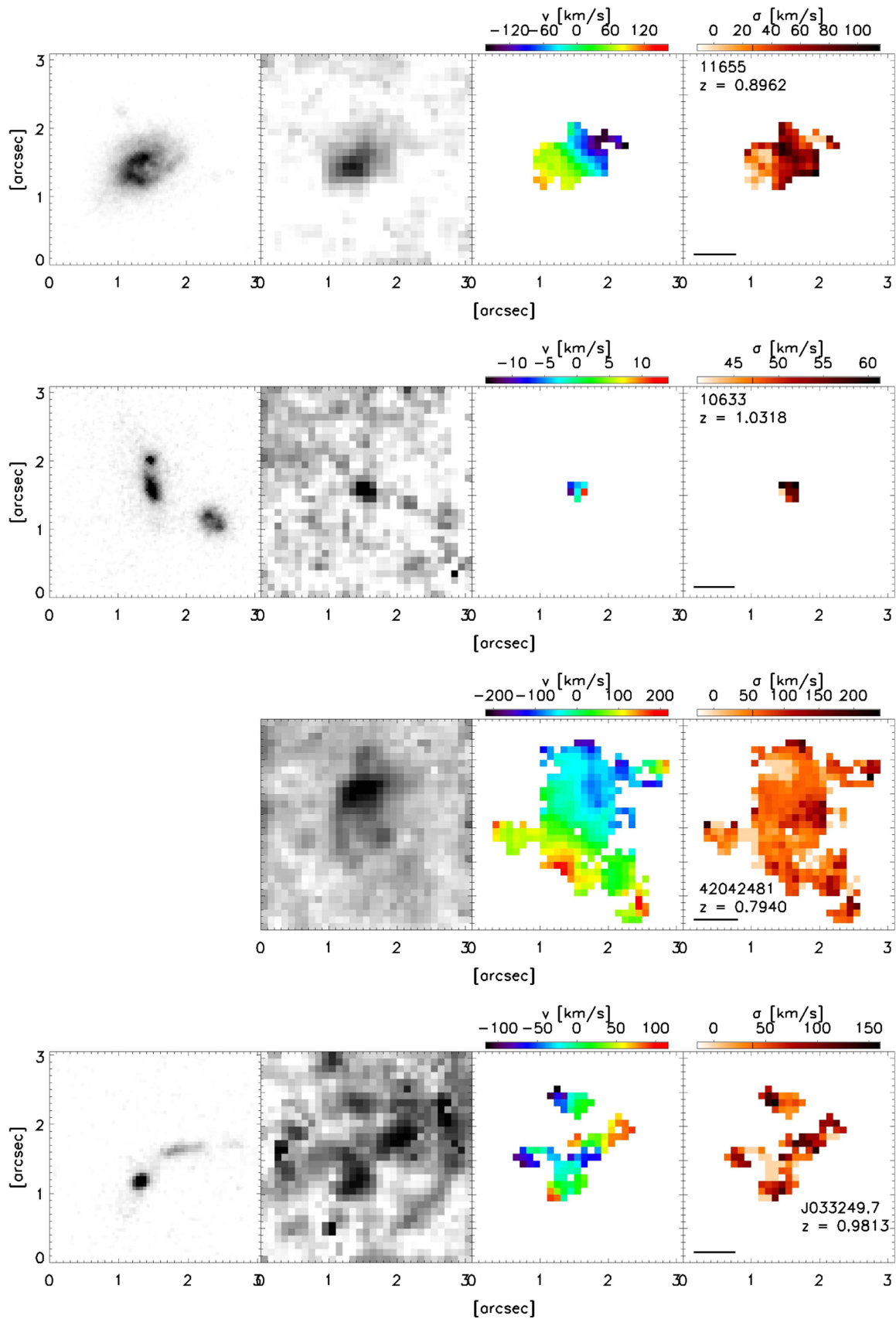


Figure 13. From the left, *HST* (when available), $H\alpha$ flux, radial velocity, and velocity dispersion maps. The orientation of the images are fixed to be north up and east to the left. In the right panel, the name of the source and its redshift are shown in the top (or other location when the text overlaps with the map), and the length of the black line on the left bottom corner represents a projected size of 5 kpc at the redshift of the galaxy. All *HST* images are taken by F814W filter, except for J033249.7 (F606W), TKRS11169 (F850LP), TKRS9727 (F850LP), and TKRS7615 (F850LP).

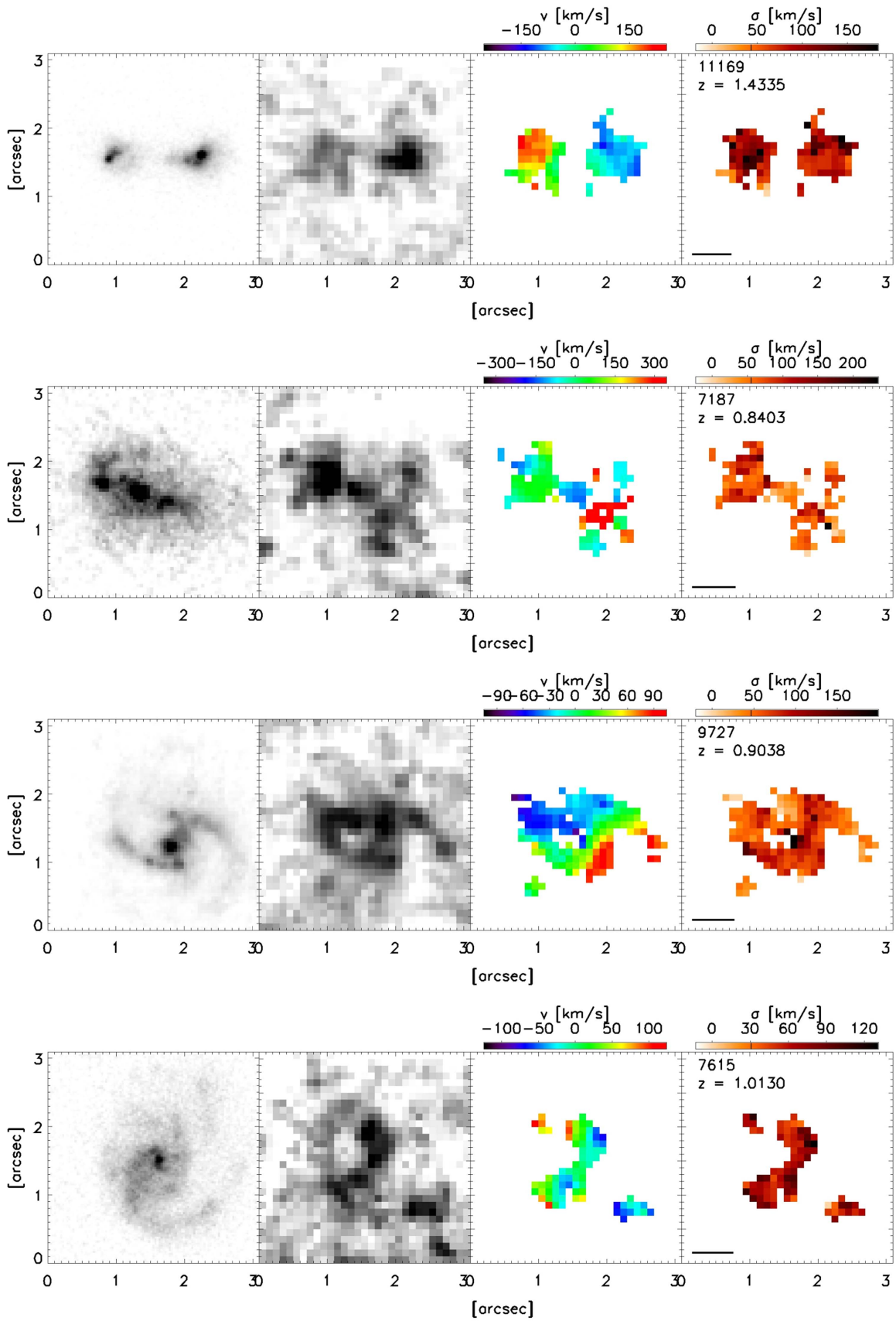


Figure 13. (Continued.)

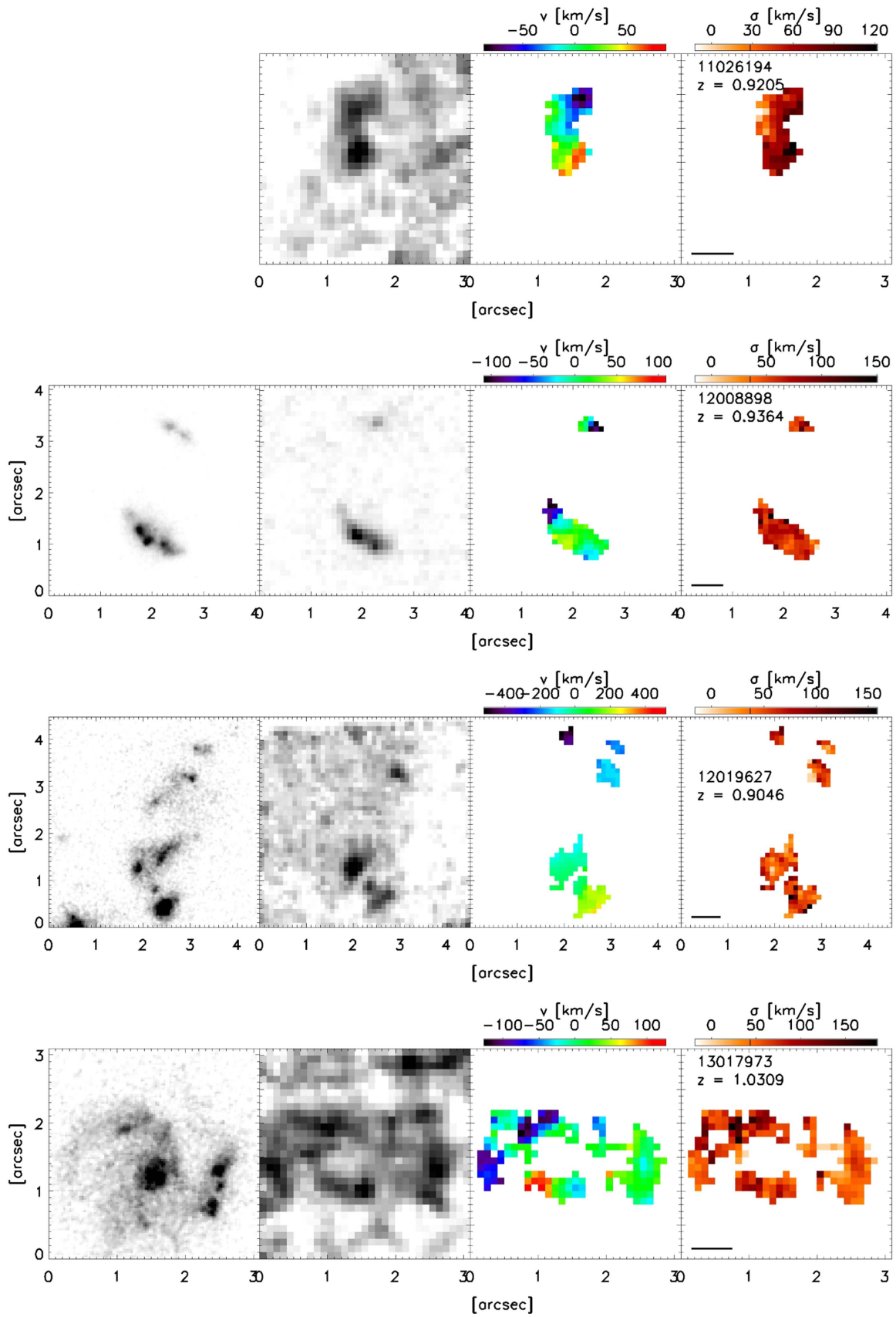


Figure 13. (Continued.)

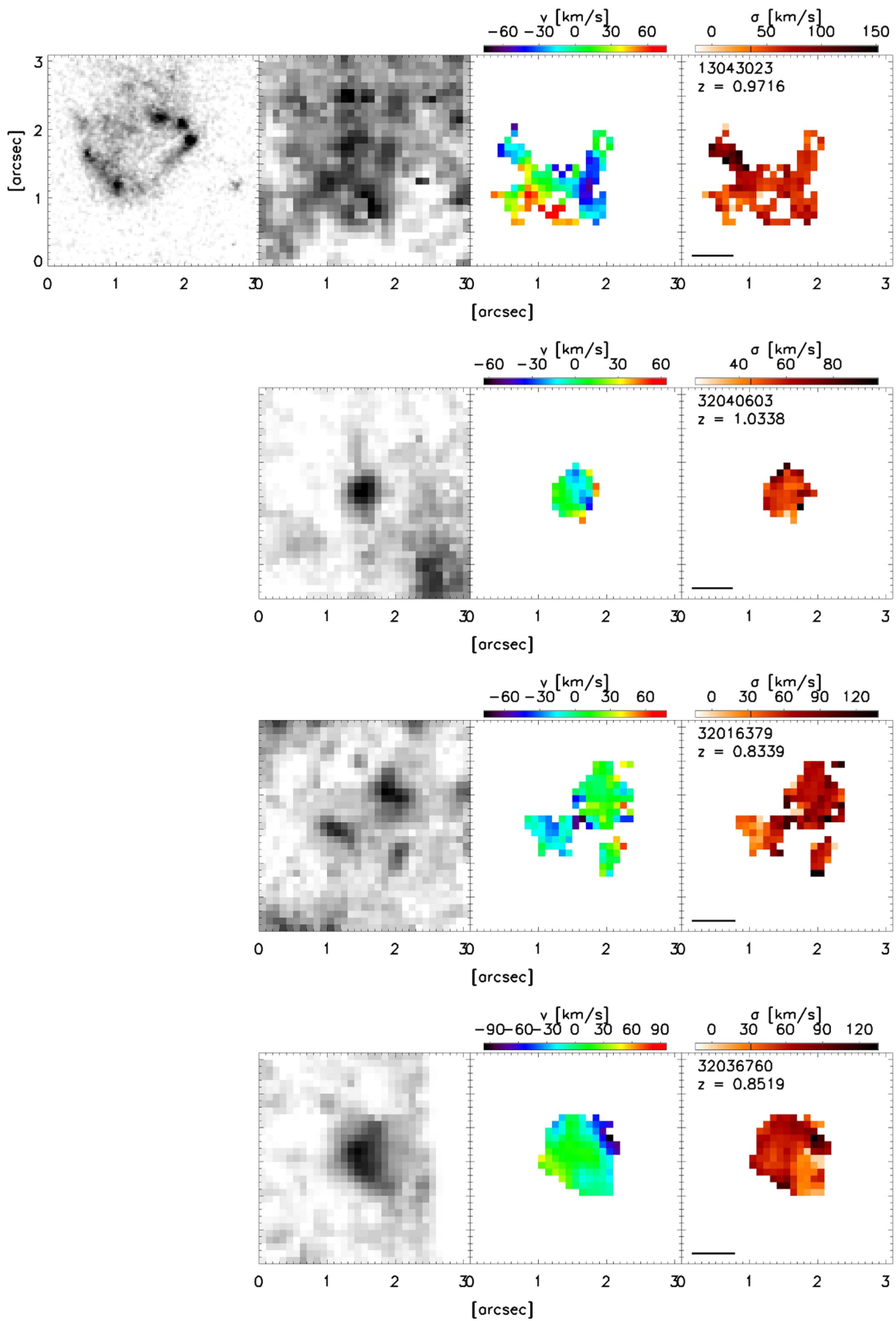


Figure 13. (Continued.)

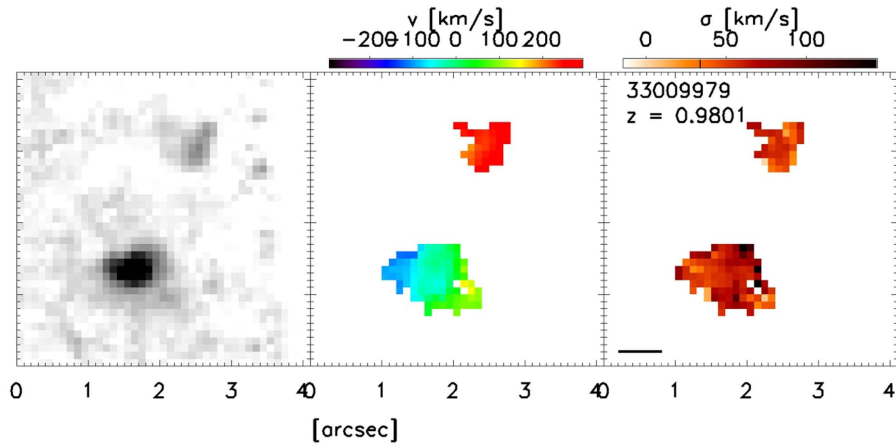


Figure 13. (Continued.)

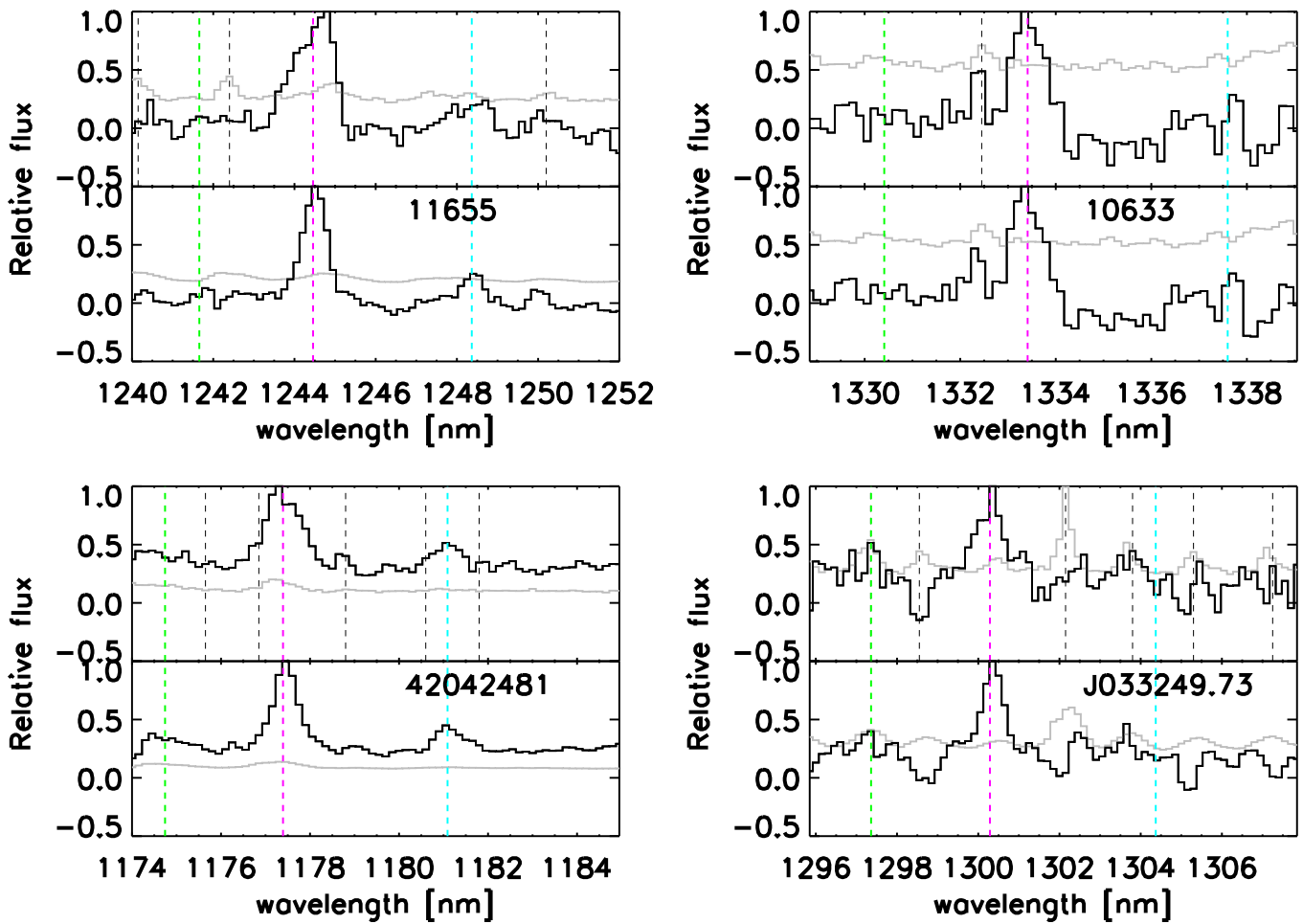


Figure 14. Spatially integrated 1D spectra (sum of all spectra in segmentation maps) of each component in IROCKS, covering the spectral region around the redshifted $H\alpha$ emission line. When the integrated spectrum has only one $H\alpha$ peak, the source has only one component and is classified as a single source. When the integrated spectrum has more than one $H\alpha$ peak, the source is classified as multiple, and components are spatially separated. The west component of 7187 still has more than one spectral peak, but different components are difficult to spatially separate, thus it is treated as one component. 1σ noise is plotted in gray. The magenta dashed line is the location of the $H\alpha$ peak, and green and cyan lines are location of [NII]6548 and [NII]6583 based on the centroid of the $H\alpha$ line. Top: spectra in the segmentation map are simply summed up. Dashed black vertical lines are the location of strong sky OH lines measured using non-sky-subtracted data. Bottom: spatially integrated spectra in the segmentation map, but individual spectra are shifted so that all Gaussian fitted $H\alpha$ line peaks match at a single redshift, which is the Gaussian peak of the integrated 1D spectrum (z_{sys} in Table 2), to increase the line signal.

components. To align the two images, we match the south tip of the bar in *HST* to that of the $H\alpha$ image. Due to its unresolved size, v_{shear} value is negligible, but σ_{ave} is still high

($\sigma_{\text{ave}} = 54.5 \text{ km s}^{-1}$). Since some components are not detected, dynamical mass estimates from OSIRIS should be considered lower limits.

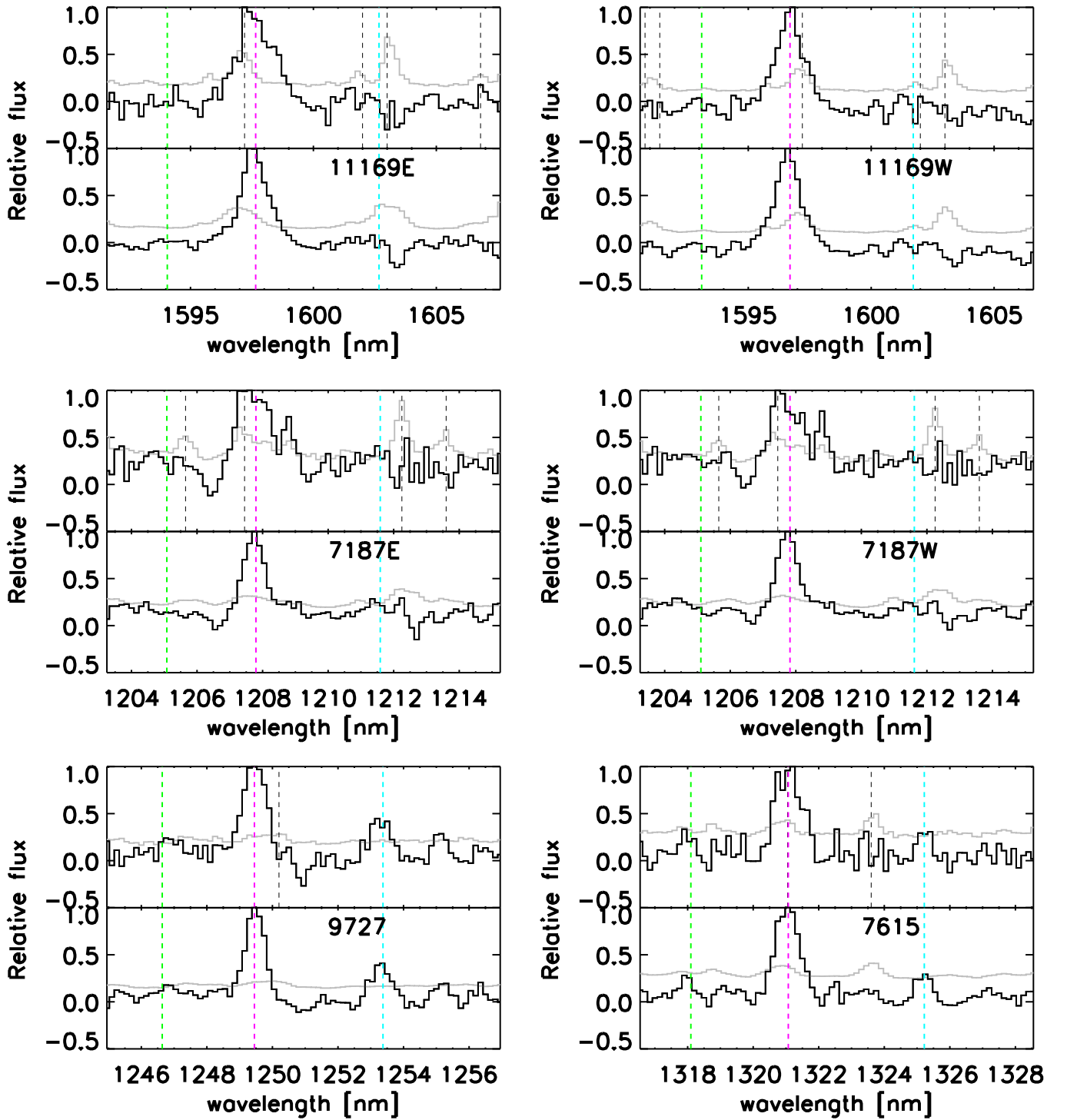


Figure 14. (Continued.)

E.3. DEEP2-42042481

This is the largest single-component galaxy in the IROCKS sample. It is one of four IROCKS disk candidates and has one of the higher v_{shear} ($v_{\text{shear}} = 180 \text{ km s}^{-1}$) and $v_{\text{shear}}/\sigma_{\text{ave}}$ ($v_{\text{shear}}/\sigma_{\text{ave}} = 2.70$) values in our sample. The OSIRIS kinematic map is well fitted by a disk model (P.A. = 153° , $V_p = 152 \text{ km s}^{-1}$) with a low residual, $\langle \Delta \rangle = 23.6 \text{ km s}^{-1}$. The velocity dispersion has a slope that is perpendicular to the rotation axis, which is similar to disk galaxy velocity profiles. It

has the stellar mass $\log M_*/M_\odot = 10.62$ and the lowest gas fraction (22%) among the four IROCKS disk candidates.

E.4. J033249.73

HST imaging in rest-frame UV shows a compact component in the east connected to a stretched arch component in the west. We match the bright compact source in *HST* with the bright $\text{H}\alpha$ detection to the south-east. The $\text{H}\alpha$ kinematic map does not show a velocity gradient, and the velocity dispersion varies

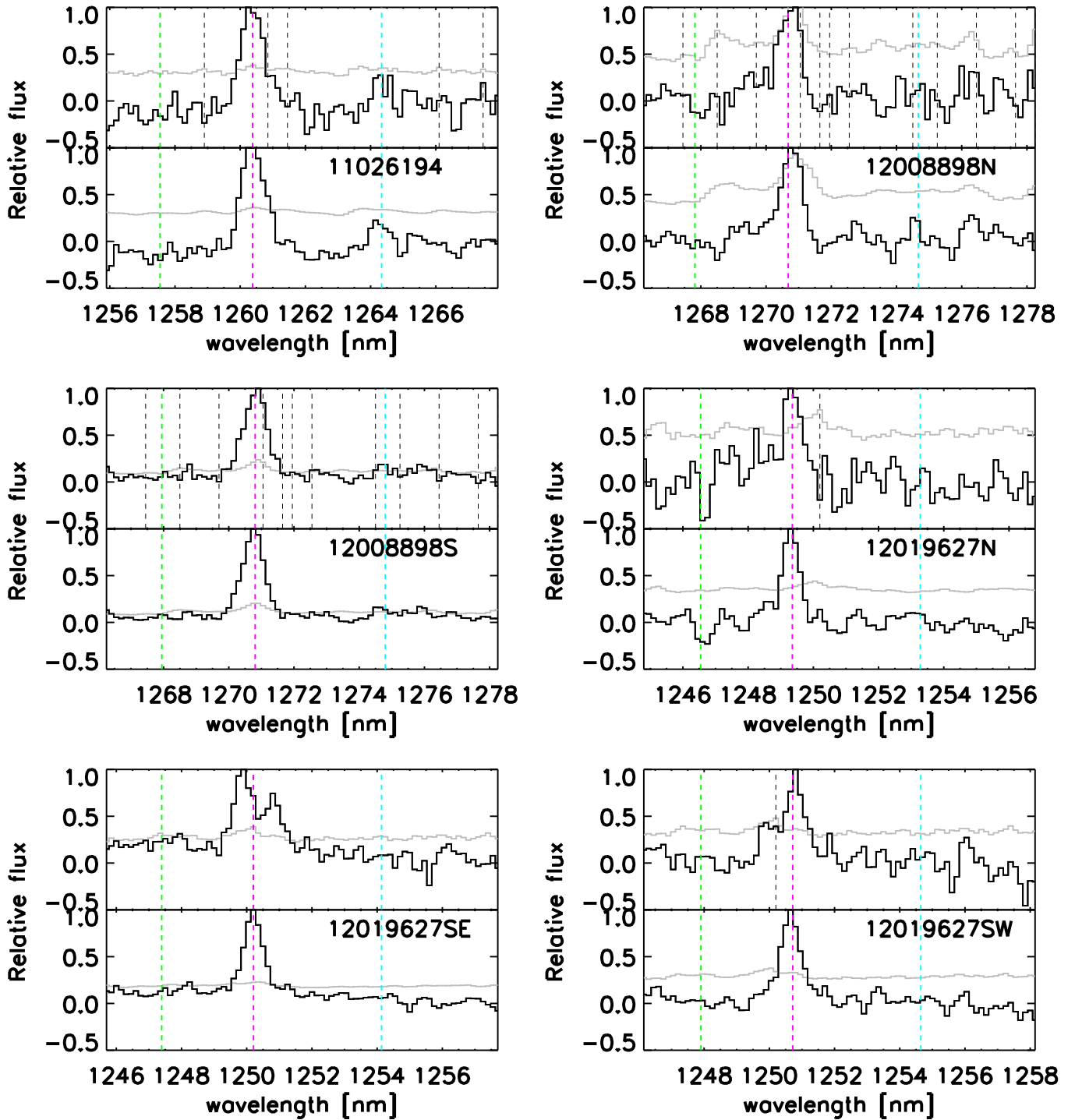


Figure 14. (Continued.)

across the whole galaxy. The east component has a lower dispersion of $<30 \text{ km s}^{-1}$ while the west arch component has higher ($\sim 100 \text{ km s}^{-1}$) dispersion.

E.5. TKRS11169

This is the only source at $z \sim 1.4$ in our sample. It is classified as an AGN by X-ray observation. *HST* imaging shows two distinct components in the east and west, and both are resolved by $\text{H}\alpha$ and aligned to the *HST* images. The west component is brighter than the east by a factor of 1.5. Both

components have significantly higher σ_{ave} of $\sim 90 \text{ km s}^{-1}$ than the rest of the $z \sim 1$ sources.

E.6. TKRS7187

HST imaging shows three brighter spots (east, center, west) and $m = 2$ like spiral arms, but $\text{H}\alpha$ does not show a velocity gradient to support the disk model. The central bright spot in *HST* is matched with the central nod in the $\text{H}\alpha$ detection. After separating components using the 1D spectrum, the west component still has more than one peak in the 1D spectrum

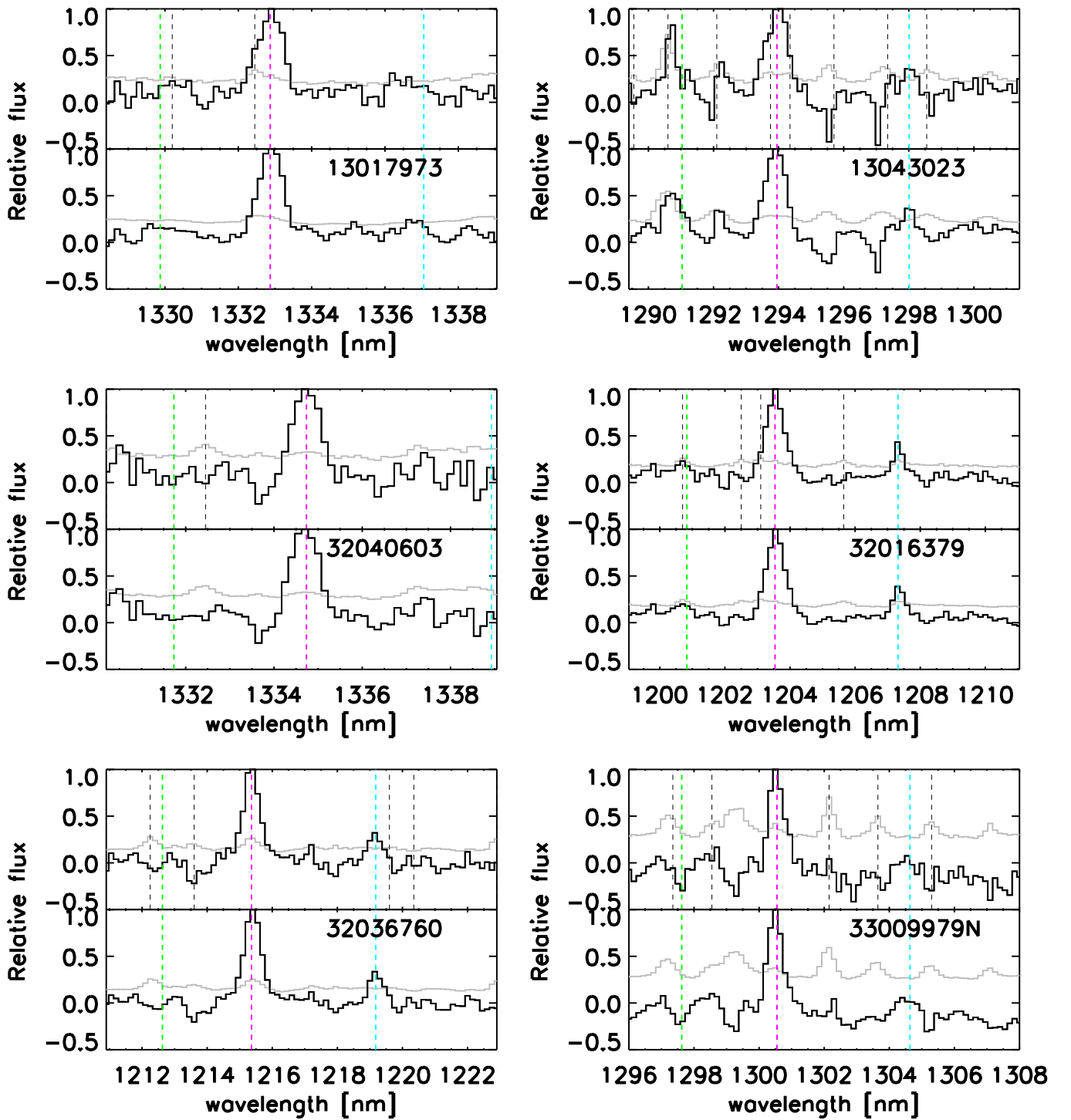


Figure 14. (Continued.)

that could not be spatially separated. This component has the highest v_{shear} of 240 km s^{-1} in our sample and hence is most likely an interacting system.

E.7. TKRS9727

Among the resolved IROCKS sample, this has the largest stellar mass ($\log M_*/M_\odot = 11.0$) in our sample. It also has the highest SFR_{SED} ($159 M_\odot \text{ yr}^{-1}$) and H II+ISM corrected SFR ($\text{SFR}_{\text{H}\alpha}^{\text{00}} = 108 M_\odot \text{ yr}^{-1}$) with the highest τ_V (3.66). This is one

of four IROCKS disk candidates whose *HST* image at rest frame UV shows $m = 2$ face-on spiral galaxy morphology, and the OSIRIS kinematic map is well fitted by a disk model (P.A. = 224° , $V_p = 110 \text{ km s}^{-1}$) with the smallest residual ($\langle \Delta \rangle = 13.2 \text{ km s}^{-1}$). The galaxy has $\sim 55\%$ gas fraction. We align the central bar-like feature in *HST* with the central thick part of H α , and match the *HST* north-west arm with the two H α nodes in north-west and the *HST* south-east arm with the south-east extended curved feature in H α .

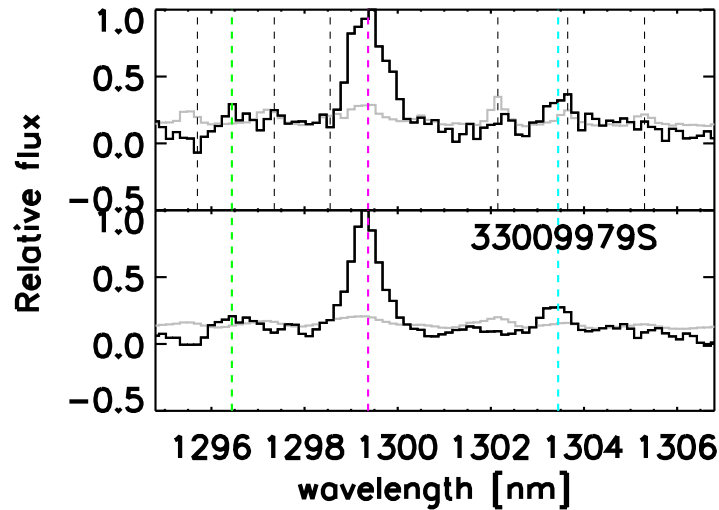


Figure 14. (Continued.)

E.8. TKRS7615

The *HST* image at rest frame UV shows face-on grand design spiral galaxy morphology, and the OSIRIS rotation map shows a subtle variation/gradient across the galaxy. Velocity dispersion is roughly uniform across the whole galaxy at around 70 km s^{-1} . This can be a face-on disk, but the rotation variation detected by OSIRIS is too small to fit a disk model. The bright $\text{H}\alpha$ north part is matched with the central nod in *HST*, and the arch-like south-east extended component to the south-west nod in $\text{H}\alpha$ is matched to the spiral arm in *HST*.

E.9. DEEP2-11026194

The $\text{H}\alpha$ kinematic map shows velocity gradient (blueshifted at the north and redshifted at the south); however, due to its small detected region, the disk fitting is insufficient to determine if it is disk candidate. The velocity dispersion varies along the rotation axis, $\sim 20 \text{ km s}^{-1}$ in the east to $\sim 100 \text{ km s}^{-1}$ in the east.

E.10. DEEP2-12008898

This is one of the best detected sources in our observations and used for the local rotation and smoothing correction analysis in Section 4.1. The system has two distinct components, a small one in the north and a large one in the south. Both components are seen both in *HST* and $\text{H}\alpha$. The north component: while *HST* shows two nodes (north-east and south-west) extended ~ 1 arcsec, $\text{H}\alpha$ shows one nod of ~ 0.5 arcsec in the north-east. It has some velocity gradient, but it is too undersampled to fit to a disk model. The velocity dispersion is almost uniform around 60 km s^{-1} . The south component: $\text{H}\alpha$ and *HST* extend almost the same length, and three nodes are seen in *HST* while two are seen in $\text{H}\alpha$. The rotation shows redshifts at the center and blueshift at the outside. The velocity dispersion is almost uniform ($\sim 70 \text{ km s}^{-1}$) over the whole galaxy, but slightly lower ($\sim 40 \text{ km s}^{-1}$) at the center. From the velocity structure and multiple nodes, the south component is probably an interacting system. We match the north-east nod in *HST* with the $\text{H}\alpha$ north component, and the overall shape of the south component.

E.11. DEEP2-12019627

Both *HST* and $\text{H}\alpha$ show patchy morphology. We separate three $\text{H}\alpha$ north nodes as the north component and the south ribbon shape part into the south-east and south-west components. The north component: three $\sim 0''.5$ $\text{H}\alpha$ nodes are spatially separated but are individually too small to form separate peaks in the 1D spectrum, and hence the three together form a north component. They are also individually too small to see individual rotation. The south-east and south-west components: both velocity fields show a gradient but are undersampled to fit with disk models. Due to their complicated morphologies, the system is probably an interacting system. Because this source has many components, we align *HST* and $\text{H}\alpha$ detection so that all $\text{H}\alpha$ components are on the bright part of *HST*, except the northmost component in $\text{H}\alpha$.

E.12. DEEP2-13017973

This is the only source in our sample detected with the old OSIRIS grating, and therefore the $\text{H}\alpha$ emission is slightly noisier than the majority of the sample. The *HST* image shows a few distinct knots in a spiral disk-like morpholog, but is quite distinct from the observed $\text{H}\alpha$ morphology. We match a few western knots in the *HST* image with that of the extended component observed in the west in $\text{H}\alpha$. The rotation map does not show a velocity gradient. This galaxy has the highest uncorrected SFR ($42.7 M_{\odot} \text{ yr}^{-1}$), and the second highest $\text{H II} + \text{ISM}$ -corrected SFR ($65.8 M_{\odot} \text{ yr}^{-1}$) among $z \sim 1$ IROCKS sample.

E.13. DEEP2-13043023

The *HST* image shows an irregular morphology with three knots in the north-west region and two in the south-east region. The $\text{H}\alpha$ image was matched to the *HST* arch connecting the south knot to the north-east knots in *HST*. The rotation map does not show a velocity gradient, and the dispersion is uniform around 50 km s^{-1} except for the north-east arm at $\sigma = 120 \text{ km s}^{-1}$.

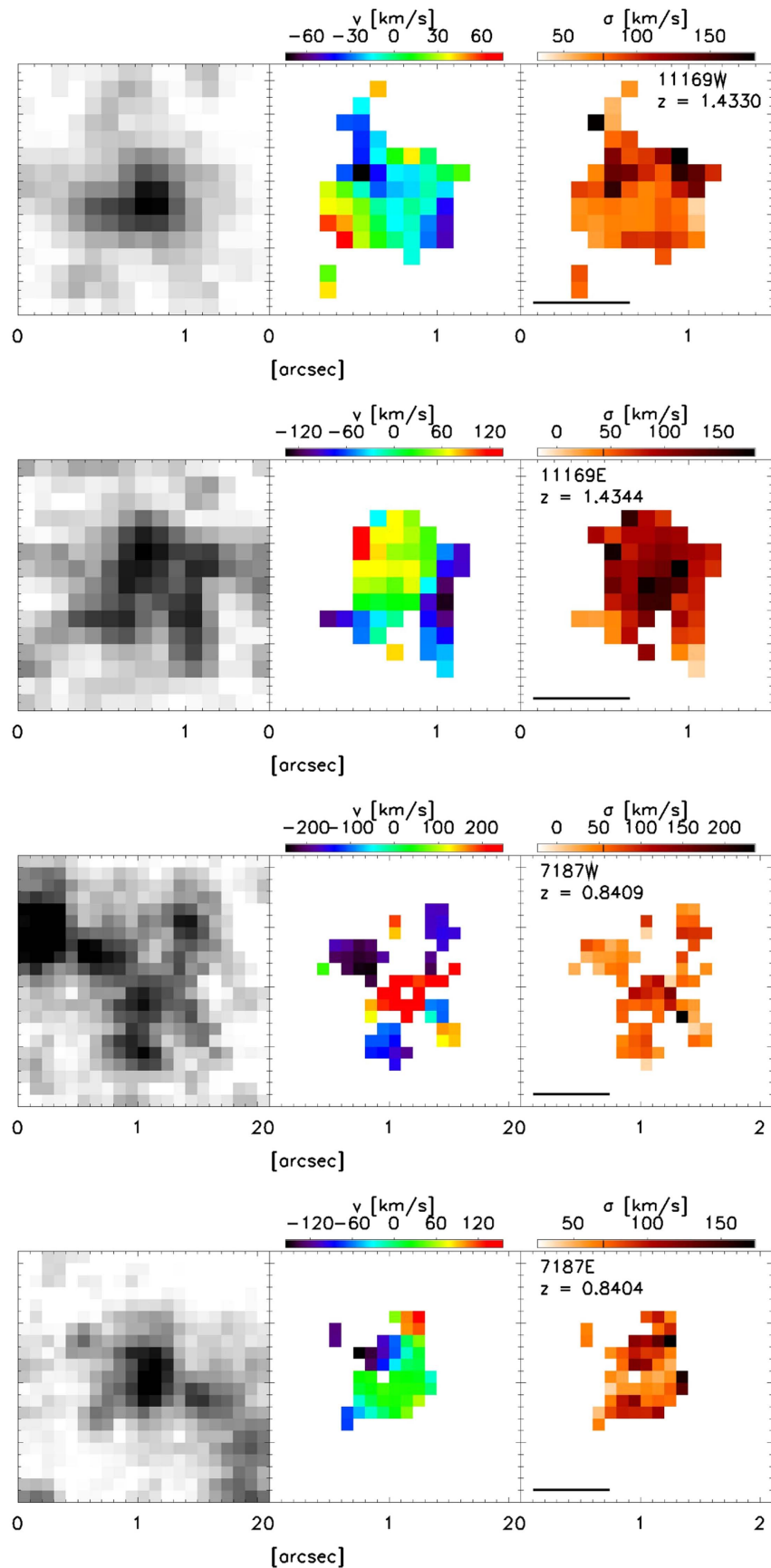


Figure 15. $H\alpha$ flux, rotation velocity, and velocity dispersion maps of individually separated components for the galaxies that are classified as “multiple,” 11169 (east and west), 7187 (east and west), 12008898 (north and south), 12019627 (north, south–east, and south–west), and 33009979 (north and south). “Multiple” galaxies are classified using peaks in their integrated 1D spectra or their spatially well separated components (Section 2.3.3).

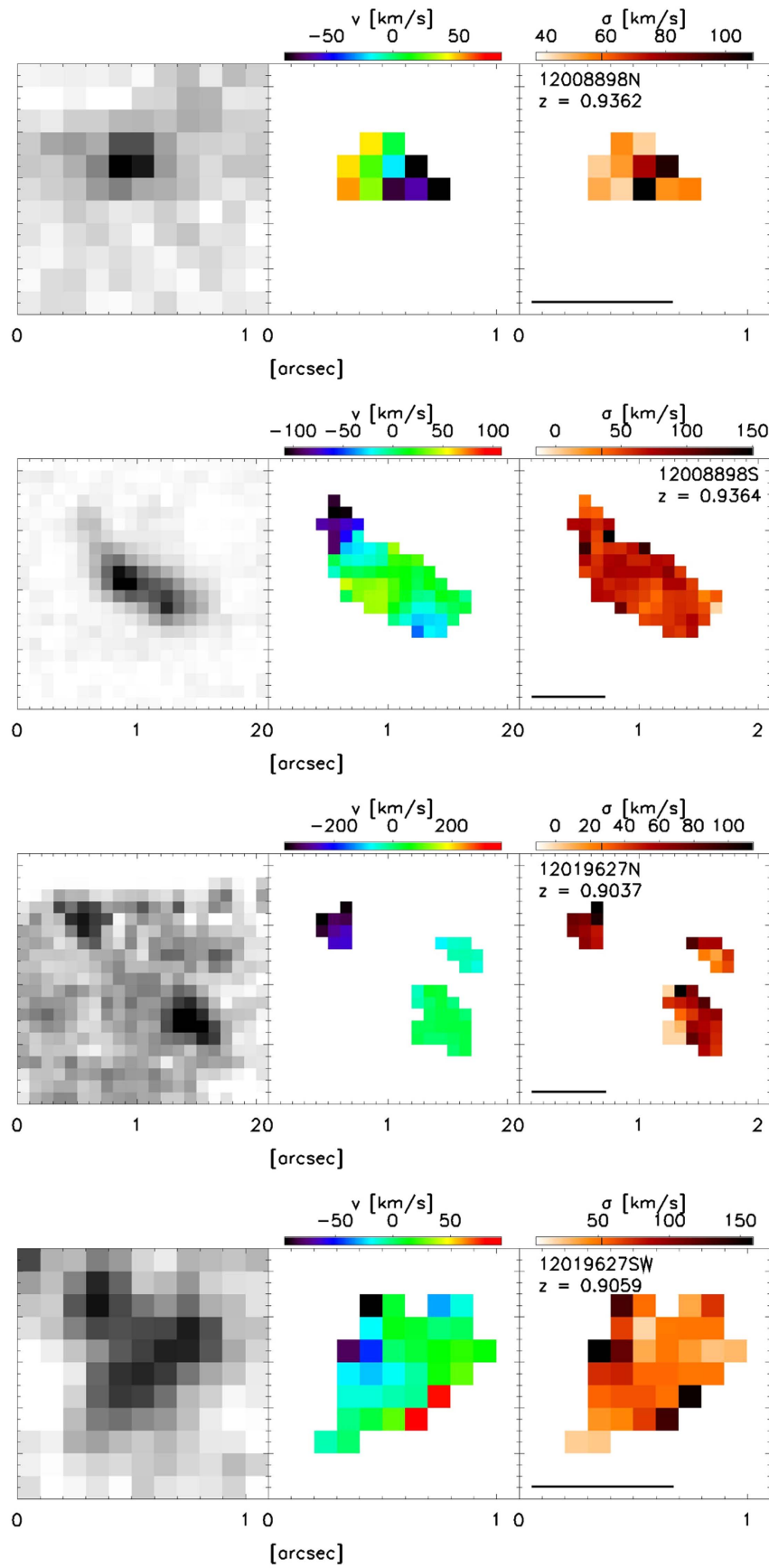


Figure 15. (Continued.)

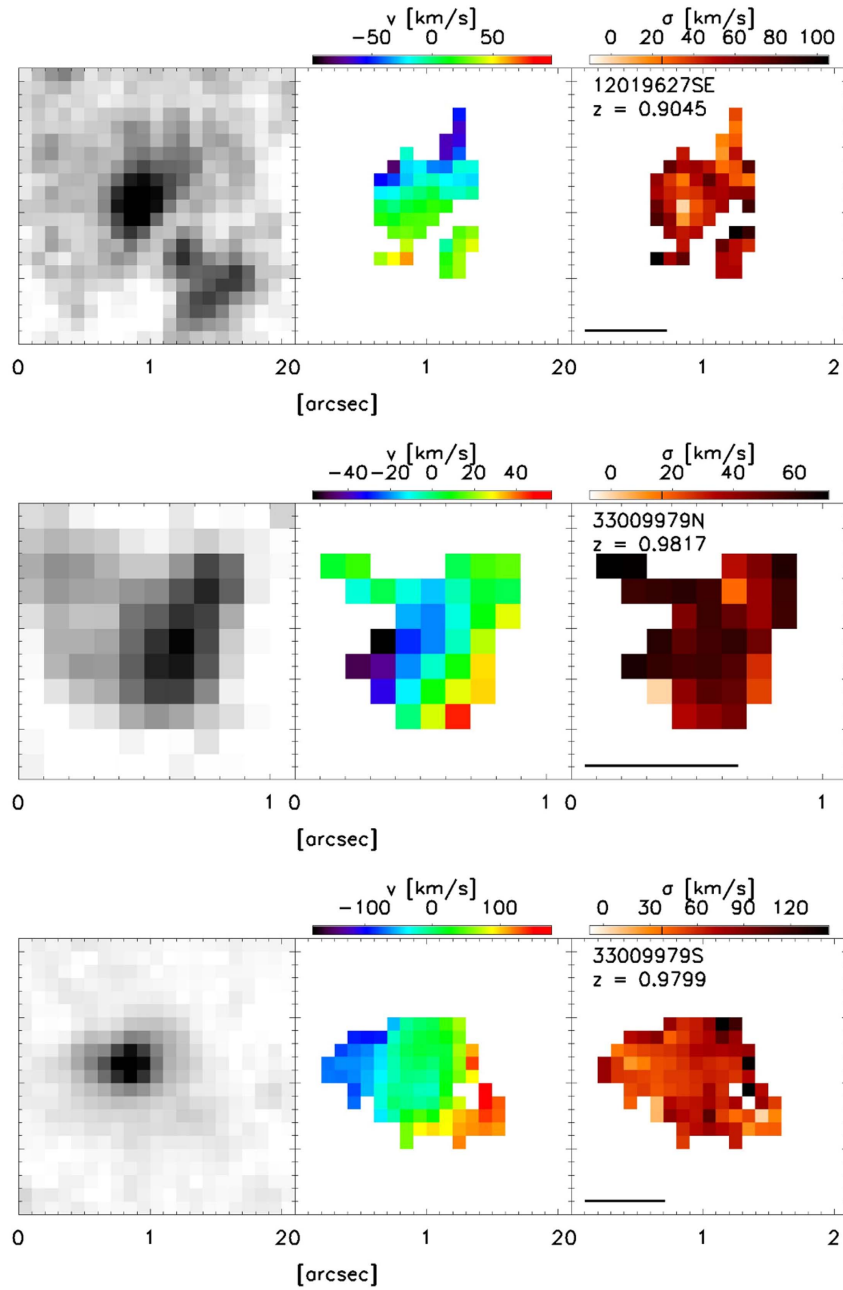


Figure 15. (Continued.)

E.14. DEEP2-32040603

This is the highest-redshift galaxy ($z = 1.0338$) among IROCKS $z \sim 1$ sample. It can be rotating (blueshift at the north-west and redshift at the south-east), but the surface area of H α is not sufficient to fit a disk model. The velocity dispersion is constant over the galaxy at $\sigma \sim 55 \text{ km s}^{-1}$.

E.15. DEEP2-32016379

The H α map shows a dual cone-like morphology and the rotation map shows almost no rotation except in the eastern region where it is slightly blueshifted by $\sim 20 \text{ km s}^{-1}$. The dispersion map is constant $\sigma \sim 60 \text{ km s}^{-1}$, except the eastern part, $\sigma \sim 30 \text{ km s}^{-1}$.

E.16. DEEP2-32036760

The H α emission is in a compact single source with only a slight velocity gradient of $\sim 60 \text{ km s}^{-1}$, and a lower velocity dispersion in the south-west ($\sigma \sim 20 \text{ km s}^{-1}$) region compared to the entire source of ($\sigma \sim 60 \text{ km s}^{-1}$).

E.17. DEEP2-33009979

This system has two well separated components in the north and south. The north component shows a slight velocity gradient, but it is not well fit to an inclined disk model. The velocity dispersion in the north component is uniform at 50 km s^{-1} . The southern component is one of the four disk candidates and is well fitted by a disk model (P.A. = 250° , $V_p = 81.7 \text{ km s}^{-1}$) with a velocity residual of $\langle \Delta \rangle = 30.8 \text{ km s}^{-1}$. The velocity dispersion is

uniform over the galaxy at $\sigma \sim 60 \text{ km s}^{-1}$. The velocity field deviates near the center compared to the whole galaxy (see Figure 5), and to help with the disk fitting model we have enforced that the dynamical center is at the $H\alpha$ flux peak.

REFERENCES

- Abraham, R. G., Nair, P., McCarthy, P. J., et al. 2007, *ApJ*, 669, 184
 Abraham, R. G., van den Bergh, S., & Nair, P. 2003, *ApJ*, 588, 218
 Agertz, O., Kravtsov, A. V., Leitner, S. N., & Gnedin, N. Y. 2013, *ApJ*, 770, 25
 Alexander, D. M., Bauer, F. E., Brandt, W. N., et al. 2003, *AJ*, 126, 539
 Appenzeller, I., Fricke, K., Fürtig, W., et al. 1998, *Msngr*, 94, 1
 Begeman, K. G. 1987, PhD thesis, Kapteyn Institute
 Bournaud, F. 2016, *Ap&SS*, 418, 355
 Bruzual, G., & Charlot, S. 2003, *MNRAS*, 344, 1000
 Calzetti, D. 2001, *PASP*, 113, 1449
 Chabrier, G. 2003, *PASP*, 115, 763
 Charlot, S., & Fall, S. M. 2000, *ApJ*, 539, 718
 Chin, J. C. Y., Stalcup, T., Wizinowich, P., et al. 2010, *Proc. SPIE*, 7736, 77361
 Chin, J. C. Y., Wizinowich, P., Campbell, R., et al. 2012, *Proc. SPIE*, 8447, 84474
 Cowie, L. L., Hu, E. M., & Songaila, A. 1995, *AJ*, 110, 1576
 Davies, R. I. 2007, *MNRAS*, 375, 1099
 Elmegreen, D. M., Elmegreen, B. G., Marcus, M. T., et al. 2009, *ApJ*, 701, 306
 Elmegreen, D. M., Elmegreen, B. G., Ravindranath, S., & Coe, D. A. 2007, *ApJ*, 658, 763
 Epinat, B., Contini, T., Le Fèvre, O., et al. 2009, *A&A*, 504, 789
 Epinat, B., Tasca, L., Amram, P., et al. 2012, *A&A*, 539, A92
 Erb, D. K., Steidel, C. C., Shapley, A. E., et al. 2006a, *ApJ*, 647, 128
 Erb, D. K., Steidel, C. C., Shapley, A. E., et al. 2006b, *ApJ*, 646, 107
 Faber, S. M., Phillips, A. C., Kibrick, R. I., et al. 2003, *Proc. SPIE*, 4841, 1657
 Förster Schreiber, N. M., Genzel, R., Bouché, N., et al. 2009, *ApJ*, 706, 1364
 Förster Schreiber, N. M., Genzel, R., Lehnert, M. D., et al. 2006, *ApJ*, 645, 1062
 Förster Schreiber, N. M., Shapley, A. E., Erb, D. K., et al. 2011a, *ApJ*, 731, 65
 Förster Schreiber, N. M., Shapley, A. E., Genzel, R., et al. 2011b, *ApJ*, 739, 45
 Galametz, A., Grazian, A., Fontana, A., et al. 2013, *ApJS*, 206, 10
 Genel, S., Bouché, N., Naab, T., Sternberg, A., & Genzel, R. 2010, *ApJ*, 719, 229
 Genzel, R., Newman, S., Jones, T., et al. 2011, *ApJ*, 733, 101
 Genzel, R., Tacconi, L. J., Lutz, D., et al. 2015, *ApJ*, 800, 20
 Glazebrook, K. 2013, *PASA*, 30, 56
 Gonçalves, T. S., Basu-Zych, A., Overzier, R., et al. 2010, *ApJ*, 724, 1373
 Governato, F., Willman, B., Mayer, L., et al. 2007, *MNRAS*, 374, 1479
 Guo, Y., Ferguson, H. C., Bell, E. F., et al. 2015, *ApJ*, 800, 39
 Guo, Y., Giavalisco, M., Ferguson, H. C., Cassata, P., & Koekemoer, A. M. 2012, *ApJ*, 757, 120
 Hopkins, P. F., Kereš, D., Murray, N., Quataert, E., & Hernquist, L. 2012, *MNRAS*, 427, 968
 Hung, C.-L., Rich, J. A., Yuan, T., et al. 2015, *ApJ*, 803, 62
 Jones, T. A., Swinbank, A. M., Ellis, R. S., Richard, J., & Stark, D. P. 2010, *MNRAS*, 404, 1247
 Jung, M. K. R., & Mac Low, M.-M. 2006, *ApJ*, 653, 1266
 Juneau, S., Dickinson, M., Alexander, D. M., & Salim, S. 2011, *ApJ*, 736, 104
 Kashino, D., Silverman, J. D., Rodighiero, G., et al. 2013, *ApJL*, 777, L8
 Kassín, S. A., Brooks, A., Governato, F., Weiner, B. J., & Gardner, J. P. 2014, *ApJ*, 790, 89
 Kassín, S. A., Weiner, B. J., Faber, S. M., et al. 2012, *ApJ*, 758, 106
 Kennicutt, R. C., Jr. 1998, *ApJ*, 498, 541
 Kennicutt, R. C., Jr., Calzetti, D., Walter, F., et al. 2007, *ApJ*, 671, 333
 Lang, P., Wuyts, S., Somerville, R. S., et al. 2014, *ApJ*, 788, 11
 Larkin, J., Barczys, M., Krabbe, A., et al. 2006, *Proc. SPIE*, 62691A
 Law, D. R., Steidel, C. C., Erb, D. K., et al. 2007a, *ApJ*, 669, 929
 Law, D. R., Steidel, C. C., Erb, D. K., et al. 2007b, *ApJ*, 656, 1
 Law, D. R., Steidel, C. C., Erb, D. K., et al. 2009, *ApJ*, 697, 2057
 Livermore, R. C., Jones, T., Richard, J., et al. 2012, *MNRAS*, 427, 688
 Livermore, R. C., Jones, T. A., Richard, J., et al. 2015, *MNRAS*, 450, 1812
 Lotz, J. M., Primack, J., & Madau, P. 2004, *AJ*, 128, 163
 Mathews, D. J., Newman, J. A., Coil, A. L., Cooper, M. C., & Gwyn, S. D. J. 2013, *ApJS*, 204, 21
 McLean, I. S., Steidel, C. C., Epps, H., et al. 2010, *Proc. SPIE*, 7735, 77351
 McLean, I. S., Steidel, C. C., Epps, H. W., et al. 2012, *Proc. SPIE*, 8446, 84460
 Mieda, E., Wright, S. A., Larkin, J. E., et al. 2014, *PASP*, 126, 250
 Mostek, N., Coil, A. L., Moustakas, J., Salim, S., & Weiner, B. J. 2012, *ApJ*, 746, 124
 Mouhcine, M., Lewis, I., Jones, B., et al. 2005, *MNRAS*, 362, 1143
 Muratov, A. L., Kereš, D., Faucher-Giguère, C.-A., et al. 2015, *MNRAS*, 454, 2691
 Murray, N., Quataert, E., & Thompson, T. A. 2010, *ApJ*, 709, 191
 Nelson, E. J., van Dokkum, P. G., Brammer, G., et al. 2012, *ApJL*, 747, L28
 Nelson, E. J., van Dokkum, P. G., Momcheva, I., et al. 2013, *ApJL*, 763, L16
 Newman, J. A., Cooper, M. C., Davis, M., et al. 2013a, *ApJS*, 208, 5
 Newman, S. F., Buschkamp, P., Genzel, R., et al. 2014, *ApJ*, 781, 21
 Newman, S. F., Genzel, R., Förster-Schreiber, N. M., et al. 2012, *ApJ*, 761, 43
 Newman, S. F., Genzel, R., Förster-Schreiber, N. M., et al. 2013b, *ApJ*, 767, 104
 Oke, J. B., Cohen, J. G., Carr, M., et al. 1995, *PASP*, 107, 375
 Oklopčić, A., Hopkins, P. F., Feldmann, R., et al. 2016, *MNRAS*, submitted (arXiv:1603.03778)
 Osterbrock, D. E. 1989, *Astrophysics of Gaseous Nebulae and Active Galactic Nuclei* (Mill Valley, CA: Univ. Science Books)
 Pannella, M., Elbaz, D., Daddi, E., et al. 2015, *ApJ*, 807, 141
 Planck Collaboration, Ade, P. A. R., Aghanim, N., et al. 2014, *A&A*, 571, 16
 Queyrel, J., Contini, T., Kissler-Patig, M., et al. 2012, *A&A*, 539, A93
 Reddy, N. A., Erb, D. K., Steidel, C. C., et al. 2005, *ApJ*, 633, 748
 Retzlaff, J., Rosati, P., Dickinson, M., et al. 2010, *A&A*, 511, A50
 Reyes, R., Mandelbaum, R., Gunn, J. E., et al. 2012, *MNRAS*, 425, 2610
 Rockosi, C., Stover, R., Kibrick, R., et al. 2010, *Proc. SPIE*, 7735, 77350
 Salim, S., Dickinson, M., Michael Rich, R., et al. 2009, *ApJ*, 700, 161
 Salim, S., Rich, R. M., Charlot, S., et al. 2007, *ApJS*, 173, 267
 Skelton, R. E., Whitaker, K. E., Momcheva, I. G., et al. 2014, *ApJS*, 214, 24
 Stott, J. P., Swinbank, A. M., Johnson, H. L., et al. 2016, *MNRAS*, 457, 1888
 Thompson, T. A., Quataert, E., & Murray, N. 2005, *ApJ*, 630, 167
 Vanzella, E., Cristiani, S., Dickinson, M., et al. 2008, *A&A*, 478, 83
 Weiner, B. J., Willmer, C. N. A., Faber, S. M., et al. 2006a, *ApJ*, 653, 1027
 Weiner, B. J., Willmer, C. N. A., Faber, S. M., et al. 2006b, *ApJ*, 653, 1049
 Whitaker, K. E., van Dokkum, P. G., Brammer, G., & Franx, M. 2012, *ApJL*, 754, L29
 Wirth, G. D., Willmer, C. N. A., Amico, P., et al. 2004, *AJ*, 127, 3121
 Wisnioski, E., Förster-Schreiber, N. M., Wuyts, S., et al. 2015, *ApJ*, 799, 209
 Wisnioski, E., Glazebrook, K., Blake, C., et al. 2011, *MNRAS*, 417, 2601
 Wisnioski, E., Glazebrook, K., Blake, C., et al. 2012, *MNRAS*, 422, 3339
 Wright, S. A., Larkin, J. E., Law, D. R., et al. 2009, *ApJ*, 699, 421
 Wurster, J., & Thacker, R. J. 2013, *MNRAS*, 431, 2513
 Wuyts, S., Förster-Schreiber, N. M., Genzel, R., et al. 2012, *ApJ*, 753, 114